ISSN 2398-6611 (Online)

Faculty of Engineering and Technology

Faculty Research Week 2019 Proceedings

14th-16th May 2019

Faculty of Engineering and Technology

James Parsons Building, Byrom Street, Liverpool,

L3 3AF

1

ISSN 2398-6611 (Online)

Contents

ISSN 2398-6611 (Online)

Petri Nets: a novel predictive approach to in silico analysis of developmental effects of thyroid hormone metabolism in humans.

T J Allen[1*], R Currie[2], L Dyson[3] and S D Webb[1]
[1]Dept. of Applied Mathematics, Liverpool John Moores University. [2]Syngenta UK Ltd. [3]Mathematics Institute, University of Warwick
* t.j.allen@2016.ljmu.ac.uk, http://bit.ly/webblabuk

Abstract. Thyroid hormone (TH) metabolism regulates nervous system development, and altered TH levels during critical periods of development result in adverse outcomes in the human foetus. Exogenous compounds exert thyroid effects through a variety of mechanisms such as disruption of hormone balance and result in TH metabolism dysfunction which can contribute to childhood neurological impairments. My research focuses on *in silico* modelling of TH balance in the mother and foetus using physiologically-based pharmacokinetics (PBPK) to develop a multi-compartment model that covers key developmental stages of the human foetus when critical neurodevelopmental effects of the TH metabolic network are occurring. The current model is formulated using Ordinary Differential Equations (ODEs) and an extension of graph theory called Petri Nets (PN) to create a novel approach to investigating metabolic networks, thus avoiding the financial and ethical considerations associated with *in vitro*/*in vivo* techniques. My model utilises a hybrid of deterministic and stochastic methods to quantitatively model the concurrent processes involved. This approach has already shown promise in providing key input to the OECD's efforts in making better use of increased knowledge of how chemicals induce adverse effects through Adverse Outcome Pathways (AOPs).

Keywords: Metabolism, Pharmacokinetics, Modelling, Ordinary Differential Equations, Petri Nets, Bioinformatics, Graph Theory, Gillespie Algorithm, Stochastic, Michaelis-Menten

1. Introduction

Thyroid hormones (TH) are essential for the control of metabolism and nervous system development, and altered TH levels during critical periods of development result in adverse outcomes in the human foetus[1], [2]. Exogenous compounds exert thyroid effects through a variety of mechanisms such as disruption of hormone balance and result in TH metabolism dysfunction. This dysfunction can contribute to childhood neurological impairments such as mental retardation, hearing loss and brain development in humans[3], and understanding whether exogenous chemicals are able to exacerbate these effects has implications both for clinical practice and public health. All environmental pollutants, pharmaceuticals, crop protection and industrial chemicals go through a battery of tests, many of which involve animals, to assess their potential for inducing adverse effects in humans and the environment[4]. A frequent finding is that many of these chemicals cause the induction of Phase II xenobiotic metabolism, whereby these compounds are conjugated with other molecules to allow their clearance from the body. This picture becomes more complicated, however, given that Phase II metabolism is involved in the clearance of the endogenous thyroid hormones triiodothyronine (T3) and its prohormone, thyroxine (T4)[5].

2. Novelty

A fully parametrised mother-foetal *in silico* model has not been established in the literature. One area in which there has been some mathematical progress is in pharmacokinetic (PK) modelling. PK modelling explores the transport of drugs through different areas of the body focussing on absorption, distribution, metabolism and excretion of the compound being examined. PK models would allow us to explore the kinetics of T3/T4 interaction throughout the body and observe how these hormones are distributed and absorbed in the different areas of interest. Two recent PK models of T3 and T4

metabolism are from Eisenberg *et al*[6] and McLanahan *et al*[7]. Eisenberg *et al* have created a multi-compartment model that aims to link the brain and thyroid together. They model the HPT axis as a series of fast and slow compartments and use simple transport mechanisms between the HPT axis and the brain submodel to monitor T3 and T4 levels over time. Though lacking a liver compartment, which is required for our desired outcomes, this model is a good starting point for our work.

3. Biology

My research focuses on *in silico* modelling of TH balance (or *homeostasis*) in the mother and foetus using physiologically-based pharmacokinetics (PBPK) to develop a multi-compartment model representing organs that covers key developmental stages of the human foetus when critical neurodevelopmental effects of the TH metabolic network are occurring. Thyroid hormone homeostasis is maintained through a negative feedback system involving the hypothalamus, pituitary and thyroid glands (HPT axis). After being secreted by the thyroid gland in a 10:1 ratio respectively, the free concentration of T4 and T3 tend to be low because they are mostly bound to thyroxine-binding globulin, transthyretin or albumin.

4. Methodology

We are developing a multi-compartment model of TH homeostasis in the mother and foetus covering key developmental stages when critical neurodevelopmental effects of the TH metabolic network occur using two modelling approaches: Ordinary Differential Equations (ODEs) and Petri Nets (PN).

4.1. Ordinary Differential Equations (ODEs)

The current model is formulated using ODEs to describe the mass action and chemical kinetics of the reactants involved, with Michaelis-Menten terms for enzymatic reactions. The Michaelis-Menten equation describes the rate of enzymatic reactions relating reaction rate, v, to the concentration of the substrate $[S]$, is given by:

$$v = \frac{d[P]}{dt} = \frac{V_{max}[S]}{K_m + [S]}$$

where $[P]$ is the concentration of product, P, V_{max} is the maximum reaction rate of P achieved at saturating P concentration. K_m is the Michaelis constant and represents the maximum rate at which the reaction rate is half of V_{max} as shown below in Figure 1.

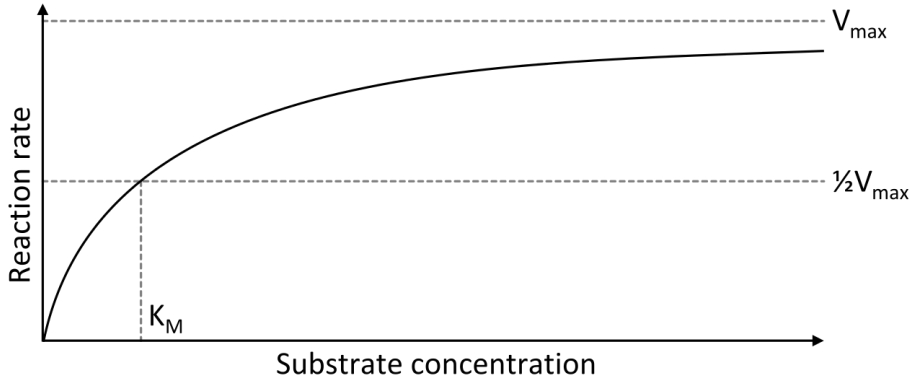

Figure 1. *Michaelis-Menten curve for an enzymatic reaction showing the relationship between reaction rate and concentration of reactant.*

4.2. Petri Nets (PNs)

My research also makes use of Petri Nets (PN) to create a novel approach to investigating metabolic networks, thus avoiding the financial and ethical considerations associated with *in vitro* and *in vivo* techniques. PNs are a bioinformatic technique composed of directed, bipartite graphs which have well defined mathematical foundations and allow the characterisation and analysis of concurrent systems such as cell signalling and metabolic networks[8]. Graph theory states that a *graph* is an object consisting of two sets called its *vertex set* and its *edge set*. The vertex set is a finite nonempty set. The

edge set may be empty, but otherwise its elements are two-element subsets of the vertex set. The theory further defines a *bipartite graph* as a graph whose vertices can be divided into two disjoint and independent sets *P* (places) and *T* (transitions), P ∩ T, such that every edge connects a vertex in *P* to one in *T*. A *directed* bipartite graph then, such as considered in the concept of a Petri Net, has directed edges that point *from* the vertex in a pair and points *to* the second vertex in that pair, i.e. from *P* to *T*. In the extension of Graph theory to Petri Nets, vertices are renamed *places* and edges as *arcs*. Places can hold a finite number of marks called *tokens* to show the number of times a place appears in a given configuration of the PN. The marking, m can be considered as the configuration of tokens distributed over an entire PN. Places are linked via arcs to transitions *T*, which are then linked to another place, the former being termed *input places* and the latter *output places*. No arc may connect two places or two transitions. Arcs can possess arc weights, *w*, which serve to modify the stoichiometry of the PN to direct tokens over it. A transition is said to *fire* if it is enabled, i.e. there are sufficient tokens in all of its input places and, when the transition fires, it consumes the required input tokens, and creates tokens in its output places. This therefore changes the configuration of the PN. A transition is enabled when the number of tokens in its input places are at least equal to the arc weight going from the place to the transition and can fire at any time in a stoichiometric manner. When fired, the tokens in the input places are moved to output places via transitions according to arc weights resulting in a new marking of the net; thus simulating the stochastic nature of the metabolic system[9]. There are several different arc types that can be used in PNs in addition to the standard arc described above. Among them is the *read arc* which is useful in modelling enabling reactions such as enzymatic catalysis whereby the arc checks for the presence of tokens without consuming them.

In this model, the stoichiometry is governed by a Gillespie Algorithm[10]. The algorithm requires the reactant molecules to be dilute and well-mixed throughout the containing volume. In contrast to the traditional differential equations of chemical kinetics, which imposes not only those requirements but also the requirement that the molecular populations be very large, the Gillespie Algorithm simulates the occurrence of individual reaction events in a way that properly reflects their inherent randomness. That randomness is often important for the relatively low molecular populations that commonly occur in cellular systems[10]. A discussion of the mathematical formalism behind PNs and their future outlook are discussed by Koch[11]. An excellent review of PNs compared with ODEs as a mathematical modelling approach to biological systems is given by Ji *et al*[12]. The utility of PNs is that parameterisation is not a requirement; the PN is parameter agnostic, in that it works simply on how the network is wired. Thus PNs allow quick initial modelling and can be used to gap-fill missing parameters in the PBPK model. Where parameter values can be obtained, however, these can be included in the PN to produce a Hybrid Stochastic PN (HSPN), which has the advantage of being able to utilise some available values to model the system and can even use fuzzy logic[13].

5. Evidence and validation

The model has been validated against in vivo data[14] and utilises a hybrid of deterministic and stochastic methods to quantitatively model the concurrent processes involved. This approach has already shown promise in providing key input to the Organisation for Economic Co-operation and Development's (OECD) efforts in making better use of increased knowledge of how chemicals induce adverse effects through Adverse Outcome Pathways[15].

6. References

[1] G. R. Williams, "Neurodevelopmental and neurophysiological actions of thyroid hormone," *J. Neuroendocrinol.*, vol. 20, no. 6, pp. 784–794, Dec. 2008.

[2] L. Préau, J. B. Fini, G. Morvan-Dubois, and B. Demeneix, "Thyroid hormone signaling during early neurogenesis and its significance as a vulnerable window for endocrine disruption," *Biochim. Biophys. Acta - Gene Regul. Mech.*, vol. 1849, no. 2, pp. 112–121, Feb. 2015.

[3] M.-L. L. Hartoft-Nielsen *et al.*, "Do Thyroid Disrupting Chemicals Influence Foetal

Development during Pregnancy?," *J. Thyroid Res.*, vol. 2011, pp. 1–14, Dec. 2011.

[4] F. Maqbool, S. Mostafalou, H. Bahadar, and M. Abdollahi, "Review of endocrine disorders associated with environmental toxicants and possible involved mechanisms," *Life Sci.*, vol. 145, pp. 265–273, Dec. 2016.

[5] T. J. Visser, "Role of sulfation in thyroid hormone metabolism.," *Chem. Biol. Interact.*, vol. 92, no. 1–3, pp. 293–303, Jun. 1994.

[6] M. Eisenberg, M. Samuels, and J. J. DiStefano, "L-T $_4$ Bioequivalence and Hormone Replacement Studies via Feedback Control Simulations," *Thyroid*, vol. 16, no. 12, pp. 1279– 1292, Dec. 2006.

[7] E. D. McLanahan, M. E. Andersen, and J. W. Fisher, "A Biologically Based Dose-Response Model for Dietary Iodide and the Hypothalamic-Pituitary-Thyroid Axis in the Adult Rat: Evaluation of Iodide Deficiency," *Toxicol. Sci.*, vol. 102, no. 2, pp. 241–253, Apr. 2008.

[8] I. Koch, "Petri nets in systems biology," *Softw. Syst. Model.*, vol. 14, no. 2, pp. 703–710, Dec. 2015.

[9] T. Murata, "Petri Nets: Properties, Analysis and Applications," *Proc. IEEE*, vol. 77, no. 4, pp. 541–580, Apr. 1982.

[10] D. T. Gillespie, "A general method for numerically simulating the stochastic time evolution of coupled chemical reactions," *J. Comput. Phys.*, vol. 22, no. 4, pp. 403–434, Dec. 1976.

[11] I. Koch, "Petri nets - A mathematical formalism to analyze chemical reaction networks," *Mol. Inform.*, vol. 29, no. 12, pp. 838–843, Dec. 2010.

[12] Z. Ji, K. Yan, W. Li, H. Hu, and X. Zhu, "Mathematical and Computational Modeling in Complex Biological Systems," *Biomed Res. Int.*, vol. 2017, pp. 1–16, Dec. 2017.

[13] F. Liu, M. Heiner, and M. Yang, "Fuzzy Stochastic Petri Nets for Modeling Biological Systems with Uncertain Kinetic Parameters.," *PLoS One*, vol. 11, no. 2, p. e0149674, Feb. 2016.

[14] L. A. Burmeister, J. Pachucki, D. L. St. Germain, and D. L. St Germain, "Thyroid hormones inhibit type 2 iodothyronine deiodinase in the rat cerebral cortex by both pre- and posttranslational mechanisms.," *Endocrinology*, vol. 138, no. 12, pp. 5231–7, Dec. 1997.

[15] M. Vinken, "The adverse outcome pathway concept: A pragmatic tool in toxicology," *Toxicology*, vol. 312, no. 1, pp. 158–165, Dec. 2013.

ISSN 2398-6611 (Online)

Implications for dark matter direct detection searches using new Milky Way cosmological simulations

R Poole-Mckenzie
2.24, Astrophysics Research Institute, 146 Brownlow Hill, Liverpool, L3 5RF
r.poolemckenzie@2013.ljmu.ac.uk

Abstract: The direct detection of dark matter (DM) relies significantly on its local velocity distribution and density. An accurate model of local DM properties is essential to place reliable constraints on DM particle cross-sections. Current methods adopt the Standard Halo Model (SHM) which assumes a simple Maxwellian distribution of local DM velocities and a fixed value for the local DM density. We investigate the local DM velocity distribution and density using Milky Way mass-like galaxies generated from new, high-resolution cosmological zoom simulations called "EAGLE zooms". The halos used in this work provide a more representative sample of Milky Way mass-like disk galaxies than previous studies. Our results show the velocity distribution in the local neighbourhood varies significantly from halo-to-halo and the mean of the distributions is well described using a simple Maxwellian distribution in the hydrodynamic case. We obtain a local DM density of 0.23-0.47 $GeVcm^{-3}$. For the DM-only case we find that the local velocity distribution is less well described using a Maxwellian and the peak velocity is smaller. We concluded that the SHM is justified to use a Maxwellian distribution, however the variation on local DM v_0 and ρ_0 seen from halo-to-halo increase the uncertainty when determining the WIMP cross-sections.

Keywords: dark matter, direct detection

1. Introduction

1.1 The WIMP paradigm

Dark matter (DM) is the most influential component of matter in the Universe and plays a vital role in the formation of large-scale and galactic structures. The evidence for DM is strong, with flat rotation curves from spiral galaxies [1, 2], cosmic microwave background anisotropies [3], velocity dispersions in galaxy clusters [4] and masses obtained from gravitational lensing [5] all suggesting the existence of a new, non-baryonic particle. However, identifying the exact nature of DM remains a mystery. Very little is known about DM as a particle, although it must be consistent with several observational constraints [6]. Particle physics has suggested numerous particle candidates beyond that of the Standard Model (SM), with the most compelling evidence favouring that of a new electromagnetically neutral, non-baryonic particle - the Weakly Interacting Massive Particle (WIMP) [7]. The existence of the WIMP or any other particle beyond the SM will not be verified until a signal is clearly identified via indirect or direct detection experiments or in particle accelerators.

1.2 Direct detection

The observationally confirmed presence of a DM halo in our Galaxy provides an interesting source of investigation for DM particle searches. This work will focus on direct detection experiments with numerous experiments having played an important role in this attempt to directly detect DM in the form of WIMPs via their elastic scattering off of nuclei [8]. The interaction rate from the DM interactions relies significantly on the local velocity distribution and the local DM density. An accurate model of the local DM velocity distribution is essential to place improved constraints on the DM particle properties. Current direct detection experiments adopt an isothermal and isotropic theory known as the Standard Halo Model

(SHM). The SHM assumes that the velocity distribution is Maxwellian, with a peak speed of 220 kms^{-1} and uses a constant value of $\rho\rho_{\chi\chi}$ = 0.3 $GeVcm^{-3}$. However, the this may not be the case.

2. Methodology

We investigate the local DM velocity distribution of 18 Milky Way mass-like halos generated from new, high-resolution, hydrodynamical cosmological simulations called “EAGLE zooms”. The new simulations have the advantage of increased resolution, which is a result of using the "zoom-in" technique, where a halo is identified in a lower resolution simulation, and then re-simulated. These simulations have been implemented with (hydrodynamic) and without baryonic physics (DM-only – DMO).

Throughout this study we adopt a coordinate system that is in the rest frame of the galaxy. This is achieved by aligning the halo with the principle axis of the angular momentum calculated within the stellar disks inner 20kpc. Our new reference system has the origin at the galactic centre, x and y are in the plane of the stellar disk and z is perpendicular to the stellar disk. For the halos in the DMO simulations, we use the alignment coefficients from the matched hydrodynamic halos to orientate the coordinates.

We define the Solar neighbourhood (local) region as a cylindrical shell with a radial distance 4% of $R_{200} \pm 1$ kpc and 1.5 kpc either side of the galactic plane. We select 4% as this is the distance of the Sun from the Galactic centre with respect to the Milky Way’s virial radius, $R_{200} \approx 210$ kpc [9]. The newly defined local region contains a total of 10,611- 21,144 DM particles for the hydrodynamic simulations and 6,889 - 17,980 for the DMO simulation.

3. Results

3.1 Local dark matter densities

The volume averaged local DM densities are in the range of 0.23 - 0.47 $GeVcm^{-3}$ for the halos in our hydrodynamic simulations and 0.15 - 0.38 $GeVcm^{-3}$ for the DMO simulations. The difference in densities between the hydrodynamic and DMO simulations is as expected, with the dissipative baryons deepening the potential well at the centre of the halos, increasing the number of particles in the inner regions and hence increasing the regions density.

3.2 Local dark matter velocities

We analyse the velocity distributions generated from our hydrodynamic and DMO simulations for all of our selected halos and compare them with the Maxwellian hypothesis. Using the aligned halos from both the hydrodynamic and DMO simulations we are able to calculate the local velocity modulus distribution and determine the distribution of local velocities (figure 1).

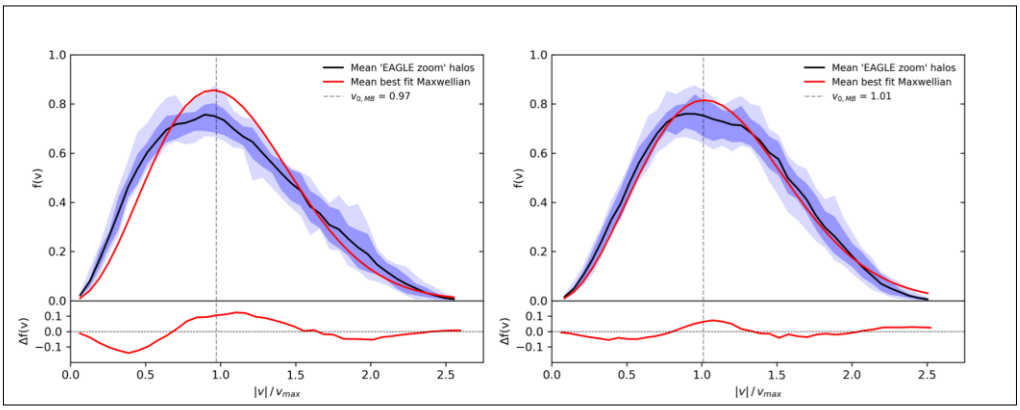

Figure 1 - Dark matter velocity modulus distributions in the rest frame of the galaxy, normalised by the maximum rotational velocity, V_{max}. The solid black line represents the mean of velocity modulus distributions for the DMO (left) and hydrodynamic (right) simulations. The solid red line represents the mean of the best fitting Maxwellian distributions. The dark and light blue

contours enclose 68% and 95% of the velocity distribution from all halos. The lower panels show the residuals between the mean distribution of the halos and the mean Maxwellian fit.

Figure 1 shows the mean local DM velocity modulus distribution in the rest frame of the galaxy for all halos in the hydrodynamic and DMO simulations. All halos in both sets of simulations have been fitted with a Maxwellian distribution,

$$f(v_i) = \frac{N}{2\pi v_0^2} e^{\frac{\vec{v}^2}{2v_0^2}} \qquad (2)$$

where N is the normalisation constant and v_0 is the peak of the Maxwellian, which is treated as a free parameter. We find that the hydrodynamic case is reasonably well described by a Maxwellian distribution, with a slight deviation at very high velocities. In contrast, the DMO case is poorly described by a Maxwellian, with large deviations seen at both low velocities and in the peak of the distribution. We also observe significant halo-to-halo variation in the distributions for both cases. The mean local velocity distribution has a peak velocity of v_0 = 179 kms^{-1} and v_0 = 160 kms^{-1}, for the hydrodynamic and DMO simulations respectively. The higher peak velocity in the hydrodynamic simulations can be attributed to the effect of the baryons deepening the potential well of the halo, causing the particles to travel at higher velocities.

3.3 Implications for direct detection

As mentioned previously, the limits placed on the WIMP-nucleon cross-section are dependent on several local DM properties. In addition to these, the limits rely on experimental parameters such as the detectors material and mass, as well as the number of days the experiment runs for (i.e. live-days). Currently the most sensitive result and most constraining value on the WIMP-nucleon cross-section has be determined by the XENON1T direct detection experiment [10].

Figure 2 shows our predicted WIMP interaction cross-section constraints, assuming a Maxwellian distribution of velocities. We apply the local DM densities, local peak velocities and escape velocities of the halos from our simulations into our interaction cross-section calculations, as well as the experimental parameters used by XENON1T. Additionally, we provide results for the DMO case, which demonstrates the effect of baryons on the results from direct detection experiments.

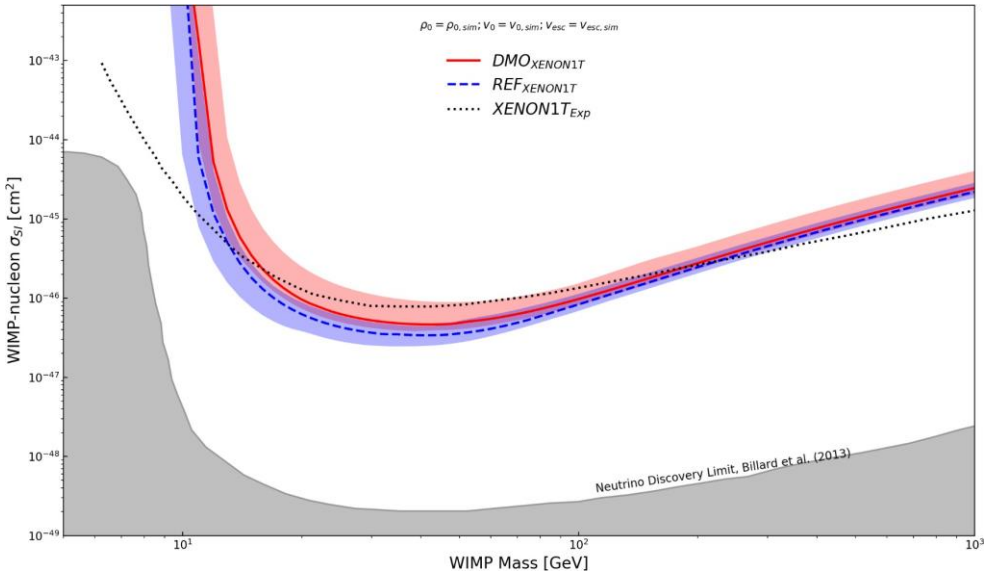

Figure 2 – The exclusion limits for the 'EAGLE zoom' halos and XENON1T parameters. The mean upper-limits are shown as red and blue lines for the DMO and hydrodynamic case, respectively. The contours enclose 68% of all the individual exclusion limits for the 18 halos. The black dotted line shows the experimental predictions from XENON1T assuming the Standard Halo Model.

We find that the hydrodynamic case places a lower upper limit on the WIMP interaction cross-section than the DMO case. This is caused by the lower local DM densities in the DMO simulation, a lower density requires a larger cross-section to produce the same interaction rate. The variation seen the local velocity distributions propagates through to the cross-section results, increasing the uncertainty on upper-limits. The differences seen between our results and the experimental data at low WIMP masses can be attributed to the lower escape velocities of our simulations than that of the Milky Ways. We place an upper limit of 3.4×10^{-47} cm^2 and 4.8×10^{-47} cm^2 on the WIMP-nucleon cross-section for the hydrodynamic and DMO case, respectively. The variation seen in the hydrodynamic case places a lower upper-limit on the WIMP-nucleon cross-section, constraining the WIMPs physical properties further than experimental predictions.

4. Summary

We have used a new suit of zoomed cosmological simulations from a modified EAGLE code to produce Milky Way-like halos in order to study the local DM density and velocity distributions, to understand the implications for direct detection. The main points from this work are summarised below:

- The local DM velocity distribution of the hydrodynamic simulations are well defined by a Maxwellian, however the DMO simulations are poorly described using a Maxwellian.
- The impact of the baryons in the hydrodynamic simulations drives a shift of the peak velocity to higher velocities when compared to the DMO case.
- The significant halo-to-halo variation in the velocity distributions caused by the range of densities and peak velocities in the simulations adds additional uncertainty to the exclusion limits for direct detection experiments.
- The variation in the hydrodynamic WIMP-nucleon cross-section shows that the experimental predictions may be lower than expected when ranges of densities and velocities are considered.

5. References

[1] V. C. Rubin, N. Thonnard and W. K. Ford, Jr., Extended rotation curves of high-luminosity spiral galaxies. I - The angle between the rotation axis of the nucleus and the outer disk of NGC 3672, 217 (1977) L1.
[2] P. Salucci, A. Lapi, C. Tonini, G. Gentile, I. Yegorova and U. Klein, The universal rotation curve of spiral galaxies - II. The dark matter distribution out to the virial radius, 378 (2007) 41.
[3] M. White, D. Scott and J. Silk, Anisotropies in the Cosmic Microwave Background, 32 (1994) 319.
[4] F. Zwicky, On the Masses of Nebulae and of Clusters of Nebulae, 86 (1937) 217.
[5] E. Aubourg, P. Bareyre, S. Bréhin, M. Gros, M. Lachièze-Rey, B. Laurent et al., Evidence for gravitational microlensing by dark objects in the Galactic halo, 365 (1993) 623.
[6] Arcadi, G., et al. (2018). The waning of the WIMP? A review of models, searches, and constraints. *The European Physical Journal C*, *78*(3), 203.
[7] Steigman, G., & Turner, M. S. (1985). Cosmological constraints on the properties of weakly interacting massive particles. *Nuclear Physics B*, *253*, 375-386.
[8] Goodman, M. W., & Witten, E. (1985). Detectability of certain dark-matter candidates. *Physical Review D*, *31*(12), 3059.
[9] J. I. Read, The local dark matter density, J. Phys. G: Nucl. Part. Phys. 41 (2014) 063101.
[10] E. Aprile, J. Aalbers, F. Agostini, M. Alfonsi, F. D. Amaro, M. Anthony et al., First Dark Matter Search Results from the XENON1T Experiment, Phys. Rev. Lett. 119 (2017) 181301.

ISSN 2398-6611 (Online)

A novel non-destructive electromagnetic method to assess the integrity of marine structures

G S Omer, M. Riley, P. Kot, W. Atherton, A. Shaw, S. Wylie, M. Muradov,

Built Environment and Sustainable Technologies Research Institute (BEST), Liverpool John Moores University, Byrom Street, Liverpool, L3 3AF, UK

G.S.Omer@2015.ljmu.ac.uk; M.L.Riley@ljmu.ac.uk; P.Kot@ljmu.ac.uk; W.Atherton@ljmu.ac.uk; A.Shaw@ljmu.ac.uk; S.R.Wylie@ljmu.ac.uk; M.Muradov@ljmu.ac.uk

Abstract:

Corrosion of the reinforcing steel is the main reason for deterioration and damage in reinforced concrete structures such as concrete columns and bridge decks. One such aggressive substance, present predominantly in marine or coastal environments, is chloride and the associated chloride ions. Chloride in the presence of oxygen and water cause pitting corrosion and the measurement of chloride content is a significant issue in the discovery of early corrosion damage induced by chloride attack. Marine concrete can be grouped into three exposure zones: submerged, splash and atmospheric zones. However, the current state of art solutions do not provide a non-destructive technology that would be able to provide an instant chloride level in concrete structures. This research investigates a novel method for the detection of chloride level using electromagnetic (EM) waves. The proposed study assesses experimentally the propagation of EM waves through concrete blocks without reinforcement and their interaction with water and salt water. The developed microwave sensor operates in the 2 GHz-13 GHz frequency range using a Rohde&Schwarz ZVL13 Vector Network Analyser (VNA). Finally, the graphical user interface was developed using LabVIEW software to capture the data from the sensor. Results demonstrate that the developed sensor is capable of determining the amount of salt water and tap water was absorbed by the concrete sample during curing process over a 28-day period.

Keywords: Chloride attack; Concrete Structure; Electromagnetic Waves; Horn Antenna; Non-destructive testing.

Introduction & background.

In the last few decades, reinforced concrete has been one of the most used building materials. It has proved to be a reliable structural material with very good durability performance when properly utilised. However, there are many structures, which show early deterioration, namely those exposed to aggressive substance environments. Experience shows that the corrosion of the reinforcement is the main causes of structural concrete deterioration. Therefore, this type of damage is responsible for the huge financial costs each year associated with the repair of deteriorated structures. Nowadays, it is well known that the durability of material and structures depends both on the environmental conditions at the exposed surfaces of the structures and on the resistance of the material to the action of aggressive substances. Thus, the determination of chloride content in a concrete structure is an important part of periodic non-destructive testing carried out for structures identified to be vulnerable to chloride-induced reinforcement corrosion [1].

In many concrete structures, chloride content caused reinforcement corrosion in the neighbourhood of the reinforcing bars from sources not initially present from the construction stage. A common cause of reinforcement corrosion is the gradual permeation and diffusion of chloride ions from the surface of the concrete [2]. Marine concrete can be grouped into three exposure zones: submerged, splashed and atmospheric zones. The submerged zone is continuously covered by seawater, the splash zone is subject to continuous wetting and drying and the atmospheric zone is above the splash zone and subject to occasional seawater spray. Therefore, deterioration in any of these zones tends to increase the concrete permeability, making the concrete liable to more deterioration. Cracks, spalls, mortar erosion, and corrosion stains are visible signs of deterioration that

causes increases porosity and decreased strength [3]. Chloride attack is a particular problem in highway concrete, where de-icing salts are used to melt away snow. The process of deterioration of the corrosion continues based on the availability of moisture, oxygen and carbon dioxide along with the presence of chloride ions in the concrete [4, 5].

Microwaves have been well defined as being sensitive to moisture content. For non-destructive testing, many applications for moisture determination use the microwave method. In the microwave technique, valuable information about the permittivity of the sample [6] is known. As water has a high dielectric constant at microwave frequencies compared to dry materials, it is easily measured using the technique. Other apparatus able to measure moisture content can be destructive for building fabrics such as bricks, concrete, blocks, plaster, etc., as they require additional drilling into the wall to take samples of the content. Furthermore, these types of methods provide inexact results. The Compton method provides enhanced results scattering of gamma ray's [7]. Moreover, it is even more essential for inspection methods to spread electromagnetic (EM) waves through the structure and determine building fabric failures, such as concrete flat roof membrane failures and the deterioration of marine structures. Research has been undertaken in developing a novel method that would use EM waves to resolve the problems mentioned above. Different ranges of EM waves were used for testing as well as horn antennae, which were used to identify the best parameters to provide accurate measurements [8].

Methodology and Results:

The aim of this investigation is to develop a novel non-destructive electromagnetic wave (EM) sensor to determine the chloride level in concrete structures. The first step of this research was to review the literature on the current techniques and methods to determine the amount of chloride in the concrete structures. Based on the literature review, it was discovered that commercially available techniques to define the level of chloride are destructive, time-consuming and high cost. In addition, understanding, the impact of chloride content, moisture and temperature on the dielectric constant of the concrete structures is considered important. The horn antenna was used to detect the moisture, chloride content and location of the reinforcement in the concrete structures. The antenna has been designed to be able to carry out many measurements without being worried about its displacement. In addition, the sensor operates in frequency ranges between (2 to 18 GHz) and the measurements were provided by s-parameters namely S11 or S21. The designed sensor as shown in Figure 1. The curing process experiment was undertaken for two concrete samples without reinforcement. One of the samples was submerged into the tap water and the second one submerged into the salt water for 28 days curing. To simulate the seawater concentration 3.5%NaCl was used. Conductivity readings were taken with the use of a Hanna Instruments conductivity meter. The conductivity of tap water was 0.176 mS/cm and the conductivity of salt water was 50.7 mS/cm by comparison, seawater has a conductivity of approximately 50 mS/cm. Hence, both plain concrete samples were separately submerged in their respective solutions to within 6mm of their top surface and were used as reference test specimens, for monitoring the effects of the tap water and salt water solution during the curing period for 28 days. Both sensors were positioned on top of the concrete surface with a 20 mm gap between the surface of the sensor and surface of the concrete sample. Then the sensor was connected to a Vector Network Analyser (VNA), which in turn was connected to a desktop computer running a modified LabVIEW program for continuous capture of S_Parameter (S_{21}). The following Figures 2 and 3 show the full experimental setup during the sample test.

Figure 1: Sensor design

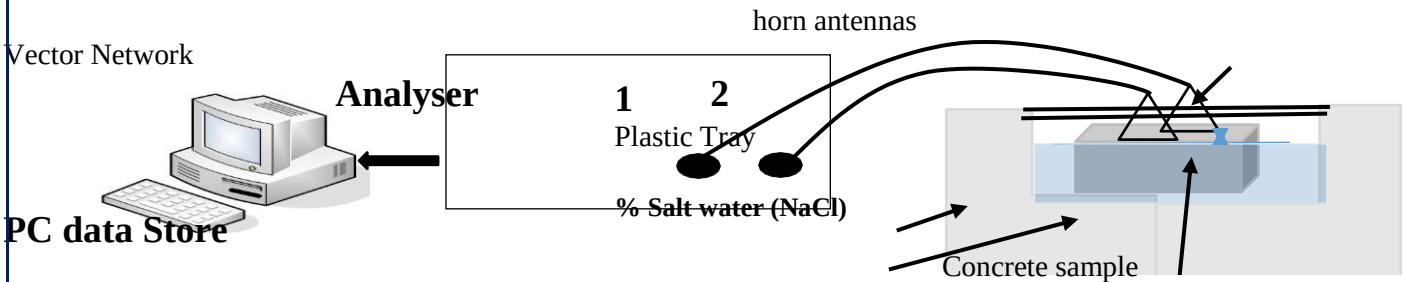

Figure 2: Block diagram setup for curing process.

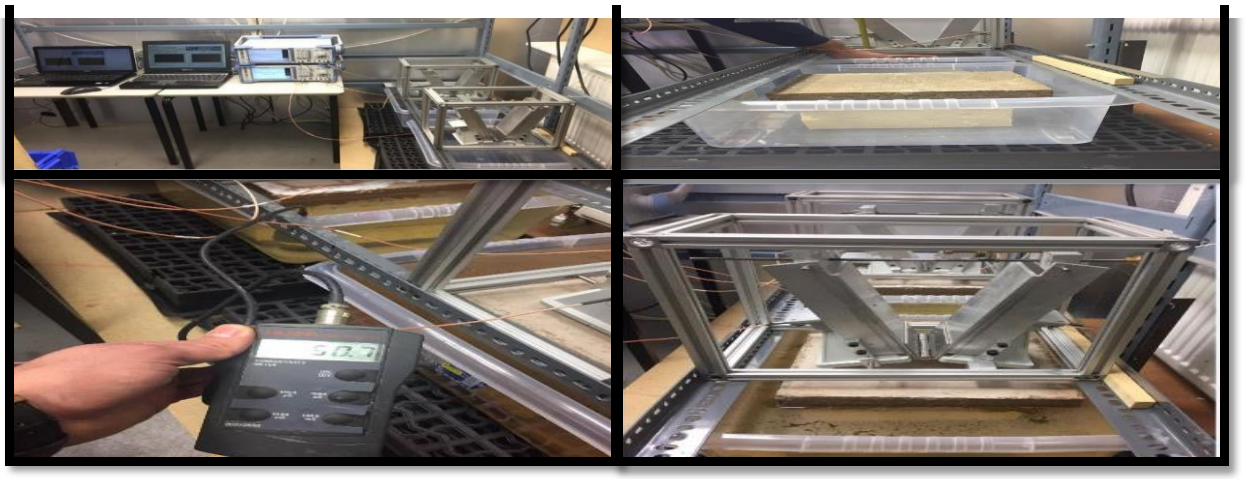

Figure 4: Preliminary experimental setup for curing process.

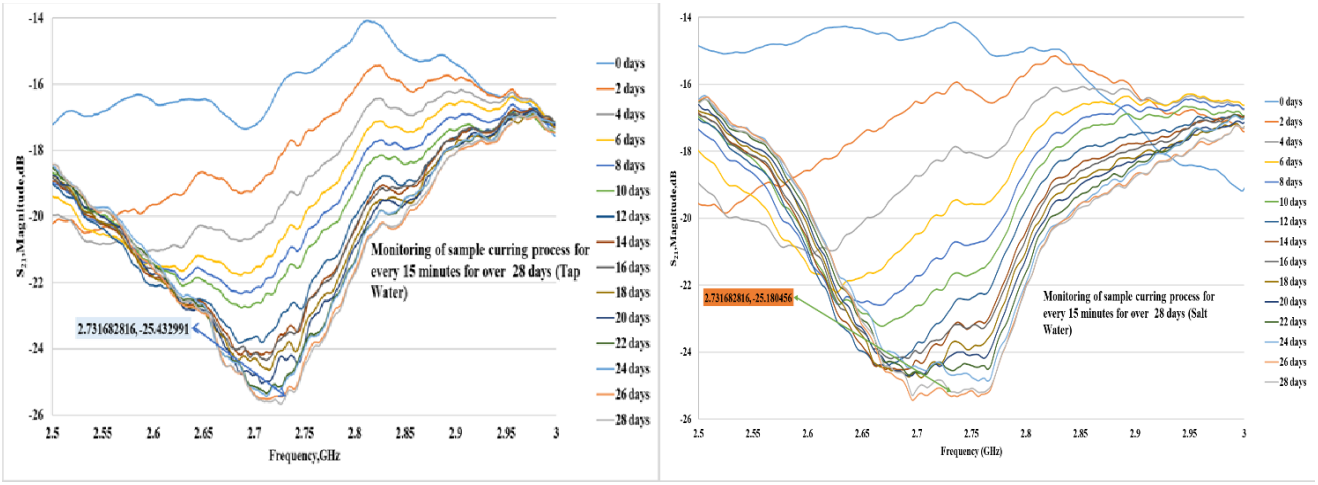

Figure 3: S_{21} measurements of curing process of the plain concrete for different concentrations over 28 days.

Figure 4 shows the S_{21} measurements for both concrete samples taken every 15 minutes during 28 days, while it was submerged in both tap water and salt water. It can be seen that there is a noticeable change in the electromagnetic waves (EM) signature between the frequency range 2.5GHz and 3 GHz, especially at the frequency 2.316GHz. The change is affected by the amount of water and salt water absorbed in the concrete samples during the 28 days curing process. This is because water has a high dielectric property that is why the microwave signal changed. Additionally, electromagnetic wave absorption is dependent on salt content and temperature. Both samples were not moved during the experimental work, and maintained at a room ambient temperature of 20 ± C°.

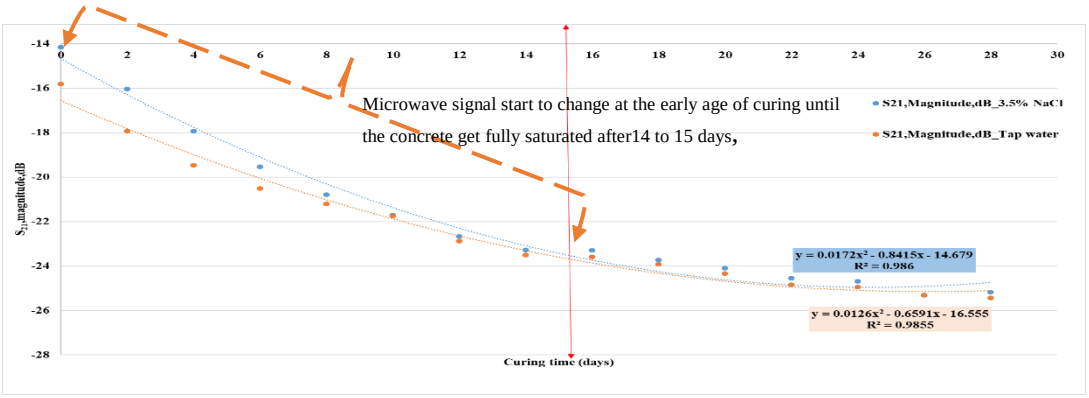

Figure 5: Comparison for both sample S_{21} measurements against curing time at frequency range of 2.732GHz.

Figure 5 shows that the microwave signal started to change at an early age of curing until the concrete was fully saturated. This is because concrete strength increased with age and sufficient moisture and favourable temperatures were also present for the cement hydration. Changes were attributed to two main features, namely: a) after each soaking cycle more salt is deposited into the concrete slabs through the pores. b) the addition of salt in the pores slows the evaporation rate of the liquid water from the concrete slabs. In the case where the chloride content in a specimen is above a certain limit, the chloride will interact with any free bound water and significantly affect its dielectric properties.

Conclusion and Future work: The experiment provides identifiable results that the electromagnetic waves at frequency ranges between 2 to 13.0GHz can be used to investigate chloride content in marine concrete structures using real time measurement's and in a non-destructive manner. Future work will provide more data analysis and enhance the sensor development.

References

[1] Spitzlei, M., *Choosing a Method for Measuring youir Materials Moisture content*, in *Article*. 2002. p. 1-9.

[2] Glasser, F.P., J. Marchand, and E. Samson, *Durability of concrete — Degradation phenomena involving detrimental chemical reactions.* Cement and Concrete Research, 2008. **38**(2): p. 226-246.

[3] Osio-Norgaard, J., J.P. Gevaudan, and W.V. Srubar, *A review of chloride transport in alkali-activated cement paste, mortar, and concrete.* Construction and Building Materials, 2018. **186**: p. 191-206.

[4] Zhou, Y., et al., *Carbonation-Induced and Chloride-Induced Corrosion in Reinforced Concrete Structures.* Journal of Materials in Civil Engineering, 2015. **27**(9): p. 04014245.

[5] Bioubakhsh, S., *The penetration of chloride in concrete subject to wetting and drying*, in *Faculty of the Built Environment*. 2011, Univerity College London: UCL (University College London). p. 355.

[6] Verma, S.K., S.S. Bhadauria, and S. Akhtar, *Review of Nondestructive Testing Methods for Condition Monitoring of Concrete Structures.* Journal of Construction Engineering, 2013. **2013**: p. 1-11.

[7] Bucuresu, D., *NON- destructive measurment of Moisture in Building Materials by Compton Scattering og Gamma Rays.* 2011. **63**(1): p. 61-75.

[8] Bavusi, M., et al., *Electromagnetic Sensing Techniques for Non-Destructive Diagnosis of Civil Engineering Structures.* 2012.

ISSN 2398-6611 (Online)

Turbulent Drag Reduction Using Backswimmer Textured Surfaces for Channel Flow

K Takrouri & M Seddighi
Department of Mechanical and Maritime Engineering, Liverpool John Moores University, L3 3AF
E-mail address: K.W.Takrouri@2016.ljmu.ac.uk
M.Seddighi@ljmu.ac.uk

Abstract. Using Direct Numerical Simulations (DNS), the present study examines turbulent drag reduction for a novel geometry inspired by the Backswimmer; an efficient aerodynamic insect, contains a very good air retaining surface and potentially a drag reduction geometry. Simulations are performed for a channel flow at low Reynolds number $Re_\tau = 180$. Turbulence statistics and detailed flow structures for the textured surface are compared against the smooth channel flow case. Preliminary results show a drag reduction (DR%) up to 20.1%.

Keywords. Backswimmer, Drag Reduction, Direct Numerical Simulations.

1. Introduction

Drag reduction has been an interesting field of research for the past years. The use of biomimetic inspired textured surfaces has been one of the extensively studied drag reduction techniques. Examples of textures include shark skin geometry [2], wavy riblets [7], square riblets [5] and liquid infused rough surfaces using longitudinal bars or staggered cubes [1]. However, most of the previous established research has been mainly focused on the square cross section elements or irregular random textured surfaces. The Backswimmer insect also known as the Notocenta glauca can dive and swim quickly through water [3]. Also, the Backswimmer is capable of supporting itself under water using its forelegs and the tip of its abdomen. From a biological point view the air layers found on the wings of the Backswimmer are considered a biological role model for biomimetic fluid drag reduction using its double structure of hairs and microvilly (the implemented geometry) which are mainly responsible for air retention and other sensory functions. The present study examines the turbulent structure and drag reduction in a channel flow consists of smooth top surface and a textured bottom surface inspired by the backswimmer.

2. Methodology

The in-house Direct Numerical Simulations (DNS) code CHAPSim is used to study the physics of the turbulent flow over both smooth and textured surfaces. The texture geometry is implemented using an Immersed Boundary Method (IBM); the code is adopted for treating different types of textured surfaces and has been validated against previous literature [8] for both smooth and textured channel flows. The Backswimmer geometry was implemented by digitizing a schematic of the Backswimmer micro-structure. The implemented geometry is shown in figure 1 (left). The number of points used to present the Backswimmer geometry is equal to 50, 32, 24 in the stream-wise, wall-normal and span-wise directions, respectively. The 3D implementation of the computational domain is shown in figure 1(right).

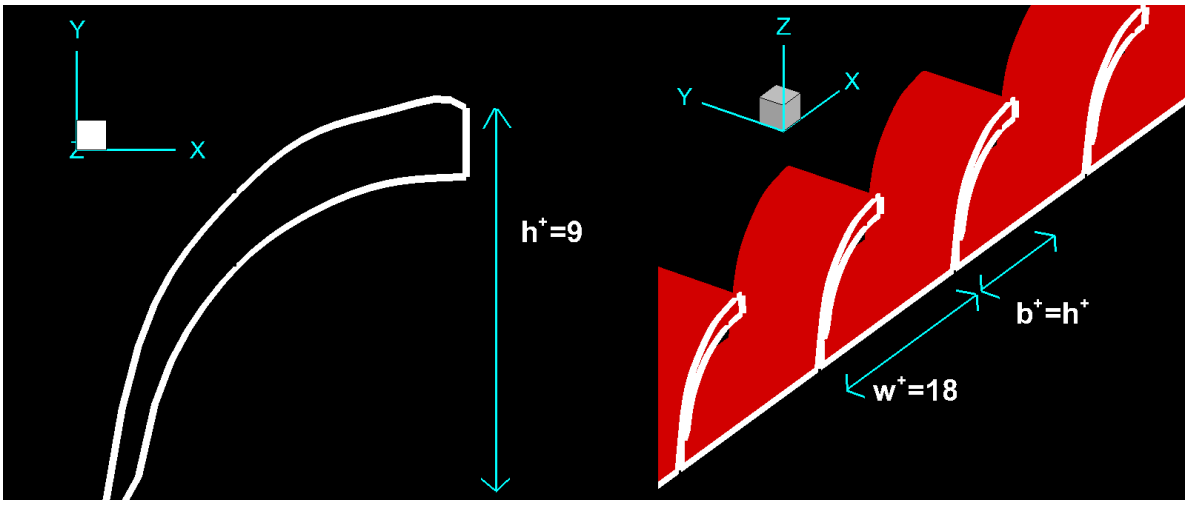

Figure 1 Backswimmer micro structure textured surface. The computational domain contains 18, 8 elements in the stream wise and span-wise directions, respectively. h+,b+ and w+ are the height, width and the spacing between each of the texture elements in the stream-wise direction in wall units at friction Reynolds number $RRee_{\tau\tau} = 180$.

3. Results and discussion

A net drag reduction in terms of the change in the skin friction drag coefficient (Cf) of DR = 20.1% was achieved using Equation 1. The computational domain size is $12\delta\delta \times 2\delta\delta \times 4\delta\delta$ where $\delta\delta$ is the channel half height. The mesh size equal to $1800 \times 320 \times 384$ with 18×8 roughnes elements in the stream-wise, wall-normal and span-wise directions respectively at a reference friction Reynolds number $RRee_{\tau\tau} = 180$.The preliminary analysis for the two textures topologies were made using instantaneous flow field data and some first and second order turbulence statistics.

$$DR\% = \frac{Cf_s - Cf_{BS}}{Cf_s} \times 100\% \qquad (1)$$

Where DR% is the drag reduction percentages, $CCff_{ss}$ is the smooth channel flow skin friction drag coefficient and $CCff_{BBss}$ is the Backswimmer channel skin friction drag coefficient.

Figure 2 shows the mean velocity profiles for both the smooth and the Backswimmer channel flow normalized by the wall units of the smooth channel ($uu_{\tau\tau}$ for the velocity and $\frac{vv}{uu_{\tau\tau}}$ for the wall-normal distance). Compared to the smooth-case, the velocity profile of the textured case shows a shift in the viscous sub-layer and also an elevated log-law region. This is due to the reduced friction velocity in the textured case and is consistent with the drag reduction obtained. This is also consistent with other drag reducing textured geometries studied in previous literature [4].

Figure 3 shows the root mean square velocity profiles for the smooth and the Backswimmer test cases. It is seen that the texture changes in the r.m.s of fluctuating velocities for the region up to $yy^+ \sim < 50$. The wall normal and the span-wise direction components of the generated profiles are consistent with previous drag reduction textured surfaces. However the maximum stream-wise r.m.s. velocity was higher for the Backswimmer unlike square riblets and super hydrophobic surfaces.

Figure 4 shows the Reynolds shear stress profile normalized by the friction Reynolds number. A dip in the Reynolds shear stress profile towards the negative direction is noticed for the Backswimmer case unlike the smooth case near wall profile as it starts at zero and increases positively along the wall normal direction. Also the shear stress values for the backswimmer case are smaller than the smooth channel flow case.

Figure 5 shows 3D iso-surface plot of instantaneous vortical structure using Q-criterion for both channel flows for the lower channel wall. Reduced turbulence activity for the case of the Backswimmer channel flow is noticed. Also, for the Backswimmer geometry the pattern of the vortical elements have an elongated shape compared against the smooth spars which is consistent with drag reduction flows.

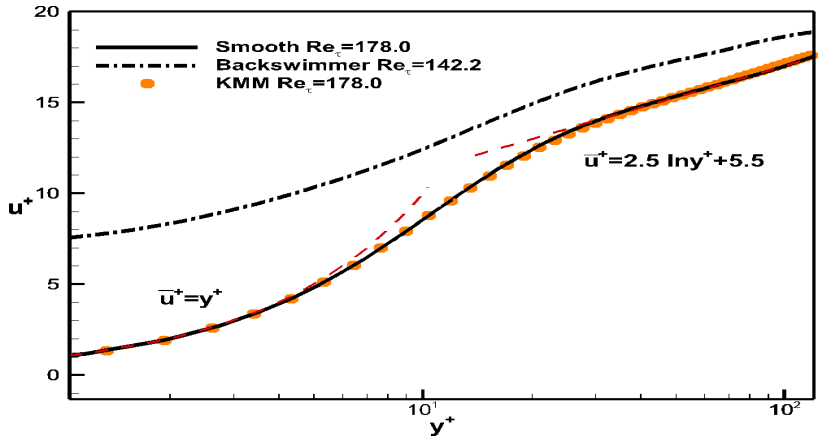

Figure 2 Variation of turbulence statistics for smooth and textured surface channel flow mean velocity profiles normalized by friction velocity $u_{\tau\tau}$ and validated against benchmark data [6].

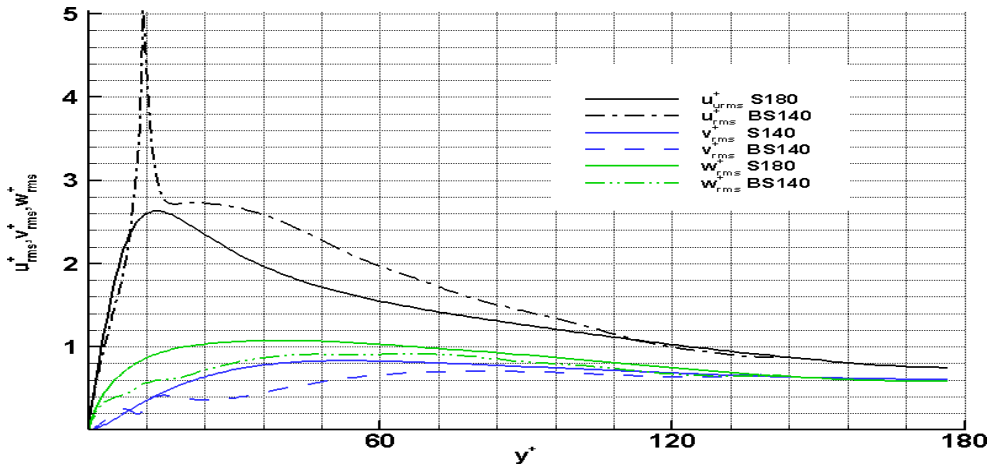

Figure 3 Variation of turbulence statistics for smooth and textured surface channel flow r.m.s. velocity profiles normalized by friction velocity $u_{\tau\tau}$.

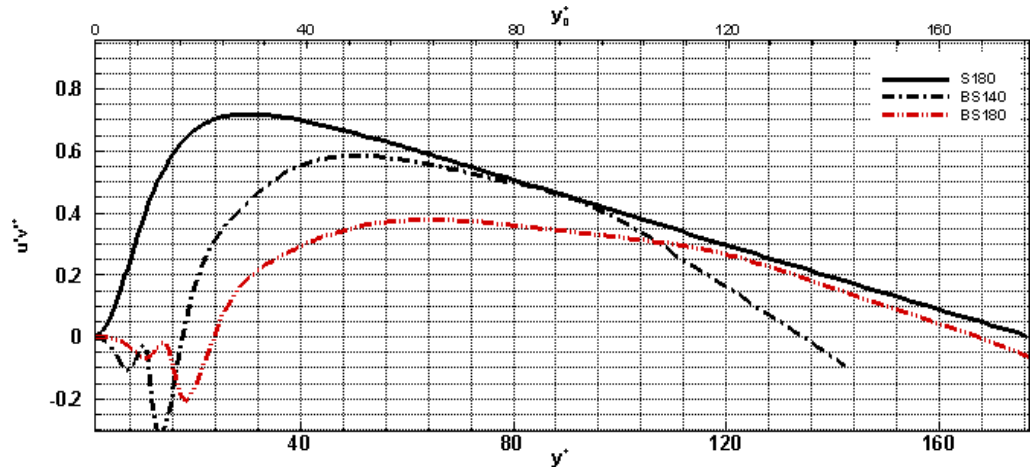

Figure 4 Variation of turbulence statistics for smooth and textured surface channel flow Reynolds shear stress profiles normalized by friction velocity u_{τ}^2.

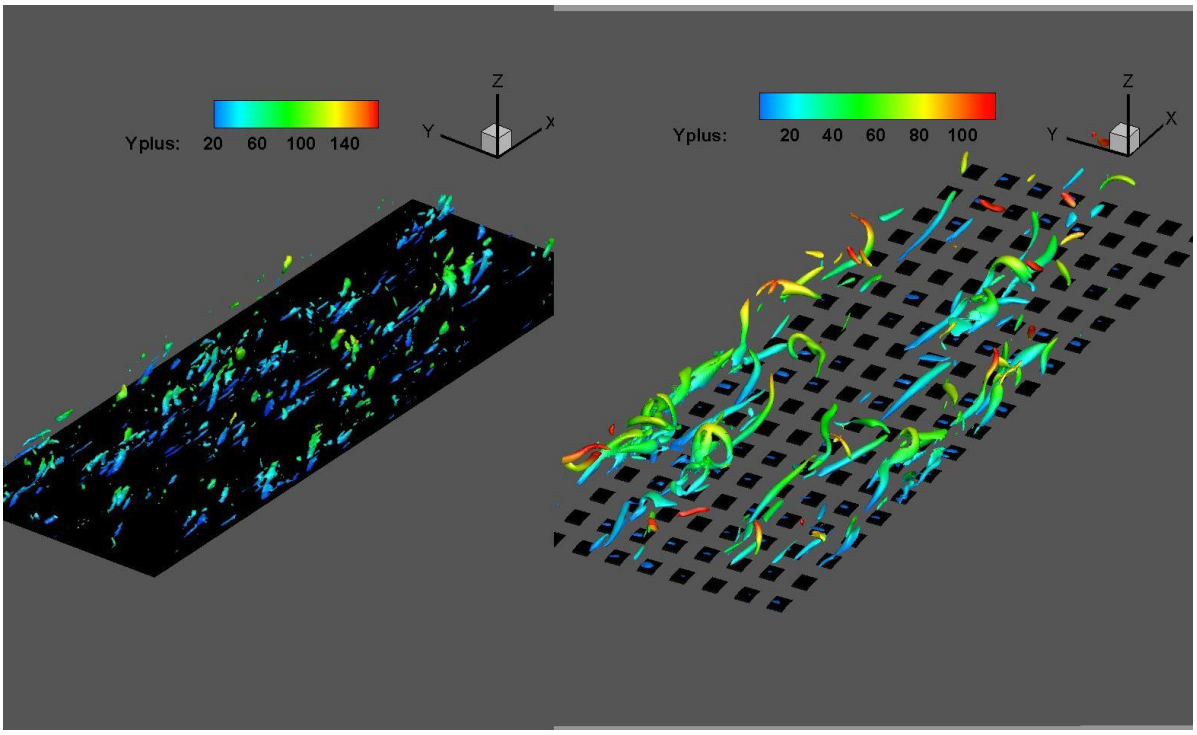

Figure 5 Near geometry vortical interactions at $\frac{Q}{u_\tau^4 Re_b^2} = 0.01$ *for both smooth and Backswimmer channel flows.*

Conclusions:

The Backswimmer geometry is potentially a drag reduction surface capable of achieving up to DR= 20.1% at low Reynolds numbers. The geometry was studied numerically using DNS in-house code in terms of mean velocity profiles, higher order turbulence statistics and iso-surface vortex interaction elements to understand the detailed flow structure of the novel geometry implementation. The results were consistent with the achieved drag reduction.

Acknowledgments:

The work made use of the UK National Supercomputer ARCHER sponsored by EPSRC through the UK Turbulence Consortium (EP/L000261/1).

References

[1] I. Arenas, E. Garcia, M. K. Fu, P. Orlandi, M. Hutmark, and S. Leonardi. Comparison between superhydrophobic, liquid infused and rough surfaces: A DNS study. *Journal of Fluid Mechanics*, 2018.

[2] B. Dean and B. Buhshan. Shark skin surfaces for fluid drag reduction in turbulent flow: a review. *Philosophical Transactions of the Royal Society*, **368**, 4775 - 4806, 2010.

[3] P. Ditsche-Kuruand E. S. Scneider, J. .E. Melskotte, M. Brede, A. Leder, and W. Barthlott. Superhydrophobic surfaces of the water bug notoncena glauca: A model for friction reduction and air retention. *Beilstein Journal of Nanotechnology*, **2**, 137 - 144, 2011.

[4] M. B. Martell, J. B. Perot, and J. P. Rothstein. Direct numerical simulations of turbulent flows over super hydrophobic surfaces. *Journal of Fluid Mechanics*, **620**, 31 - 41, 2009.

[5] R. G. Mayoral and J. Jimenez. Drag reduction by riblets. *Philosophical Transactions of the Royal Society*, **369**, 1412 - 1427, 2011.

[6] D. Moser, J. Kim, and N. N. Mansour. Direct numerical simulation of turbulent channel ow up to Re_ =590. *Physics of Fluids*, **11:4,** 943 – 945, 1991.

[7] H. Sasamori, H. Mamori, and K. Iwamoto. Experimental study on drag-reduction effect due to sinusoidal riblets in turbulent channel flow. *Experiments in fluids*, **55**, 18 - 28, 2014.

[8] M. Seddighi. Turbulence in transient channel flow. *Journal of Fluid Mechanics*, **715**, 60 - 102, 2013.

ISSN 2398-6611 (Online)

The effect of the increase of container carrier heavy goods vehicles on traffic flow operation and congestion

Ahmed Adnan Makki[a], Trung Thanh Nguyen[a], Jun Ren[a], William Hurst[b]
[a]Liverpool John Moores University, Department of Maritime and mechanical Engineering, LOOM Research Institute, James Parson Building, 3 Byrom street, Liverpool, L3 3AF, UK.
[b]Liverpool John Moores University, Department of Computer Science, James Parson Building, 3 Byrom street, Liverpool, L3 3AF, UK.
Email:T.T.Nguyen@ljmu.ac.uk

Abstract. The purpose of this paper is to investigate the impact of heavy goods vehicles that are carrying intermodal shipping containers on the traffic flow. The objective is to estimate the available capacity for heavy goods vehicles on the street to accommodate the increasing demand due to container terminal expansion. The author will utilise passenger car equivalence to determine the effect of the demand rise of heavy goods vehicles flow rate on road congestion. The results show that unless we create a new street, the traffic flow will suffer severe congestion and long periods of traffic jam, to avoid congestion, and maintain a seamless traffic flow of goods we need to create a new street of heavy goods vehicle access only and utilise urban consolidation centres. However, when considering containers with maximum payload weight or average to maximum payload volume, the traffic flow will run on very low speeds and long waiting periods.

Keywords. heavy goods vehicle, passenger car equivalence, road freight, urban consolidation centre, inland waterway, freight rail

1. Introduction

The expansion of the Liverpool container terminal increases the demand for road freight, and roads that connect the terminal with the city and the nearby cities will suffer from congestion. Therefore, local authorities either try to overcome this problem by building new roads, tunnels, adding extra lanes to existing roads, establishing consolidation centres or utilising other modes of transport for freight transportation. In order to reach a feasible solution, the planners would require an accurate and efficient method of estimating the effect of HGVs on road traffic flow.

It is essential to utilise the Passenger Car Equivalence (PCE) of HGVs, to obtain an accurate estimation of the road traffic capacity. The PCE value is the equivalent effect of a Light Goods Vehicle (LGV), a Rigid HGV (HGVr) or an Articulated HGV (HGVa) on traffic flow in comparison to the effect of Passenger Car (PC) vehicles. For example, if a truck requires three times the space and time that are needed by passenger cars, then one truck is said to have an equivalent of three passenger cars (PCE=3).

The authors have chosen the road under investigation because of the ongoing expansion of the container terminal of Liverpool. The collection of data is from (England 2017), conducted by automatic traffic counters. The utilised data contains traffic flow of vehicles with the length of ≤5.2 m, 5.21-6.6 m, 6.61-11.6 m, and ≥11.6 m and their average speed for every hour.

The target of the proposal for expanding Merseyside ports aims for processing an annual 2M TEUs[1] by 2020 and 3M TEUs by 2030. The proposed targets by Merseyside ports is that the freight rail and inland waterway would transport 10% and 5% of these containers respectively (PORTS 2011).

The number of existing annual TEUs processed in the year 2017 is 760.02kTEUs, and the TEUs entering the UK through the port hold 48.5% of the yearly TEUs in both directions. Therefore, we can assume that the annual TEUs that leave the container terminal to the UK mainland by utilising intermodal transportation is 368.61k TEUs.

Of all the road freight TEUs going to the UK through Liverpool container terminal, 22% go to Liverpool while 78% go to Manchester, North West Region, and the rest of the UK (Unit 2011; DfT 2017b; DfT 2017c; DfT 2017a; DfT 2018). By deducting the transported TEUs by rail and inland water modes (Unit

[1] TEU is a twenty-foot Equivalent Unit, and every TEU is equivalent to a 20 ft. intermodal shipment container

2011) (Merseytravel 2016)(PORTS 2018), the transported TEUs by road passing through the port's inland access (dunning bridge road) should be 244.39kTEUs by now, 643.11kTEUs by 2020, and 964.67kTEUs by 2030.
However, for the year 2017, the inland waterway freight has just transported 2.39% of TEUs and freight rail has only transported 1.642% of TEUs, which leaves 95.968% of TEUs that utilise road freight transportation by container carrier's HGV. Therefore, we should set the target for road freight according to the actual intermodal share, and they are 726.093kTEUs and 1089.14kTEUs for 2020 and 2030 targets respectively for inward road freight to the north-west and the rest of UK.

2. Intermodal Transportation

Intermodal freight transport involves the transportation of freight in an intermodal container, using multiple modes of transportation. The intermodal modes that we will discuss is rail, containership, and container carrier HGVs.

2.1. Freight rail

The utilisation of freight rail to distribute the transportation workload over several transportation modes. The rail freight line at the Liverpool port has a maximum length of 380m (63 TEUs) for every dispatch. The routes availability depends on the weight of the freight axle and the strength of underline bridges. Therefore, the freight rail will not be with enough capacity to overcome the increase of delivery demand unless the dispatch frequency and the number of rail lines increases.
Many issues can affect the maximum capacity of freight rail (Meadows 2018):

- Unloading/loading times for a ship and associated trains
- Available storage area while the containers are being transferred
- Number of cranes or grab stackers (big fork-lifts)

The maximum capacity of trains handling may or may not have commercial customers. For example, the terminal train plan may be able to handle five trains a day, but there might be only enough commercial traffic for one. The freight operating companies will bid for train paths to/from the port based on their commercial requirements.

2.2. Inland Waterway Freight

The inland waterway freight destinations are limited to the North West region and shares the same issues with freight rail. In addition, the tide and weather conditions affect the inland waterway freight operation and limit the number of deliveries. Besides, there are other operational barriers (IWA 2013), such as:

- Lack of appropriate continuing development of waterway infrastructure, for example, raising bridge headroom to facilitate the use of container barges
- Lack of operational experience in many types of industry, where transport managers are unfamiliar with processes, availability and costs, so rarely consider waterborne transport as an option
- Lack of knowledge about water-freight operational issues in some navigation authorities
- Inadequate promotion of waterborne freight as a modern transport mode
- Lack of immediate availability of suitable vessels or trained crew in some cases
- A planning system that does not adequately take account of waterway freight transport infrastructure needs at national, regional or local levels
- Lack of co-ordination between Government departments on waterborne freight transport matters

2.3. Road freight

The North West region is suffering from road congestion not only because of freight deliveries but also because of the continuous yearly increase of passenger car traffic flow. The urban congestion is one of the main issues especially in Liverpool, whereas the rise in demand for road freight due to the expansion of Liverpool container terminal. For example, the traffic flow at church road and Dunning Bridge road (A5036) have increased by 26% from May-2016-May-2017.
The increase in HGV access put pressure and limitation to the maximum heavy goods vehicles that utilise in this road, and more specifically the HGVs will increase congestion and the number of times that vehicles need to stop for every road link. Therefore, there is a plan by local authorities to create a new two-lane road to reduce congestion and pave the way to meet the 2020 and 2030 targets.

2.4. Urban Consolidation Centres

The utilisation of urban consolidation centres (UCC) will reduce the number of heavy and long vehicles flowing in city roads during peak hours by processing large containers at consolidation centres and making several of smaller amounts of deliveries by using smaller trucks of 2-3 axles and a maximum gross weight of 18 tonnes (Michael Browne 2007). Making deliveries with smaller trucks will reduce their effect on the traffic flow and make it easier to access roads, parking areas, unloading goods, and reducing the noise (Rooijen; Hans Quak 2010).

It will solve the last mile problem that occurs during the last mile of the delivery where the delivery location is inside the city. The last mile problem is one of the most expensive and challenging parts of urban freight distribution as it holds over 50% of the logistics cost (Leonardi 2014) (Julian Allen 2012). The adaption of UCCs will reduce the weight and length of the trucks used for delivery, thereby reducing their effect on road congestion, traffic flow speed, and increase their access and manoeuvring ability to make quick and efficient deliveries in the city centre (Bjorklund 2017). However, the UCC life span is usually 2-3 years, and this makes it an unreliable long-term solution and limits its benefits to short-term only.

3. Passenger Car Equivalence

The passenger car equivalence (PCE) value is the representation of the effect of non-passenger cars vehicles on the traffic flow in comparison to the impact of an average passenger car on the traffic flow. The utilisation of PCE value is essential in determining the road capacity because it provides the actual effect of a non-passenger car on the road and leads to a more realistic modelling solution.

4. Speed and Traffic Jam

To determine the effect of the increasing demand on road congestion, we need to estimate the traffic flow speed according to traffic flow density in PCE. According to (Greenshields 1935) traffic flow density has a linear relationship with traffic flow speed as shown in (1).

$$S = FFS * \left(1 - \frac{K}{K_j}\right) \quad (1)$$

Where,

S is the predicted traffic flow speed in km/h
FFS is the maximum flow speed in an empty road in km/h
K is the traffic flow density in PC/lane/km
K_j is the jam traffic density in PC/lane/km

5. Experiments

The author will explore six scenarios where the road freight meets the target for 2020 and 2030, and in all these scenarios we will consider maximum payload's weight, average payload's weight, and average payload's volume.

- Scenario 1: Utilising the existing two-lane road
- Scenario 2: Utilising a new HGV access only two-lane road
- Scenario 3: Utilising the existing two-lane road and a new all-access two-lane road.
- Scenario 4: Utilising UCC by accessing the existing road
- Scenario 5: Utilising UCC by accessing the new HGV access only two-lane street
- Scenario 6: Utilising UCC by accessing the existing and new two-lane all access streets

The results for scenario 1 show that increasing the access of HGVa up to the required demand level to meet the 2020 and 2030 targets without making a new street will lead to long periods of the traffic jam from 8 am to 10 am and from 1 pm to 5 pm as shown in figure 1a. Also, with higher payload weight the jam hours will increase from 6 hours a day to 11 hours a day as shown in figure 1b. In scenario 2, the results show more relaxed traffic flow speed with no traffic jam periods, because all the extra demand for HGV will utilise the new HGV access only two-lane street as shown in figure 1a and figure 1b. Scenario 3 results lower speeds than scenario 2 because the new street is all access and assumed to have the same traffic flow rates for non-HGV vehicles.

Scenarios 4-6 will involve replacing every HGVa with two HGVr when considering an average payload

volume of 80% while only one HGVr will replace an HGVa when considering the average payload weight of 7.28 tonnes per TEU. The results for scenarios 4-6 show the benefit of utilising UCC when considering an average payload weight as shown in figure 1c. However, when considering an average payload volume, we will get similar effects to scenario 1 where maximum payload weight is considered as shown in figure 1d.

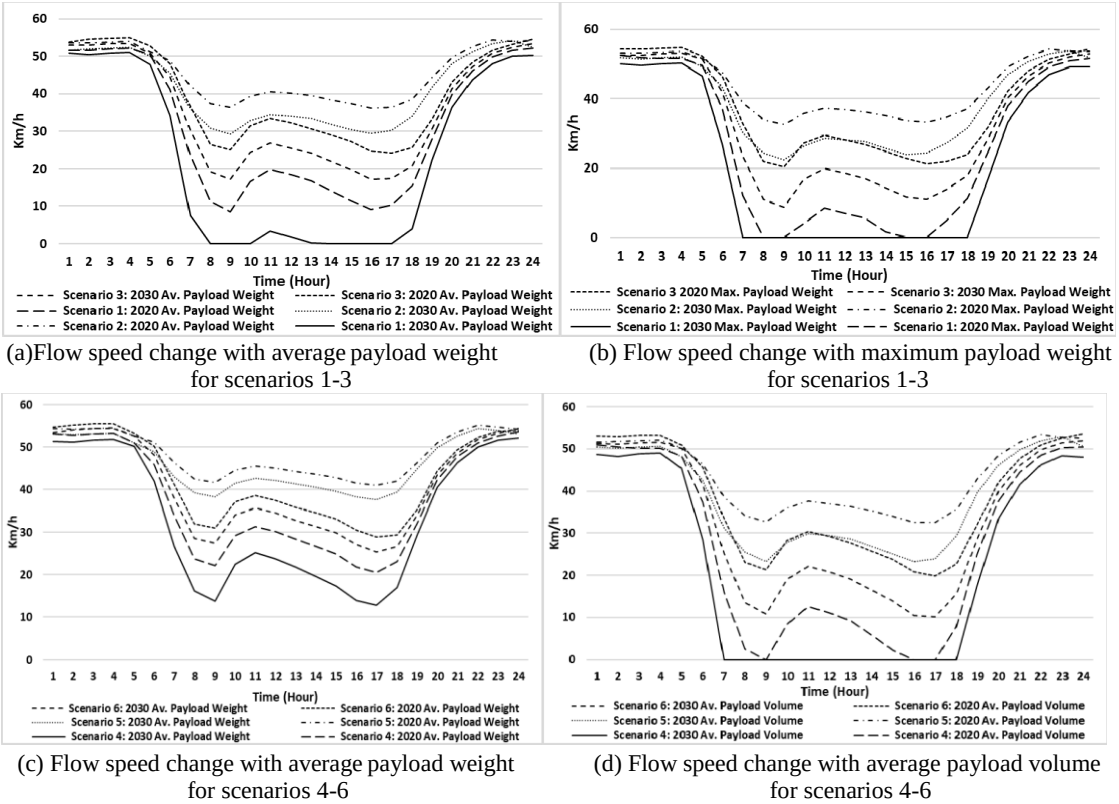

(a)Flow speed change with average payload weight for scenarios 1-3

(b) Flow speed change with maximum payload weight for scenarios 1-3

(c) Flow speed change with average payload weight for scenarios 4-6

(d) Flow speed change with average payload volume for scenarios 4-6

Figure 1: The change of average flow speed of traffic flow due to increasing of HGVs to meet the 2020 and 2030 targets

6. Conclusions

This paper showed the benefits of creating a new street to facilitate the intermodal transportation of shipment containers without making any further traffic congestion. However, utilising a new street of HGV access only will not be enough, and retailers, logistic companies, and local authorities will require creating an urban consolidation centre (UCC) to reduce the need for articulated HGVs and replace them with smaller HGVs. The utilisation of UCCs will help to maintain optimum flow speed and reduce waiting periods, and due to the short lifespan of UCCs. The authors have utilised the PCE value to obtain a realistic traffic flow rate. The UCC solution will not be available for long term, and it is essential to develop and increase the freight rail and freight inland waterway operation.

7. Reference

Bjorklund, H.J.M., 2017. Urban consolidation centres; retail stores' demands for UCC services. *International Journal of Physical Distribution & Logistics Management (IJPDLM)*, 47(7), pp.646–662.

DfT, 2017a. Statistical data set , Port freight (PORT02) : Port freight statistics tables. Available at: https://www.gov.uk/government/statistical-data-sets/port02-freight#table-port0204.

DfT, 2017b. *UK Port Freight Statistics: 2016 (revised)*, UK: Department for Transport.

DfT, 2018. *UK Port Freight Statistics: January to March 2018 (Quarter 1)*, UK: Department for Transport. DfT, 2017c. *UK Port Freight Statistics: July to September 2017 (Quarter 3)*, UK: Department for Transport. England, D.-H., 2017. Available Data Sources. Available at: http://tris.highwaysengland.co.uk/.

Greenshields, B.D., 1935. A Study of Traffic Capacity. *Highway Research Board*, 14, pp.448–447.

IWA, 2013. *IWA Policy on Freight on Inland Waterways*, The Inland Waterways Association. Available at: https://www.waterways.org.uk/information/policy_documents/freight_on_inland_waterways.

Julian Allen, J.L. Michael Browne Allan Woodburn, 2012. The Role of Urban Consolidation Centres in Sustainable Freight Transport. *Transport Reviews*, 32(4), pp.473–490.

Leonardi, J.A.M.B.A.W.J., 2014. A Review of Urban Consolidation Centres in the Supply Chain Based on a Case Study Approach. *The International Journal of Supply Chain Forum*, 15(4), pp.100–112.

Meadows, E., 2018. Freedom of Information Letter from Network Rail.

Merseytravel, 2016. *Freight Sites Neighbouring the Liverpool City Region*, Liverpool, UK: Merseytravel.

Michael Browne, J.A. Allan Woodburn, 2007. Evaluating the potential for urban consolidation centres. *European Transport*, (35), pp.46–63. PORTS, P., 2011. *Mersey Ports Master Plan: A 20 year Strategy for Growth*, Maritime Centre, Port of Liverpool L21 1LA: PEEL PORTS. PORTS, P., 2018. PEEL PORTS LAUNCHES FIRST RAIL FREIGHT SERVICE. Available at: https://www.peelports.com/news/2018/peel-ports-launches-first-rail-freight-service.

Rooijen; Hans Quak, T. van, 2010. Local impacts of a new urban consolidation centre– the case of Binnenstadservice.nl. *Social and Behavioral Sciences 2*, 2(3).

Unit, L.S., 2011. *The third Local Transport Plan for Merseyside, Annex 4:Freight Strategy*, Liverpool, UK: LTP Support Unit.

ISSN 2398-6611 (Online)

Effects of sampling cadence on structure function parameters of AGN optical light curves

Tricia Sullivan and Iain A. Steele
Astrophysics Research Institute, 146 Brownlow Hill, Liverpool, L3 5RF

t.sullivan@2015.ljmu.ac.uk

Abstract Active galactic nuclei (AGN) are variable point-like light sources associated with supermassive black holes. They reside in galaxy centres, where their stochastic energetic activity is implicated in regulating galaxy evolution. Because AGN variability is linked to black hole accretion, its characteristics may impose constraints on the emitting region size, black hole mass, accretion rate, etc. It is typically modelled by a damped random walk (DRW) whose features are parametrised by the structure function (SF) that measures root-mean-square flux change as a function of time lag. The SF is a bent power law with red noise on short-time lags and white noise on long lags. The literature has used survey data extensively to seek correlations of SF powerlaw index and amplitude with physical features of the system. However, survey photometry is collected in seasonal patterns. To explore impacts of sampling patterns from Sloan Digital Sky Survey (SDSS) Stripe 82 and Large Synoptic Survey Telescope (LSST), we generated simulated lightcurves, then removed data in accordance with survey sampling patterns. After fitting a powerlaw index to the first ~100 days of SFs, we find a systematic decrease in powerlaw index between even and cadenced sampling. Additionally, spurious substructure is introduced to the SF, complicating anticipated corrections.

Keywords: AGN variability, quasar structure function

1. Introduction

Stochastic optical variability is a hallmark of active galactic nuclei (AGN). It results when accretion of gas onto a central supermassive black hole (SMBH) emits radiation in a manner similar to a scaled-up X-ray binary [1]. AGN variability has been found to be well-fitted by a damped random walk (DRW) and its associated structure function (SF) [2]. The SF is a simple measure of emission variability amplitude as a function of time; for a DRW this is a bent power law with a red-noise regime on shorter timescales and a white-noise regime on long timescales. In theory $\gamma\gamma$ is ~0.5 for a DRW, but observations reveal a range of values for $\gamma\gamma$ [3], which constrains timescale of changes in accretion rate.

A number of attempts have been made to correlate red-noise power-law index $\gamma\gamma$ and white-noise maximum amplitude $\mathbb{S}\mathbb{S}_{\infty}$ with features of the AGN such as luminosity, SMBH mass and spin, radio-loudness, and Eddington ratio [4]. If accurate, these parameter relationships could elucidate accretion properties that are otherwise unobservable. However, while emission variability itself is stochastic, survey sampling patterns are not.

The upcoming Large Synoptic Survey Telescope (LSST) project will record 500 petabytes of data, including lightcurves for ~10 million AGN over ten years [5]. Here we examine the response of the SF to mock sampling effects based on proposed LSST observing cadences as well as the cadence of existing Sloan Digital Sky Survey (SDSS) Stripe 82 (S82) data. We simulate DRW light curves and fit a powerlaw to the SF's first 100 days to test whether sampling cadence impacts $\gamma\gamma$.

2. Data

We follow the method of [6], with variability timescale τ, dispersion σ, signal flux s_i and time lag between observations $\Delta t = t_{i+1} - t_i$ where i is an instance of time. We begin with a Gaussian deviate $s_i = G[\sigma^2]$ and then allow the subsequent terms to 'walk' while scaling variability by an exponential term (and similarly scaling the Gaussian itself) to ensure that the signal returns to the mean.

$$s_{i+1} = s_i e^{-2\Delta t/\tau} + G[\sigma^2\left(1 - e^{-\frac{2\Delta t}{\tau}}\right)]$$

Observational noise is simulated by a noise term ${n_i}^2$. The observed light curve is then

$$y_i = s_i + G[{n_i}^2]$$

ISSN 2398-6611 (Online)

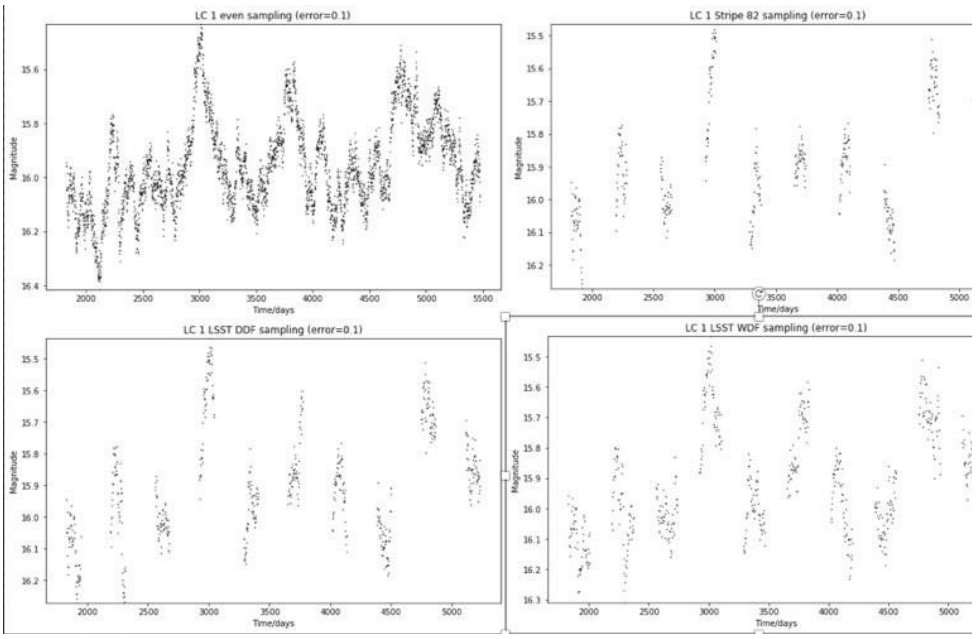

Figure 1 Example DRW lightcurve with sampling patterns (clockwise from top left): even, Stripe 82, DDF, WDF.

We produced 50 lightcurves (10×5 error levels 0.1 - 0.5) based on parameter values in [3] ($\pi = 500$, $\$\$_\infty = 0.18$) and length 75 $\tau\tau$ (~100 years) sampled daily. An initial 'burn-in' period of ~5 years was removed. We then censored selected data points based on three idealised annual observing cadences: SDSS S82 (alternate days for 90 days, off-target for 275 days) and proposed LSST cadences Wide Deep Fast (WDF—alternate days for 120 days, 245 days off-target) and Deep Drilling Fields (DDF—every third day for 182 days, off-target 183 days). We also used 6742 public lightcurves from [4] to obtain actual S82 sampling patterns as well as distributions on $\tau\tau$ and magnitude errors. We generated an additional 5000 DRW lightcurves using Monte Carlo simulations varying $\tau\tau$ as a Gaussian around 500 days consistent with [6]. Figure 1 shows examples.

3. Method

To test the effects of sampling, SFs were constructed by comparing each lightcurve with a time-shifted version of itself where the shift was performed repeatedly with incrementally increasing time lags. For any given lag, root-mean-square difference of all values of flux between original and shifted lightcurves was calculated to yield a single value for each lag. We fitted a powerlaw up to lags of 100 days (the approximate length of unbroken sampling). We aggregated and compared $\gamma\gamma$ for each set of data. After observing that S82 suffered the most egregious effects, we compared $\gamma\gamma$ for a single evenly-sampled SF to its analogue when subjected to the *actual* sampling recorded by [4] from 6742 real S82 lightcurves. Finally, we performed the same steps comparing even sampling to idealised S82 sampling for 5000 Monte Carlo simulated DRW lightcurves.

4. Results

For the initial batch of 10 lightcurves there are two effects of introducing periodic sampling cadence to inherent DRW stochastic variability. The first is systemic reduction in $\gamma\gamma$ (see figure 3) by 13 - 48% depending on cadence, and the second is the introduction of unphysical substructure (see figures 2 and 5). In addition to imposing periodicity on a white-noise process, the substructure renders ambiguous any measurement of the turnover from red to white noise.

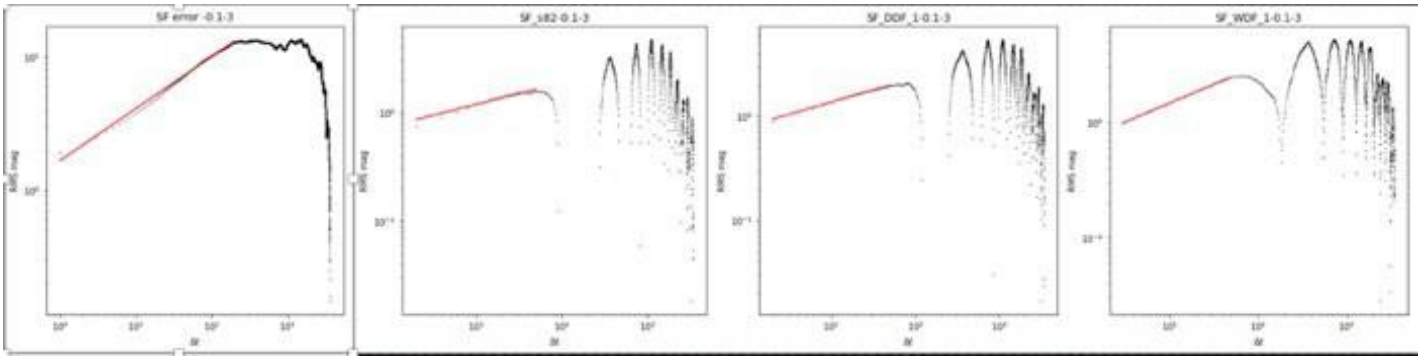

Figure 2 Logarithmic plots of example SFs from (left to right): evenly sampled, S82, LSST DDF, LSST WDF with time lag on the x-axis and RMS variability on the y-axis and power law fits in red. We note that the precipitous drop in SF at high lags is not a result of cadencing and ignore it for the moment.

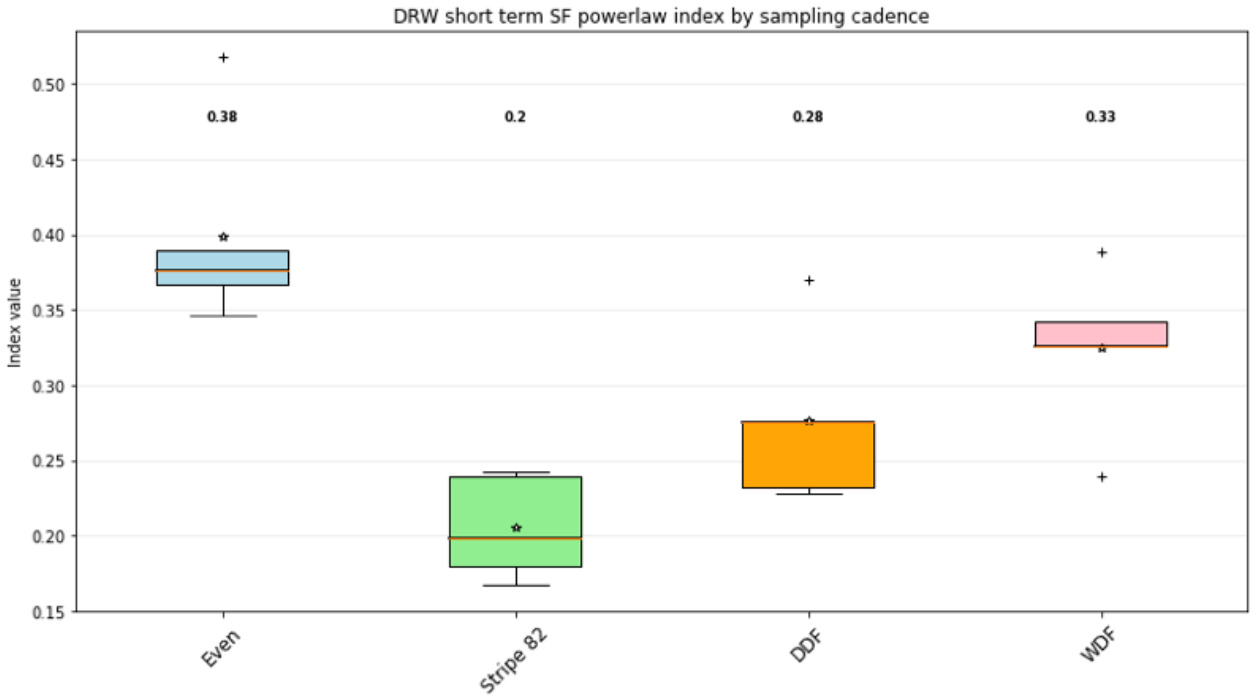

Figure 3 (left) Boxplots showing powerlaw indices for SFs given each sampling cadence. The mean for each index is printed above the box. S82 suffers the greatest decrement in γ and the largest scatter.

We note that even sampling resulted in mean $\gamma = 0.38$ for 10 lightcurves, which is less than the expected $\gamma = 0.5$, likely due to small sample size. For the 5000 S82 lightcurves generated by Monte Carlo simulations, median $\gamma = 0.46$, in line with expected DRW, with a drop to $\gamma = 0.33$ (-30%) when switching to S82 cadence.

When we simulated a single DRW lightcurve and then subjected it to the individual sampling for each observed S82 object, the effect on the SF was more dramatic. The original SF has $\gamma\gamma = 0.41$ and the actual sampling patterns produce SFs with mean $\gamma\gamma = 0.11$(- 73%) as well as a large scatter (fig 4). In some cases data turn out to be extremely sparse and/or the length of the survey is too short for that particular object's SF to be properly measured.

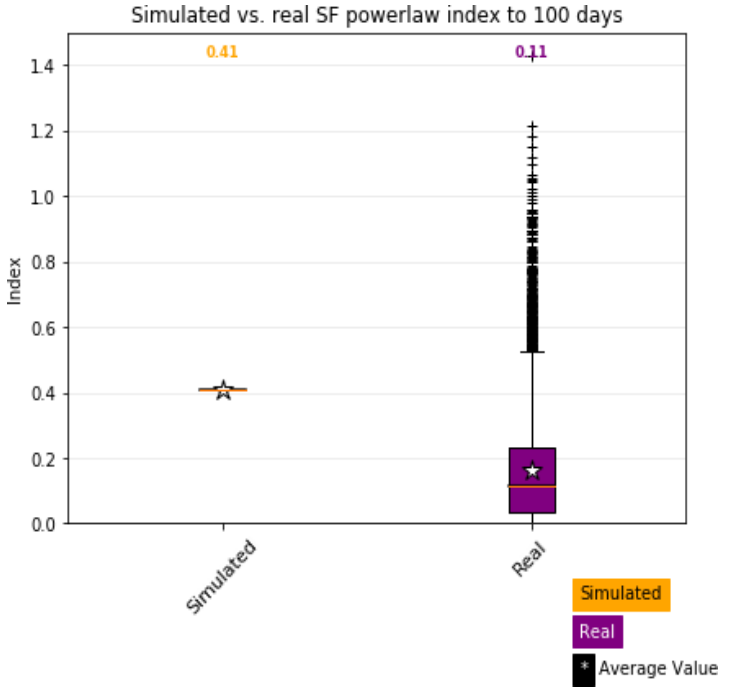

Figure 4 Powerlaw indices for one evenly-sampled DRW SF before and after censoring according to real S82 data.

5. Discussion

In fitting a power law to the first 100 days of a simulated lightcurve's SF, we observe a negative offset between $\gamma\gamma$ for periodically censored (cadenced) data versus uncensored. The shorter the observing season, the more dramatic the offset. For S82 data, the limitations of real (sparse/short-length) sampling on characterising the SF are apparent in figure 4 and do not need much interpretation.

By fitting to the first 100 days only we have ensured that our estimate of $\gamma\gamma$ does not depend on amplitude reaching the white-noise regime SF_∞. We therefore envisaged a straightforward correction to observed $\gamma\gamma$ given π, SF_∞ and sampling cadence. However, it is impossible to constrain SF_∞ from the cadenced lightcurves because the so-called white-noise regime of the SF exhibits a series of regular peaks interspersed with gaps.

Additionally, for some lightcurves in the Monte Carlo sample a spurious initial peak occurs within 100 days, leading to an overestimate of SF_∞ and an underestimate of turnover time in the cadenced SF (see figure 6). The result suggests that cadencing imposes unpredictable inaccuracies in SF_∞ in a manner that obviates a simple offset correction for either γ or SF_∞. To make progress, we require an outcome in which intelligent but automatic corrections to SF parameters are

possible given a lightcurve and a known cadence. A deep-learning approach may be suitable for the next stage of tackling the problem.

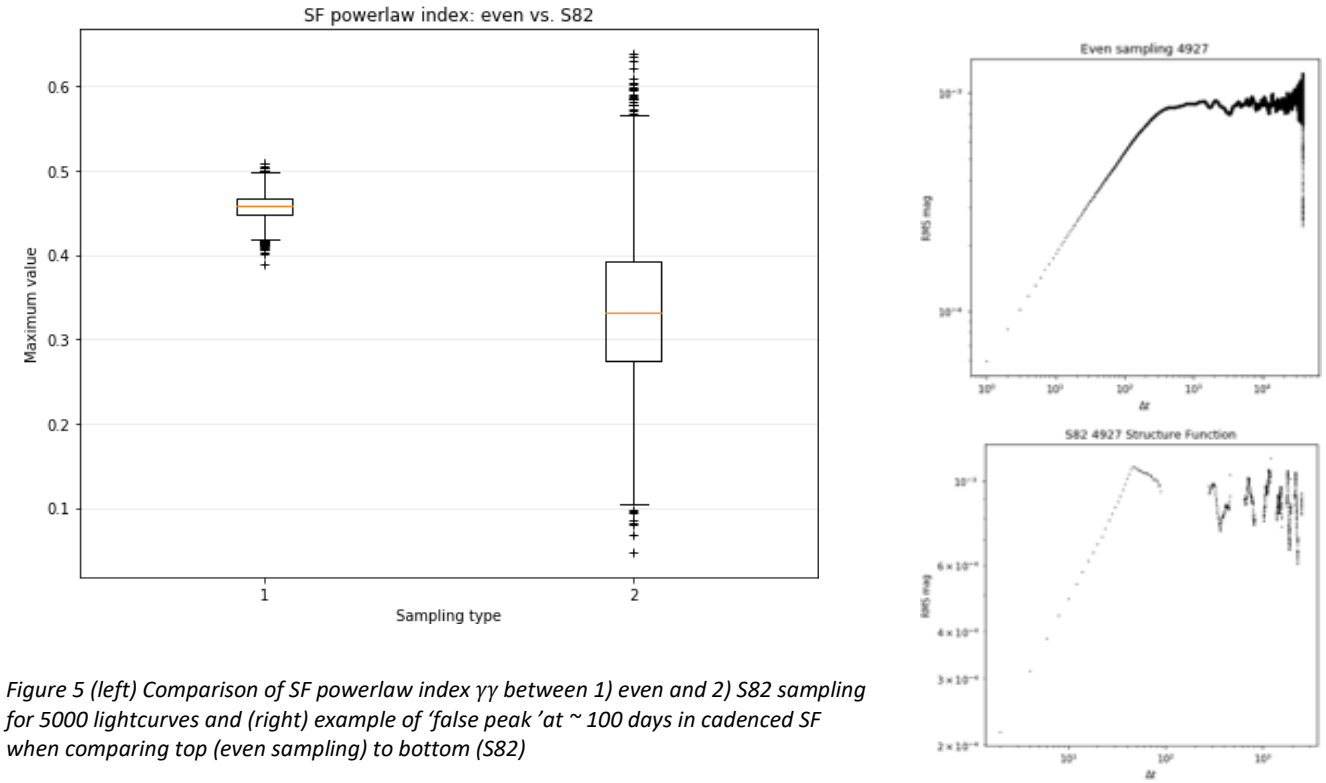

Figure 5 (left) Comparison of SF powerlaw index γγ between 1) even and 2) S82 sampling for 5000 lightcurves and (right) example of 'false peak 'at ~ 100 days in cadenced SF when comparing top (even sampling) to bottom (S82)

6. Conclusion

To investigate the effect of cadenced sampling on SFs, we have simulated evenly-sampled DRW lightcurves and censored them to produce mock observing cadences based on SDSS Stripe 82 and LSST proposed WDF and DDF surveys. We compared the red-noise regime powerlaw indices between evenly-sampled SFs and their cadenced counterparts. We find a decrement in the powerlaw index $\gamma\gamma$ for all three cadences, with $\gamma\gamma$ losing up to 48% of its value under S82 sampling. Applying actual S82 sampling patterns from real data to a simulated DRW lightcurve resulted in a drop of 73% for $\gamma\gamma$, with notable increase in scatter. Finally, when using a sample of 5000 DRW lightcurves the change in $\gamma\gamma$ is -30%. Visual inspection reveals that measuring long-lag amplitude $\$\$\$_\infty$ is problematic due to the presence of unphysical structure in the cadenced SFs, and the dependence of $\$\$\$_\infty$ on $\tau\tau$ adds another layer of complication. We cannot offer a correction based on conventional analysis at this time, but there is some reason to hope that deep learning can be implemented to address the sampling effects. We propose to address this task as a next step.

7. Acknowledgements

TS thanks M. Lam for technical help and P. McWhirter for instructive conversations on machine learning. TS was supported by the STFC [ST/P006752/1]. The LIV.DAT Centre for Doctoral Training (CDT) is hosted by Liverpool John Moores University/Astrophysics Research Institute and the University of Liverpool.

8. References

[1] McHardy, I, Uttley P, Taylor R & Papadakis I 2006 *Proc. ASP Conference Series 2004*, Crimea, Ukraine **360** 85 ed. Gaskell M et al.
[2] Kelly B, Bechtold J & Siemiginowska A 2009 *ApJ* **698** 895-910
[3] Kasliwal V, Vogeley M & Richards G 2015 *MNRAS* **451** 4328-4345
[4] MacLeod C et al. *ApJ* **721** 1014-1033
[5] LSST https://www.lsst.org/about/timeline
[6] Kozlowski, S 2017 *ApJ* **826** 118

ISSN 2398-6611 (Online)

Advanced Control of a Symmetrical Nine-phase PMSM with Non-Sinusoidal Back-EMF Using Harmonic Current Injection

M. Slunjski
Department of Electronics and Electrical Engineering,
James Parsons Building, Byrom Street, L3 3AF, Liverpool, UK
m.slunjski@2017.ljmu.ac.uk

Abstract. The research conducted in this work investigates advanced vector (field oriented) control method of a two-pole surface permanent magnet synchronous machine (PMSM) with a symmetrical nine-phase winding configuration. Magnets on rotor are shortened which causes production of highly non-sinusoidal back-electromotive force (EMF) in the stator windings. Corresponding FFT analysis of the recorded EMF reveals a high third-harmonic component, which is almost equal in magnitude to the fundamental. Harmonics with similar magnitudes have been used by researchers in the past to improve fault-tolerant operation and to increase electromagnetic torque of the multiphase machines. By investigating the possible torque improvements using finite element method (FEM) software tool, it was shown that electromagnetic torque of the studied PMSM can be improved for additional 36%. To control the real machine in experimental setup, field-oriented control (FOC) algorithm adjustments needed for third-harmonic current injection control implementation are therefore in this work investigated and a high-performance control algorithm for studied PMSM is derived and implemented.

Keywords. Multiphase drives, surface PMSM, symmetrical nine-phase machine, non-sinusoidal back-EMF, advanced field-oriented control, third-harmonic current injection.

1. Introduction

In the last two decades, the need to reduce production cost and at the same time achieve better performance, as well as new safety regulations for fast growing industry of more- and all-electrical vehicles, have directed research interests towards machine configurations with more than three phases. These, so called, multiphase machines are therefore today well recognized as an attractive alternative to the conventional three phase machines. If compared with three-phase counterparts, multiphase machines offer various benefits such as higher fault-tolerant capability, higher torque density, smaller per-phase power/current and additional degrees of freedom that can be used for control purposes that are not possible in standard three-phase machines (Levi et al, 2007; Levi, 2016; Parsa, 2005).

Nowadays, a high torque capability is highly desirable for the electric machine drives in growing industries such as electrical vehicles, ship propulsion and electric/more electric aircraft. Harmonic currents injection to the stator which is possible due to the additional degrees of freedom that multiphase machine possess is one of the well-known techniques used for this purpose. In this method, the torque is enhanced using odd harmonic currents which couple with the back-EMF. A five-phase PMSM with concentrated windings and almost trapezoidal back-electromotive force was studied in (Parsa and Toliyat, 2005; Parsa et al, 2005). The investigated drive is supplied with combined sinusoidal plus third-harmonic currents and the motor is able to produce the same torque as an equivalent brushless dc motor; however, it overcomes disadvantages such as torque ripple and complex control above the base speed region. In (Parsa, 2005b), this so called 5BPM, was applied in a ship propulsion system, while in (Parsa et al, 2005), the same harmonic injection principle was used to investigate the field-weakening performance of the machine and a suitable field-oriented control scheme was developed. The recorded torque improvements using third-harmonic current injection were in the region of 10-17%.

In (Zhao and Yang, 2011), a 20% torque increase was recorded with the same torque quality, while for different adaptations of rotor investigated in (Wang et al, 2014; Sadeghi et al, 2014) the achieved improvement was in the range between 9-17%, while keeping the same RMS current. In (Aslan and Semail, 2014), a low voltage five-phase PMSM was designed and tested for automotive applications.

The machine's rotor is designed and controlled to produce third-harmonic EMF to link with the high third-harmonic magneto-motive force produced by the stator windings. In the base speed region, the machine control uses both harmonic currents, producing 33% higher torque with the same volume.

In this paper, an advanced high-performance field-oriented control algorithm is derived to control a nine-phase PMSM with a 36-slots stator and with a shortened 2 poles magnet rotor. As shown in (Slunjski et al, 2018) where the investigated machine was analysed in detail using a finite element method software tool, the rotor structure gives rise to a highly non-sinusoidal back-EMF. As a result, a third-harmonic component almost equal to the fundamental is produced. Based on conclusions presented in mentioned work, it is shown that for the studied machine, electromagnetic torque produced only by the fundamental component can be increased by 36% using third-harmonic current injection. To validate the theoretical torque improvement, an advanced field-oriented control algorithm which, in additional to fundamental, applies and third-harmonic current control is in this work derived.

2. Control of a multiphase PMSM machine with highly non-sinusoidal back-EMF

Modelling of the investigated multiphase PM synchronous machine with highly non-sinusoidal back-EMF and corresponding high-magnitude low-order harmonic spectrum (Figure 1a) was presented in detail in (Slunjski et al, 2018). The same machine model is used in this work to validate the possible (36%) torque improvements. To control the symmetrical nine-phase PMSM, an advanced field-oriented control algorithm in synchronous domain is implemented. To transform the phase variables model to rotational domain where FOC can be implemented, vector space decomposition (VSD) matrix and modified Park's rotational transformation are used. From given spectrum in Figure 1a, fundamental and third harmonics are used for torque production and enhancement by applying third-harmonic current injection. The other harmonic components, such as the 5th and the 7th are not considered in this work, and so they must be mitigated to avoid induction of loss producing currents. Vector proportional integral (VPI) controllers are used for this purpose (Yepes et al, 2015).

Implementation of the third-harmonic current injection control requires modification of the well-known field-oriented control algorithm. In the case when only fundamental harmonic component is considered, two current components (i_{d1} and i_{q1}) exists and must be controlled. Other current harmonic components in additional sub-plains are then not of concern and are usually ignored or eliminated if they exist. If third-harmonic current component is also desired to be controlled (e.g. torque improvement reason, fault tolerant control), an additional two current components (further addressed as i_{d3} and i_{q3}) must also be taken into consideration. To perform maximum torque-per-ampere control in PMSM, flux-producing current component references are set (and controlled) to zero ($i_{d1} = 0$ and $i_{d3} = 0$). Total electromagnetic torque in the machine is then produced as the sum of two torque-producing parts i.e.:

$$T_{em13} = T_{em1} + T_{em3}; \quad T_{em1} = \frac{n}{2} \cdot P \cdot \lambda_{m1} i_{sq1}; \quad T_{em3} = \frac{n}{2} \cdot P \cdot 3 \cdot \lambda_{m3} i_{sq3} \tag{1}$$

In (1), both torque-producing parts were obtained using corresponding equivalent electric circuit which can be found in Figure 1b. In equations, n is the number of stator phases, P is the number of rotor pole-pairs, R_s is the stator resistance, while λ_{sx}, λ_{mx} / $L_{sd} = L_{sq}$ stands for flux/inductance. For ease of implementation, these currents can be replaced with their ratio i_{q3}/i_{q1}, i.e. constant k. After short mathematical manipulation, relation between fundamental torque-producing current i_{q1}, electromagnetic torque T_{em13} and ratio k suitable for FOC implementation can now be written as:

$$k = \frac{i_{q3}}{i_{q1}}; \quad i_{q1} = \frac{2}{n \cdot P} \cdot \frac{T_{em13}}{\lambda_{m1} + 3 \cdot \lambda_{m3} \cdot k} \tag{2}$$

2
)

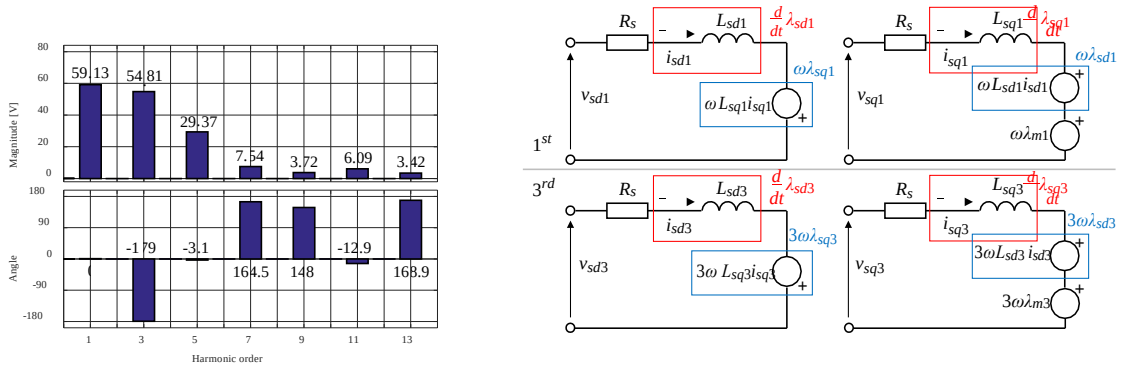

(a) (b)

Figure 1: FFT of back-EMF (a), and equivalent electric circuit of PMSM for 1st and 3rd harmonics.

In new control, VSD matrix will stay unchanged but rotational transformation matrix responsible for i_{xy3} to i_{dq3} transformation must be modified by adding third-harmonic component angle phase shift determined using FFT (Figure 1a). To determinate optimal k ratio, the classical maximum torque-per-ampere control strategy can be applied i.e. the maximum electromagnetic torque value per given RMS current can be calculated. As it turns out, the result of optimization gives optimal ratio between the two harmonic components to be e_3/e_1 (where e stands for back-EMF FFT component). Based on the given data in Figure 1a, it is easy to conclude that the exact value of the ratio between fundamental and third-harmonic for optimal current harmonic injection must be $k_{opt} = 0.927$. The complete FOC algorithm for the symmetrical nine-phase PMSM, with third-harmonic current injection is shown in Figure 2.

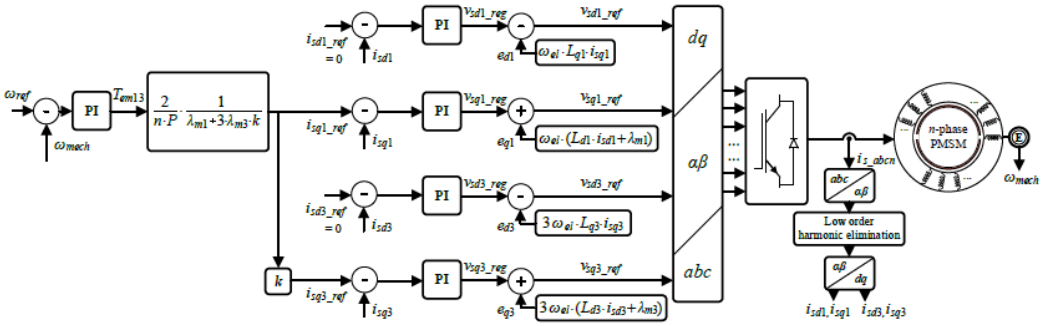

Figure 2: Advanced field-oriented control of PMSM with highly non-sinusoidal back-EMF.

3. Simulation Results

The control system was validated using simulations. The testing sequence is such that the machine is first supplied using only the fundamental current component, called first or $k = 0$ region. Next, the fundamental and third harmonic injection are used with the optimal current injection ratio k, called second or $k = 0.93$ region. The applied torque and speed command remain constant throughout, and so the phase RMS current changes its value. In Figure 3a, the machine's electromagnetic torque and mechanical speed are shown. It can be seen that the torque is constant during the whole testing time with the corresponding value 2 Nm. In transient, at t = 0.25 s, a small torque oscillation can be seen. This is directly related to instantaneous k ratio change, i.e. required system adaptation time. Mechanical speed is also kept constant during entire sequence, which therefore results in constant output power. In Figure 3b the phase currents waveforms are shown. It is important to note that although all nine phase current signals were used in system analysis, only waveforms of first phase in each phase set (i.e. phases $a1$, $a2$, $a3$) are shown in this figure. During the interval, t = 0 to 0.25 s, $k = 0$ region, the phase current is sinusoidal with an approximate peak value of 1.16 A. In the second region, after the current injection ratio was changed to $k = 0.93$, a similar current peak value can be seen, but this time with the shape which is, as expected, following the shape of the machine's back-EMF. It can be concluded from the RMS current analysis that with third harmonic injection, current is for $k = 0.93$ case (0.60 A) lower than the value calculated in $k = 0$ case (0.81 A). This means that the power losses are reduced i.e. there is lower power on the input terminals of the machine (output power is constant). If the decrease in RMS

current is calculated as a percentage, as expected, the new value is ~ 36% lower than the one calculated for the case when $k = 0$. Flux- and torque-producing currents in synchronous domain can be seen in the Figure 3c. Flux-producing currents i_{d1} and i_{d3} are set and controlled to 0. In the region before optimal coefficient change, only fundamental torque-producing current component i_{q1} is used for torque production and recorded dc current value in this region is approx. $i_{q1} = 1.16$ A ($I_{RMS} = 0.81$ A). As expected, after third-harmonic current injection ratio is changed to its optimal value fundamental current component decreases to $i_{q1} = 0.62$ A while at the same time, third-harmonic torque-producing current is changed from $i_{q3} = 0$ A to $i_{q3} = 0.58$ A ($I_{RMS} = \sqrt{(i_{q1}^2 + i_{q3}^2)}/2 = 0.60$ A).

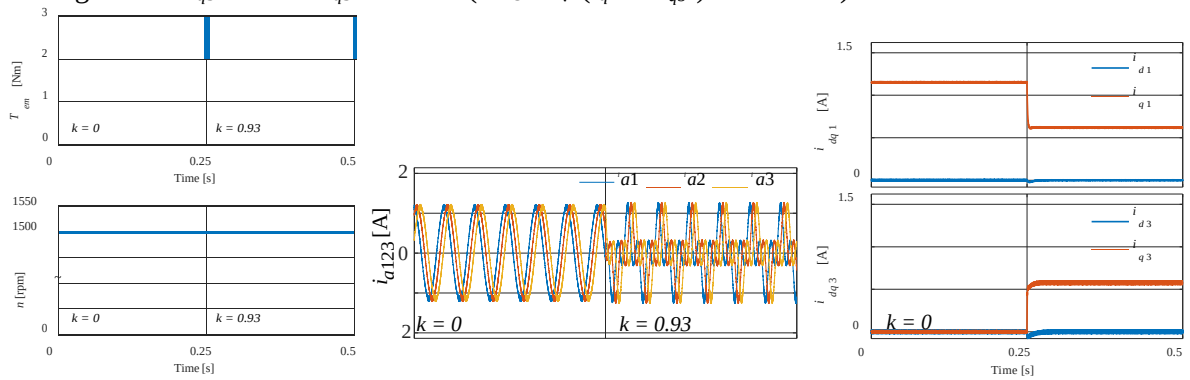

(a) (b) (c)

Figure 3: Simulation results obtained after machine testing under advanced control algorithm.

4. Conclusion

In this paper, an advanced high-performance field-oriented control algorithm for a nine-phase PMSM with a specific rotor structure is derived. Third-harmonic current injection control was successfully implemented, and hypothesised torque improvements analysed originally in [9] were confirmed. Detailed simulation results were also presented and analysed. In future work, other low-order high-magnitude odd harmonic components are going to be studied for additional torque enhancement and over nominal speed control improvement.

References

Aslan, B. and Semail, E. (2014) New 5-phase concentrated winding machine with bi-harmonic rotor for automotive application. *International Conference on Electrical Machines (ICEM)*, 2114-2119.

Levi, E. (2016) Advances in converter control and innovative exploitation of additional degrees of freedom for multiphase machines. *IEEE Transactions on Industrial Electronics*, 63 (1), 433-448.

Levi, E., Bojoi, R., Profumo, F., Toliyat, H.A. and Williamson, S. (2007) Multiphase induction motor drives - a technology status review. *IET Electric Power Applications*, 1 (4), 489-516.

Parsa, L. (2005) On advantages of multi-phase machines. *31st Annual Conference of IEEE Industrial Electronics Society*, 1574-1579.

Parsa, L. and Toliyat, H. A. (2005) Five-phase permanent magnet motor drives for ship propulsion applications. *IEEE Electric Ship Technologies Symposium*, 371-378.

Parsa, L., Kim, N., Toliyat, H. A. (2005) Field weakening operation of high torque density five-phase permanent magnet motor drives. *IEEE International Conference on Electric Machines and Drives*, 1507-1512.

Sadeghi, S., Mohammadpour, A. and Parsa, L. (2014) Design optimization of a high performance 5-phase slotless PMSM. *International Symposium on Power Electronics, Electrical Drives, Automation and Motion*, 6-11.

Slunjski, M., Jones, M. and Levi, E. (2018) Analysis of a Symmetrical Nine-phase Machine with Highly Non-Sinusoidal Back-EMF. *44th Annual Conference of the IEEE Industrial Electronics Society*, 6229-6234.

Zhao, P. and Yang, G. (2011) Torque density improvement of five-phase PMSM drive for electric vehicles applications. *Journal of Power Electron*, 11, 401-407.

Yepes, A. G., Malvar, J., Vidal, A., López, O. and Doval-Gandoy, J. (2015) Current harmonics compensation based on multi-resonant control in synchronous frames for symmetrical n-phase machines. *IEEE Transaction of Industrial Electronics*, 62 (5), 2708-2720.

Wang, W., Zhu, Z. Q. and Ombach, G. (2014) Torque enhancement of surface mounted permanent magnet machine using third-order harmonic. *IEEE Transaction on Magnetics*, 50 (3), 104-113.

ISSN 2398-6611 (Online)

F-EM sensors for monitoring continuously trace metals in mine-impacted water

I Frau[1], **S Wylie**[1], **P Byrne**[2], **J Cullen**[3] **and A Mason**[4]
[1]Built Environment and Sustainable Technologies (BEST) Research Institute, Department of Civil Engineering, Faculty of Engineering and Technology, Liverpool John Moores University, Liverpool, L3 3AF, UK.
[2]Department of Geography, School of Natural Sciences and Psychology, Faculty of Science, Liverpool John Moores University, Liverpool, L3 3AF, UK.
[3]Built Environment and Sustainable Technologies (BEST) Research Institute, Department of Built Environment, Faculty of Engineering and Technology, Liverpool John Moores University, Liverpool, L3 3AF, UK.
[4]Animalia AS, Norwegian Meat and Poultry Centre, PO Box Økern, 0513 Oslo, Norway

E-mail address: i.frau@2016.ljmu.ac.uk

Abstract. Trace metals, such as Zn, Cu, Pb, Cd are polluting global water supplies. Active and abandoned mining area are one of the major sources of the pollution. Continuous detection of these inorganic pollutants currently remains infeasible, limiting the understanding of the dynamics of an unexpected pollution event. Consequently, the aim of this work is to develop a novel sensing system based on microwaves and planar sensors that functionalised with specific coatings (f-EM sensors) for in-situ monitoring of Cu in freshwater.
The reflection coefficient was measured using both laboratory based, non-portable and portable Vector Network Analysers (VNAs) between 100 MHz and 3 GHz. The sensing system was waterproofed for in-situ monitoring. Acquired samples were spiked with a Cu solution using the standard addition method.
Results demonstrate that coatings based on l-cysteine, chitosan and bismuth-cobalt-zinc oxides were able to detect changes in Cu concentration and determine the unknown concentrations at two specific frequencies, 0.47 and 0.96 GHz with linear correlation given R^2= in the range 0.90-0.97.
This novel f-EM sensing platform will be able to qualify and quantify metal pollution in complex freshwater, in-situ with continuous monitoring.

Keywords. Copper, f-EM sensors, Lorentz peak function, standard addition method

1. Introduction

1.1. Metal pollution in water

Cu is among the most common toxic elements associated with mine waste and have been widely documented to cause significant pollution of water resources [1]. It is an essential element for living organisms, but in high concentrations, especially with long-term exposure, it can generate significant health problems, including respiratory, gastrointestinal and neuronal disorders [2].

1.2. Inadequate monitoring

Currently, no method is able to monitor water resources accurately and continuously. Recognised methods require samples to be collected in the field and taken to a laboratory, which involves pre-

sample analysis treatments, trained staff, and expensive consumables. Efforts are being made to develop sensing system for in-situ metal analysis of water resources. Some good improvements have been achieved with voltammetry [3], fluorescence and colourimetric [4] techniques. However, one of the biggest challenges is to develop a sensing system able to detect trace metals continuously.

1.3. Microwaves and f-EM planar sensors

Microwave spectroscopy has emerged in recent years as a novel monitoring technique that is able to determine the presence and concentration of specific components and pollutants in water. The advantages of this technique include the immediate response and its low power and measurement costs. Between the numerous resonant structures, planar sensors have the potential to give high sensitivity and accuracy [5]. Moreover, they are portable, light, and practical for in-situ and continuous monitoring, compared with resonant cavities, and can be easily implemented using thin and thick films, microfluidic structures, etc [6].

For a sensing perform with higher sensitivity (to detect lower Cu concentration) and selectivity (to distinguish between similar metal ions), the integration of thick film on planar sensors is a novel and attractive approach for microwave spectroscopy.

The objectives described in this paper are to use f-EM sensors based on L-CyChBCZ for Cu detection in complex water matrices and to compare the responses of a laboratory and a hand-held VNA.

2. Materials and Method

2.1. Coating development

8-pair gold interdigitated electrodes (IDE) printed on PTFE substrates were functionalised using a semi-automatic screen-printer (Super Primex) as described by Frau, Wylie, Byrne, Cullen, Korostynska and Mason [7], with a paste mixture based on l-cysteine, chitosan and bismuth cobalt zinc oxide (acronym: L-CyChBCZ). These materials in powder form were mixed with a binder and a few drops of a solvent for achieving the correct viscosity for printing. In this work, the f-EM sensors were covered with a 65 µm thick film (figure 1a). Then, they were waterproofed using a thermoplastic adhesive and embedded in 50 mL centrifuge tube lids.

2.2. Samples and standard addition method

The standard addition method is a quantitative method for determining the concentration of an analyte. The principle is based on the addition of the pollutant under test by adding multiple volumes of it to minimise the matrix effect which can interfere with the pollutant under test [8].

Water samples from a mining-impacted areas in and Central Wales, as Frongoch adit (acronym: FA) (Wamyss mine), were collected and spiked by a continuous standard addition of 1 mL of 100 mg/L Cu solution into a 80 mL sample. This corresponded to an increase of 1.25 mg/L in Cu concentration.

2.3. Measurements

Samples were analysed by immersing the f-EM sensor based on LCyChBCZ in the water sample. The reflection coefficient magnitude ($|S_{11}|$), was measured between 10 MHz and 3 GHz using two different Vector Network Analysers (VNA): a non-portable Rohde and Schwarz ZVA24 and a portable miniVNA tiny (mini Radio Solutions) (figure 1b). The EM response was recorded continuously.

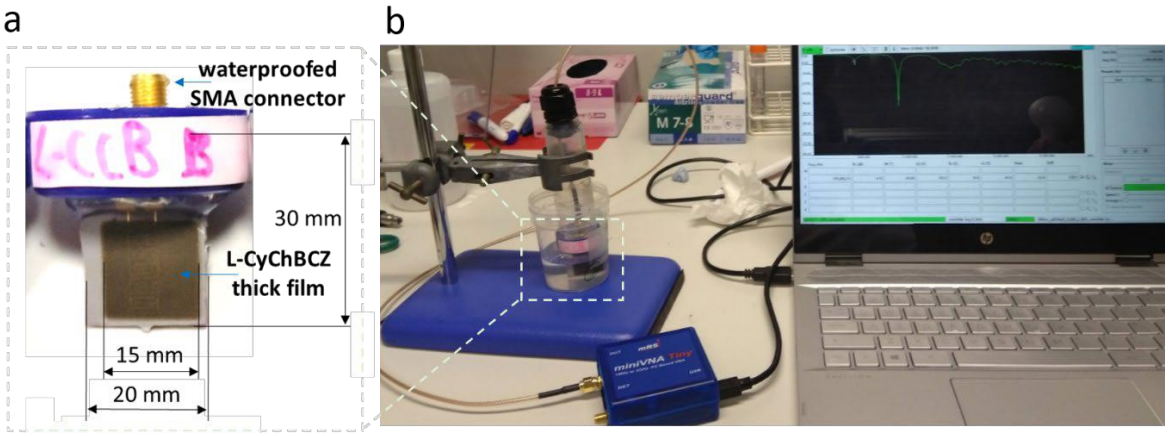

Figure 1 (a) f-EM sensor based on L-CyChBCZ coating and (b) miniVNA tiny connected through coaxial cables to the f-EM sensors immersed in water for monitoring continuously the changes in Cu concentration.

2.4. Lorentz peak function

The spectral responses for the polluted water samples consist of a combination of peaks. For a more accurate identification of a specific metal under test, the full-spectral-response was analysed by fitting the $|S_{11}|$ responses using peak functions. The spectrum was fitted using Lorentz peak function for a more detailed and multiparametric spectrum analysis (equations 1) [9].

$$y = y_0 + \frac{2A}{\pi} \times \frac{w}{4(x - x_c)^2 + w^2} \quad (1)$$

where y_0 is the offset; x_c is the centre of the peak; w is the FWHM (full width at half maximum) and A is the area of the peak.

3. Results and discussion

3.1. S_{11} responses

The microwave response was able to determine the change of Cu content. Six distinct peaks were identified for each sample. Overall, the most significant spectral changes related to the increase of Cu concentration, evaluated by comparing and analysing all the parameters calculated with the Lorentzian fitting-peak, were peaks occurred at 470 and 960 MHz. Figure 2a shows the $|S_{11}|$ response measured with the miniVNA tiny. The two regions are shown in more details in figures 2b and 2c. This experiment demonstrates the feasibility of the microwave response to detect the increase of metal content in water continuously and to quantify its increment.

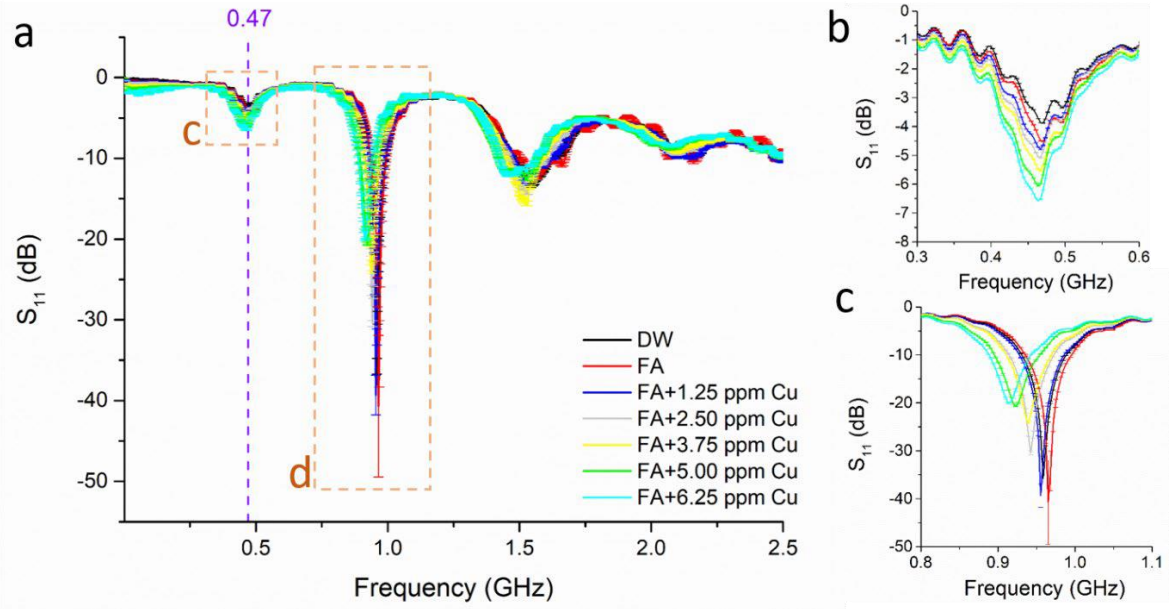

Figure 2 (a) Spectral response for FA series measure with the miniVNA tiny in the frequency range 0.01-2.5 GHz and its magnifications at two resonant peaks: (b) at 0.47 GHz (c) and at 0.91-0.98 GHz.

3.2. VNAs comparison

Table 1 shows a comparison of the sensing performances between the ZVA24 and the miniVNA tiny. This includes the R^2 (linear correlation coefficient), the sensitivity for every 1 mg/L changes of Cu, the quality factor of the peaks (Q-factor) and the limit of detection (LOD) at peaks 1 and 2. The linearity of the sensing, sensor sensitivity and high Q factor are important factors for considering the sensing efficiency, as well as its combination with shifts in resonance frequency.

LOD was evaluated, as described by Salim and Lim [10], using equation 3 which describes the smallest concentration of Cu that can be detected; the Q-factor was found using equation 4.

$$LOD = 3.3 \text{ x } \frac{(SD \text{ of blank response})}{(\text{slope of calibration curve})} \quad (3)$$

$$Q = \frac{f_0}{f_{3dB}} \quad (4)$$

where f_0 is the centre of the peak and f_{3dB} is the half-power bandwidth. All these parameters can be improved by considering multi-resonant peaks in the spectral response of a f-EM sensor.

Table 1 Comparison between VNAs using statistical features

	R^2		Sensitivity[a]		LOD(3)		Q-factor(4)	
	ZVA24	miniVNA	ZVA24	miniVNA	ZVA24	miniVNA	ZVA24	miniVNA
Peak 1	0.981	0.963	0.301	0.399	0.114	0.060	7.39	4.80
Peak 2	0.899	0.900	1.267	3.387	0.967	0.936	135.48	83.98

[a]ΔS_{11} (dB) for each 1 mg/L Cu concentration change;

The results show how the performance of the cheap and portable miniVNA tiny is sufficiently comparable with the ZVA24, demonstrating the feasibility of obtaining accurate in-situ measurements.

4. Conclusion

This paper demonstrates the feasibility of using microwaves and planar sensors for the continuous analysis of Cu ions in water. Planar sensors immersed in water were able to quantify the Cu concentration by the standard addition method. F-EM sensors, functionalised using thick films base on chelating polymers and metal oxides, were used for improving the selectivity of Cu ions in a real complex water sample spiked continuously using the standard addition method.

Lorentzian peak fitting was used for analysing the spectral responses. Non-portable and portable VNAs were used and the performances were found to be comparable, demonstrating the ability for in-situ field measurements.

Acknowledgments

The authors acknowledge the Faculty of Engineering and Technology PhD Scholarship in conjunction with the Faculty of Science programme for allowing this research to be undertaken. Special thanks are given to Dr Olga Korostynska, Patrizia Onnis (PhD student in Faculty of Science) and Prof David Phipps, for their help and valuable suggestions.

References

[1] Environment Agency 2008 *Abandoned mines and the water environment* vol Science project SC030136 (Bristol: Environment Agency)

[2] Agency for Toxic Substances and Disease Registry (ATSDR) 2004 *Toxicological profile for Copper* (Atlanta, GA: Department of Health and Human Services, Public Health Service)

[3] Holmes J, Pathirathna P and Hashemi P 2018 Novel Frontiers in Voltammetric Trace Metal Analysis: Towards Real Time, On-Site, In Situ Measurements *TrAC Trends in Analytical Chemistry*

[4] Tan L, Chen Z, Zhao Y, Wei X, Li Y, Zhang C, Wei X and Hu X 2016 Dual channel sensor for detection and discrimination of heavy metal ions based on colorimetric and fluorescence response of the AuNPs-DNA conjugates *Biosensors and Bioelectronics* **85** 414-21

[5] Rahman N A, Zakaria Z, Rahim R A, Dasril Y and Mohd Bahar A A 2017 Planar Microwave Sensors for Accurate Measurement of Material Characterization: A Review *TELKOMNIKA* **15** 1108-18

[6] Zarifi M H and Daneshmand M 2016 Liquid sensing in aquatic environment using high quality planar microwave resonator *Sensors and Actuators B: Chemical* **225** 517-21

[7] Frau I, Wylie S, Byrne P, Cullen J, Korostynska O and Mason A 2018 Continuous Detection of Copper and Bromide in Polluted Water using f-EM Sensors. In: *2018 12th International Conference on Sensing Technology (ICST)*, pp 35-8

[8] Bader M 1980 A systematic approach to standard addition methods in instrumental analysis *Journal of Chemical Education* **57** 703

[9] Meier R J 2005 On art and science in curve-fitting vibrational spectra *Vibrational Spectroscopy* **39** 266-9

[10] Salim A and Lim S 2018 Review of Recent Metamaterial Microfluidic Sensors *Sensors* **18** 232

ISSN 2398-6611 (Online)

Testing a cosmological galaxy simulation with unsupervised clustering

Sebastian Turner[1,*], Ivan K. Baldry[1], Paulo J. Lisboa[2], Robert A. Crain[1], Steven N. Longmore[1], and Chris A. Collins[1]

[1]Astrophysics Research Institute, Liverpool John Moores University, 146 Brownlow Hill, Liverpool, United Kingdom, L3 5RF
[2]Department of Applied Mathematics, Liverpool John Moores University, Byrom Street, Liverpool, L3 3AF, UK

*s.turner1@2012.ljmu.ac.uk

Abstract. The use of computer simulations enables astrophysicists, who are traditionally limited in their study of the Universe to the use of real observations, to conduct numerical experiments in model Universes to test theories of astrophysics. The results of such numerical experiments must, though, be assessed against real observations in order to establish whether the input theories apply to the real Universe. We present results from a comparison of simulated and observed galaxies via unsupervised clustering. This enables us to compare distributions of galaxies in many features at the same time, with a view to breaking the overall populations down into subpopulations. Simulated galaxies are taken from the EAGLE suite of hydrodynamical simulations, which model the formation and evolution of cosmologically representative populations of galaxies, while observed galaxies are taken from the GAMA survey. We take care to establish a consistent samples and feature selections between simulations and observations.

Keywords. galaxies: general - galaxies: statistics - galaxies: evolution - galaxies: formation - methods: statistical

1. Introduction

Understanding the diversity of galaxies in the Universe is an open question in astrophysics. In particular, establishing the origins of the various observed bimodalities of galaxies in e.g. morphology (Schawinski et al., 2014), star formation (Smethurst et al., 2015), and environmental status (Wang et al., 2018) will be key to disentangling the interplay of evolutionary mechanisms that influence them. Simulations are a valuable resource in this pursuit. They supplement the observational study of the Universe by enabling numerical experimentation with theories of astrophysics in model Universes.

Unsupervised clustering presents an opportunity to examine simulations and observations together in a new way. While previous such projects have studied one feature at a time (e.g. Furlong et al., 2015), unsupervised clustering invites the use of several more features simultaneously for a full exploration of the available data. There are several previous studies that have used unsupervised clustering in an astrophysical context (e.g. Siudek et al., 2018). This study represents the first time that it has been applied for a comparison of observed and simulated galaxy subpopulations.

Our clustering approach was introduced in section 2 of Turner et al. (2019). We briefly summarise it again here for ease of reference. We apply the `k-means` unsupervised clustering algorithm for its conceptual simplicity and computation speed. `k-means` aims to partition a sample of N observations in a D-dimensional feature space into k compact, spherical clusters. The number of clusters k is not known in advance, so we trial several values. We also use random initialisations to ensure that `k-means` fully explores the feature space, but this means that `k-means` may return different outcomes. Our approach evaluates `k-means` clustering outcomes in terms of how well they model the observations. By measuring the stability of outcomes, we are able to identify the best value of k; that which most consistently returns similar outcomes. Then, by measuring the compactnesses of outcomes at that value of k, we are able to identify the very best clustering outcome overall.

In this paper we report a comparison of observed and simulated samples galaxies via this unsupervised clustering approach. The remainder of this paper is structured as follows. In section 2, the focus of this paper, we outline our samples, feature selection, and data preparation, particularly with a view to the care taken to ensure a fair comparison. In section 3, we present some early results of our unsupervised clustering, discuss some of their implications, and suggest future directions for this work.

2. Data

We construct our samples as consistently as possible. They are characterised with the same five features: stellar mass, dust mass, specific star formation rate, a measure of size, and bulge-to-total ratio. Sections 2.1 and 2.2 outline the construction of each of these samples. The final samples are shown as black scatter points in figure 1, and are broadly consistent. Simulated galaxies appear smaller and bulgier. The observed sample ends up with 3669 galaxies and the simulated sample with 7129.

2.1 GAMA

Our observational sample of galaxies comes from the third data release (DR3; `http://www.gama-survey.org/`) of the Galaxy And Mass Assembly (GAMA) survey (Baldry et al., 2018). The survey aims to evaluate cold dark matter (CDM) models of the Universe using observations of baryonic structure at scales of 1 kpc to 1 Mpc. The survey is structured around its spectroscopic campaign, which provided reliable heliocentric redshifts for ~300000 objects to an apparent r-band magnitude limit of 19.8 across five regions of the sky covering a total area of 286 deg^2. The spectroscopy in the three equatorial regions has been supplemented with reprocessed imaging in 21 bands from a variety of other surveys that overlap with the GAMA survey spectroscopic campaign footprint (the Panchromatic Data Release; Driver et al., 2016).

We gather feature data for our GAMA survey sample from two DR3 data tables: `MAGPHYSv06` and `BDDecompv02`. `MAGPHYSv06` contains outputs from the application of the energy balance code `MAGPHYS` to the self-consistent extinction-corrected matched aperture photometry listed in the data table `LAMBDARCatv01` (Driver et al., 2018). `LAMBDARCatv01` was generated by the application of the photometric code `LAMBDAR` (Wright et al., 2016) to the reprocessed imaging collated for the Panchromatic Data Release. `MAGPHYS` uses template spectra that model the emission of optical light by stars (Bruzual et al. 200) and far infra-red light by dust (i.e. attenuated and then reemitted; Charlot et al., 2000) in a given galaxy to estimate its energy output based on fits of these spectra to input photometry. From `MAGPHYSv06`, we take the median stellar masses (M_*), dust masses (M_d), and Gigayear-timescale specific star formation rates ($SSFR$) given by the probability density functions of fits to the `LAMBDARCatv01` photometry. The dust masses are converted to specific dust masses by dividing by the stellar masses in order to eliminate any linear dependence on stellar mass.

`BDDecompv02` lists outputs from the application of `ProFit` and `ProFound` (Robotham et al., 2017; 2018) to Kilo-Degree Survey (De Jong et al., 2017) r-band imaging of $z < 0.08$ galaxies in the three equatorial regions of the GAMA survey. `ProFit` uses Bayesian statistics to model the light profiles of galaxies, while `ProFound` conducts source extraction on images. From `BDDecompv02`, we take effective radii derived from single-Sérsic fits ($R_{e,l}$), and bulge-to-total light ratios (B/T_l) derived from two-component fits consisting of a Sérsic bulge and an exponential disc.

We apply the following limits to each of the features representing our observed sample of galaxies. The lower limit for MM_* is imposed to match the EAGLE MM_* limit (see section 2.2). All other limits are imposed to exclude outliers from the sample.

$$9.5 < \log_{10}(M_*) < 12.0, \mathrm{M}_\odot$$
$$-6.0 < \log_{10}(M_d) < -2.0, \mathrm{M}_\odot$$
$$-14.0 < \log_{10}(SSFR) < -9.0, \mathrm{yr}^{-1}$$
$$0.0 < \log_{10}(R_{e,l}) < 1.5, \mathrm{kpc}$$
$$0.0 < B/T_l < 1.0$$

2.2 EAGLE

The Evolution and Assembly of GaLaxies and their Environments (EAGLE) simulations (Schaye et al., 2015; Crain et al., 2015) are hydrodynamical, cosmological models of the formation and evolution of galaxies in a flat Λ-CDM Universe. The simulations feature subgrid prescriptions which model the effects of astrophysical processes that operate below the resolution limits of the simulations. Schaye et al. (2015) describe these subgrid prescriptions in full in section 4 of their paper. Their specific details, and the resolution below which they were implemented, varied among the EAGLE simulations.

We construct our simulated sample of galaxies using the outputs of the `RefL0100N1504` simulation. This was one of several fiducial EAGLE simulations (denoted by the prefix "`Ref`") which were run in various volumes using the same subgrid prescriptions and at a standard resolution. `RefL0100N1504` proceeded in a 100^3 comoving Mpc^3 volume, the largest volume modelled by the EAGLE simulations, which therefore contains the full diversity of galaxies of the EAGLE simulations. It contained 1504^3 dark matter particles, each with mass 9.70×10^6 M$_\odot$, and initialised with the same number of baryonic particles, each with initial mass 1.81×10^6 M$_\odot$.

We gather feature data for our EAGLE sample from several data tables (`http://virgodb.dur.ac.uk:8080/Eagle/`). Stellar masses (M_*) are taken from `Aperture`. We opt for stellar masses within the central 30 pkpc of galaxies as they exhibit the best agreement with observations (Schaye et al., 2015), including the GAMA survey (Baldry et al., 2012). Projected half-mass radii ($R_{1/2,m}$), also calculated using the stellar mass within the central 30 pkpc, are taken from `Sizes`. Dust masses (M_d), derived from restframe submillimetre fluxes calculated with the radiative transfer code `SKIRT`, come from `DustFit` (Camps et al., 2018). Again, we divide the dust masses by the stellar masses for specific dust masses. Bulge-to-total mass ratios (B/T_m) are listed in `MorphoKinem` (Thob et al., 2019). They are defined kinematically by doubling the mass of counter-rotating stars in a given galaxy under the assumption that the bulge does not exhibit any net rotation. Finally, specific star formation rates ($SSFR$) are obtained from `Stars` by summing the masses of all star particles formed within the central 30 pkpc a given galaxy within the last 10^9 years, dividing those masses by 10^9 years (for rates), and then dividing those star formation rates by the aforementioned stellar masses of the galaxies.

We apply the limits shown below to our simulated sample of galaxies. The lower M_* limit is imposed as, below this mass, galaxies from the EAGLE simulation are less reliably comparable with observed galaxies (Schaye et al., 2015; Thob et al., 2019). We note that the EAGLE simulations report zero $SSFR$s and M_d for some galaxies; equivalent observed galaxies would have non-zero, noise dominated values for these features. In order to enable a comparison of these sorts of galaxies (i.e. with low SSFR and Md), we calculate new values for these features for simulated galaxies with $\log_{10}(SSFR) < -11$ and $\log_{10}(M_d) < -4$ with random values, drawn from a normal distribution centred at these values and having standard deviation equal to the typical observational uncertainty on these features, as taken from our observed sample. All other limits below are imposed to exclude outliers.

$$9.5 < \log_{10}(M_*) < 12.0, \mathrm{M}_\odot$$
$$-6.0 < \log_{10}(M_d) < -2.0, \mathrm{M}_\odot$$
$$-14.0 < \log_{10}(SSFR) < -9.0, \mathrm{yr}^{-1}$$
$$0.0 < \log_{10}(R_{1/2,m}) < 1.0, \mathrm{kpc}$$

1. Results

We cluster in both samples from $kk = 2$ to 20. Feature data is z-scored prior to clustering in order to eliminate any clustering bias towards any feature with larger numerical ranges. We initialise 100 times at each value of kk. Applying our cluster evaluation approach, as outlined in section 1, we find stable clustering up to $kk = 5$ in our observed sample, and $kk = 6$ in our simulated sample. We select the most compact outcomes at these highest stable values of kk for further study, as they will offer us the most insight into the subpopulations in each sample. These outcomes are visible in figure 1.

The outcomes show broad agreement with one another, particularly at lower masses. Equivalent clusters (suggested by the use of the same colour in each of the plots in figure 1) occupy similar regions of the sample distributions in the five-dimensional feature spaces. This is in spite of some differences in the overall scaling relations. Clusters in the observed sample appear broader due to effects like noise and measurement uncertainty. Agreement worsens at higher masses, where there are three simulated clusters vs. two observed clusters. The EAGLE simulations use feedback to regulate and inhibit star formation activity, particularly at higher masses, so the subgrid prescriptions that implement this may be responsible for these differences in clustering structures. We intend to use a metric like the Kullback-Leibler Divergence to quantitatively measure the similarity of the distributions of each of these sets of clusters. This will enable us to establish the relative important of features in the clustering, and hence identify the simulation theories that have succeeded and failed with respect to reproducing the observed cluster distribution. For those clusters that are successfully reproduced in the simulated sample, we intend to trace the galaxies in those clusters back through time to understand how they evolved, and thereby make inferences about the galaxies contained within their equivalent observed clusters.

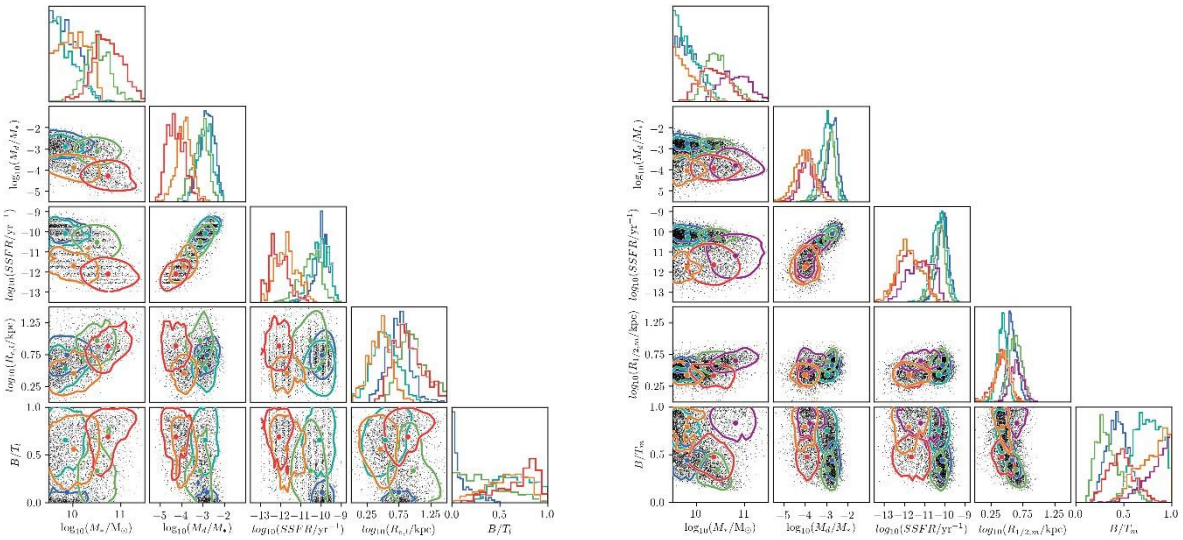

Figure 1. k-means clustering in our observed (left) and simulated (right) samples of galaxies. In both plots, the black scatter points show the sample, and the coloured contours and histograms show the cluster distributions. Colours have been chosen and applied to suggest equivalencies between the clusters in each sample.

2. References

Baldry I. K., et al., 2012. *MNRAS*, 421, 621
Baldry I. K., et al., 2018. *MNRAS*, 474, 3875
Bruzual G. and Charlot S., 2003. *MNRAS*, 344, 1000
Camps P., et al., 2018. *ApJ Supplement Series*, 234, 20
Charlot S. and Fall S. M., 2000. *ApJ*, 539, 718
Crain R. A., et al., 2015. *MNRAS*, 450, 1937
De Jong J. T. A., et al., 2017. *A&A*, 604, A134
Driver S. P., et al., 2016. *MNRAS*, 455, 3911
Driver S. P., et al., 2018. *MNRAS*, 475, 2891
Furlong, M., et al., 2015. *MNRAS*, 450, 4486
Lisboa P. J., et al., 2013. *BMC Bioinformatics*, 14, S8
Robotham A. S. G., et al., 2017. *MNRAS*, 466, 1513
Robotham, A. S. G., et al., 2018. *MNRAS*, 476, 3137
Schawinski, K., et al., 2014. *MNRAS*, 440, 889
Schaye J., et al., 2015. *MNRAS*, 446, 521
Siudek, M., et al., 2018. *A&A*, 617 70
Smethurst, R. J., et al., 2015. *MNRAS*, 450, 435
Thob A. C. R., et al., 2019. *MNRAS*, 485, 972
Turner S., et al., 2019. *MNRAS*, 482, 126
Wang, E., et al., 2018. *ApJ*, 860, 102
Wright A. H., et al., 2016. *MNRAS*, 460, 765

ISSN 2398-6611 (Online)

Participant Influences on the Success of Critical Path Method Planning in Construction Project Environments

Neil Pickavance, Andrew Ross and Damian Fearon
Department of the Built Environment, Faculty of Engineering & Technology, Liverpool John Moores University, Byrom Street, Liverpool, L3 3AF
n.m.pickavance@2017.ljmu.ac.uk
a.d.ross@ljmu.ac.uk
d.j.fearon@ljmu.ac.uk

Abstract. Critical Path Method (CPM) planning as a logic-based and deterministic programming method operates in construction contracting environments characterised by excessive trade sub-letting, work package fragmentation, transient low-loyalty sub-contract labour, poor trade integration, and dislocated project teams. Despite some advances, newer methods adhering to a social-based collaborative approach, such as Lean Construction and Last Planner® System, have not yet positioned themselves as primary use methods of planning and project control. A reconsideration of CPM literature across construction programme management has been undertaken and several approaches to CPM planning are identified. However, there appears to be an absence of work on its practical application within construction contracting environments. Exploratory qualitative data was collected through a purposive sample of six semi-structured interviews with UK construction management personnel on a case-study project. Results were used to identify emerging key themes and guide back into the literature. CPM planning seems to operate in unstructured environments characterised by poor application, understanding, and ad hoc engagement by participants. It is concluded that problems with CPM may be rooted in people-based, and not process-based, issues.

Keywords. Critical Path Method, Last Planner® System, programme, subcontractor, integration

1. Introduction

This paper is part of an ongoing research project to investigate and understand the influences that project participants exert on the adoption and application of traditional Critical Path Method (CPM) planning at contracting organisations in the UK construction industry. CPM remains the most commonly used project planning technique in UK construction, possibly due to being a standardised method, familiarity, and being specified widely by construction clients. UK construction dispute resolution uses CPM extensively to demonstrate time entitlements. Despite this widespread use CPM is criticised as a construction planning tool (Tommelein et al, 1999), particularly from proponents of Lean Construction, Last Planner® System, and other similar social-based methodologies.

On the whole, complex construction projects in the UK are likely to be finished more than six months late (CIOB, 2008). From practical observations within construction project environments there appears considerable evidence that main and sub-contracting teams are failing to adopt and apply CPM in a structured manner. Further, reviews of literature on and around construction planning returned limited evidence of the understanding, adoption, and application of CPM within complex project environments. These environments, characterised by excessive sub-letting, work package fragmentation, transient low-loyalty sub-contract labour, and poor trade integration create dislocated relationships between teams within projects that are not well-suited to traditional CPM planning.

This paper further progresses a preceding critical investigation into the adoption and application of CPM within a construction project case-study environment. The categories and emerging concepts from the results of six qualitative semi-structured interviews with experienced personnel form a basis to guide back into the literature around construction management, supply chain integration and management, collaboration, partnering, and organisational cultures. This focuses the investigation on the wider context of project teams and an understanding of their impacts on the success of CPM planning within construction environments, and not just the system limitations.

2. Literature Review

Project planning, management, and control of construction projects has traditionally been undertaken via network analysis. Originating from industrial, military, and production environments the transposition of CPM into construction was recorded in "A non-computer approach to the critical path method for construction" (Fondahl, 1962). With similarities to Program Management and Review Technique (PERT), CPM is based on mathematical and algorithmic models of logic networks applied to construction scheduling (Aquilano & Smith, 1980). Activities, milestones, and critical trades are mapped within a logical network, with programme management via this deterministic approach remaining a significant method of planning and project control (Agyei, 2015).

Many subjects are successfully conveyed, and learned, from textbook format but characteristics and nuances of construction project planning is difficult to convey. Operating within a diverse, fragmented, multi-cultured temporary organisation delivering a complex, bespoke product with a transient, low-loyalty, sub-contracted workforce the creation, management, and execution of project planning goes beyond network diagrams and resource schedules. Application of CPM in contracting environments is not addressed in construction texts (Lester, 2006) and (Pierce, 2013).

UK government has commissioned numerous construction industry reports with the intention of providing best-practice strategies on key issues. Many focus on project delivery improvements such as partnering and collaborative working (Latham, 1994), performance and efficiency (Egan, 1998), reports to check and measure the success of previous reports (Wolstenholme, 2009), and production improvements (Construction 2025, 2013). Addressing high-level industry issues most reports do not consider the serious impact supply chain fragmentation has on projects.

Official codes of practice provide operating frameworks for project management and delivery. However, these appear to lean towards being largely administrative (British Standards Institution, 2010). The Project Management Body of Knowledge (Association of Project Management, 2012) similarly fails to address the complex nature of planning in fragmented contracting environments. The Code of Practice for Programme Management in the Built Environment (Chartered Institute of Building, 2016) also fails to adequately address real-world planning challenges.

Responsibility for undertaking the project planning role at main contractors varies within the UK construction industry, from a dedicated planning position or by another project management team member. Depending on project size, company culture, and culture within a building sector there may be no formal responsibility for the project planning role. Poorly allocated and unsupported planning staff appears to foment a questioning of integrity of the planner role, coupled with limitations of formal deterministic planning (CPM) becoming more widely recognised (Winch & Kelsey, 2005). Similar querying on whether construction project planning was doing its job (Laufer & Tucker, 1987) demonstrates some misunderstanding of the fundamental nature of the execution of the planning role.

Alternative planning methodologies (imported from automotive and production industries) from the 1990s onwards suggest alternatives to CPM's hard-logic 'push planning' approach. Categorised as Collaborative Planning these comprise modern methods such as Lean Construction (Koskela, 1992) and Last Planner® System (Ballard, 2000). Similar variants are Agile Project Management, AgiLean Project Management, Six Sigma, and Lean Six Sigma. While characterised by improvement process,

reduction of ‘waste’, and collaborative working via work-crew inclusivity there is little evidence that these approaches significantly address the root of supply chain fragmentation.

3. Method

The research design builds upon a qualitative case-study to collect and interpret data to discover concepts and relationships within a live construction project environment. The collation of the original data was by interviews, with the research position interpretivist in nature. This qualitative strategy emphasised social reality research over quantification of data (Bryman, 2016). The case study was undertaken at a new-build construction development in the UK Midlands area that had entered into its contract phase. The final account is projected to be circa £300.0M and the main contractor is a large construction organisation who operate predominantly on the UK mainland but also continental Europe. In addition, two sub-contract companies engaged on the same project were included in the study. Both sub-contract organisations were major UK supply chain contractors, one operating in the steel frame erection sector and the other operating in the mechanical and electrical building services sector.

Interviewees were selected as a cross-section sample of construction management personnel within the case-study organisations. Four construction staff from the main contractor, and one member of staff each from the sub-contractors were interviewed. Each participant was employed full-time in either a project manager role or project planner role and possessed between fifteen and thirty two years’ experience in the UK construction industry. The mean years of experience of the sample was 26.2.

The original eleven questions posed in the interviews were open and exploratory, designed to elicit rich data for further analysis. The questions spanned common topics in project planning and were developed from extensive observations and experience within a practitioner environment. The interviews used a semi-structured approach on a personal face-to-face basis with key topics derived from the literature. To focus the investigation the approach within this paper has been to utilise the questions (and responses) from six of the original eleven questions posed that concentrated on CPM challenges, supply chain integration, and co-ordination. The six questions were:

> Q1. What do you perceive are the main challenges for contractors planning with Critical Path Method?
>
> Q2. How much do attitudes and cultures within a company influence the successful development and co-ordination of an integrated construction programme?
>
> Q4. How do you feel the programme development and co-ordination process could be improved?
>
> Q5. What are the methods, techniques and protocols that construction organisations use to develop, co-ordinate and integrate critical path programmes?
>
> Q7. What processes do you follow to establish and integrate the various sub-contract trade sections of the construction programme?
>
> Q11. How do you feel a process similar to the RIBA’s Plan of Work would be of use for developing a co-ordinated and integrated programme?

The data from the six interviews has been previously transcribed into written text and an open-coding analytical process undertaken. NVivo 11 qualitative data analysis computer software package was used to code the transcripts at the sentence level to identify categories and concepts. This analysis was to provide an initial exploratory investigation into the subject matter. Open-coding allowed the text to be opened up and expose the thoughts, ideas, and meanings contained therein, to uncover, name, and develop concepts (Strauss and Corbin, 1990).

This paper has built upon the initial investigation by utilising the categories and emerging key themes from the qualitative data analysis to guide back into the literature. This direction is intended to support the development of a conceptual framework for further positioning the research in the wider context of the subject areas via existing theories, methods, methodologies, and practice.

4. Results / Discussion

Some challenges around the usage of traditional CPM planning appear not that it is a deterministic / logic-based method (as often) criticised by Collaborative Planning proponents, but fundamentally whether project participants have a basic understanding of CPM application and its benefits. Interviewee 3 (Contracts Manager): "*I think that the identification of the activities which are critical to the successful completion, that's the main challenge…*"

Prevalent cultures at contracting organisations appear to directly impact and influence the adoption and application of CPM planning. Within a general construction contracting environment the participants seemed aware that they were maybe 'stuck' in the past. Interviewee 1 (Senior Planner): "*Different industries have different cultures…the petrochemical industry and the nuclear industry have got better cultures than the normal construction - as I call it - industry. I think they're a bit behind the times, normal construction, they don't like moving forward…*"

Early and consistent supply chain engagement and partnering was seen as crucial to CPM programme development and co-ordination, acknowledging the importance of trade programme contribution into the master programme. Interviewee 1 (Senior Planner): "*I think you should have a specialist set of contractors who do the tender, and they all know each other, get together, do the integrated programme together and that's what you run with.*"

Formal protocols for CPM programme development seem poorly evident, and ad hoc approaches may be common. The informal 'weighing-up' of a project with the supply chain, alongside formal planning techniques, was stated. Interviewee 2 (Senior Project Manager): "*Yes, the supply of information, walking the course, making sure they understand the project itself, the logistical strategy on the project, what's going on around the project in the area*."

In a predominantly sub-contracting environment the approaches to trade programme integration had a major influence on quality and success of programme. Interviewee 2 (Senior Project Manager): "*We go through various workshops, we bring them together, we do analysis of the programmes at each iteration, we understand it, we get the buy-in from our teams, our supply chain.*" Significantly, the aforementioned events are not a formal protocol.

While a formal process framework (RIBA) exists for design development progression in the construction industry there is a notable lack of similar for programme development. Interviewee 1 (Senior Planner): "*I think there is a definite need for a structure for developing programmes, especially integrating the subcontractor programmes and how that links in to the main programmes.*" Lack of stage-gates in CPM programme development is evident here.

5. Conclusion

This study has undertaken a small number of interviews on a major UK construction project with full-time professional, experienced, and senior contracting personnel. The primary data collected rich, descriptive experiences from pre-arranged semi-structured interviews. From this data the use of CPM planning seemed to operate in an unstructured environment characterised by poor understanding and application of CPM and dislocated engagement by project participants into the programme management function. The results from this study may be fairly representative of contracting organisations in the UK due to the general nature of the project studied.

Emerging literature is directing further investigation into various themes such as training and development of project teams, communication, construction supply chain management, contractor partnering, organisational cultures, collaborative practices, and supply chain integration. The challenges with CPM planning relating to the logical and deterministic nature of CPM planning seem to be of only partial concern to the sample. Key inferences are that challenges with CPM planning may be rooted in behavioural and cultural issues over process-based issues.

A relatively small, albeit very experienced, research sample was used for the study. However, the paper has addressed a need evident from the literature search that the effects of behaviours, attitudes, and cultures within contracting organisations on the success of CPM planning doesn't appear to be widely researched. Further investigation is necessary to be undertaken at UK contracting organisations to identify the adoption and application of CPM planning, with the aim of ascertaining the efficiencies of both the system itself and the operators of CPM.

6. References

[1) Agyei, W. (2015). Project planning and scheduling using PERT and CPM techniques with linear programming: case study. *International Journal of Scientific & Technology Research*, *4*(8), 222-227.
[2] Association for Project Management. (2012). *APM body of knowledge*. Buckinghamshire, England: Association for Project Management.
[3] Aquilano, N. J., & Smith, D. E. (1980). A formal set of algorithms for project scheduling with critical path scheduling/material requirements planning. *Journal of Operations Management*, *1*(2), 57-67.
[4] Ballard, H. G. (2000). *The last planner system of production control* (Doctoral dissertation, University of Birmingham).
[5] British Standards Institution (2010) *BS6079-1:2010: Project management. Principles and guidelines for the management of projects*. Available at: https://www.shop.bsigroup.com/ (Accessed: 20 April 2018).
[6] Bryman, A. (2016). *Social research methods*. Oxford university press.
[7] Chartered Institute of Building (CIOB), 2008. A Research on Managing the Risk of Delayed Completion in the 21st Century, CIOB, Ascot.
[8] CIOB. (2016). Code of Practice for Programme Management in the Built Environment. Chichester: Wiley Blackwell.
[9] Egan, J. (1998). Rethinking construction: report of the construction task force on the scope for improving the quality and efficiency of UK construction. *Department of the Environment, Transport and the Regions, London*.
[10] Fondahl, J. W. (1962). A non-computer approach to the critical path method for the construction industry.
[11] HM Government. (2013). Construction 2025. Industrial Strategy: Government and Industry in Partnership.
[12] Koskela, L. (1992). *Application of the new production philosophy to construction* (Vol. 72). Stanford: Stanford University.
[13] Latham, M. (1994). Constructing the team: Joint review of procurement and contractual arrangements in the UK construction industry. *Department of the Environment, UK*.
[14] Laufer, A., & Tucker, R. L. (1987). Is construction project planning really doing its job? A critical examination of focus, role and process. *Construction Management and Economics*, *5*(3), 243-266.
[15] Lester, A. (2006). *Project management, planning and control: managing engineering, construction and manufacturing projects to PMI, APM and BSI standards*. Elsevier.
[16] Pierce Jr, D. R. (2013). *Project scheduling and management for construction* (Vol. 89). John Wiley & Sons.
[17] RIBA. (2013). RIBA plan of work 2013. *RIBA*.
[18] Strauss, A., & Corbin, J. M. (1990). *Basics of qualitative research: Grounded theory procedures and techniques*. Sage Publications, Inc.

[19] Tommelein, I. D., Riley, D. R., & Howell, G. A. (1999). Parade game: Impact of work flow variability on trade performance. *Journal of construction engineering and management*, *125*(5), 304-310.
[20] Winch, G. M., & Kelsey, J. (2005). What do construction project planners do?. *International Journal of Project Management*, *23*(2), 141-149.
[21] Wolstenholme, A., Austin, S. A., Bairstow, M., Blumenthal, A., Lorimer, J., McGuckin, S., ... & Guthrie, W. (2009). Never waste a good crisis: a review of progress since Rethinking Construction and thoughts for our future.

ISSN 2398-6611 (Online)

A fuzzy evidential reasoning approach to improve prior probabilities evaluation process for parent nodes of Bayesian Network (BN) model used for two-stroke engine health assessment

Muhammad Usman*, Zaili Yang
Liverpool Logistics Offshore and Marine Research Institute, James Parson Building, Byrom Street.
*E-mail address: M.Usman@2014.ljmu.ac.uk

Abstract: Maintenance of machinery equipment is part of necessary costs of a ship operation. With the evolution of technology, innovative models are being employed to move away from fixed interval maintenance actions towards predictive maintenance to extend the time between overhauls. A Bayesian network (BN) model has been developed as health assessment tool for a large two-stroke engine. However, there was a gap in the model where prior probabilities for BN parent nodes were estimated from engine operational parameters directly through user's knowledge and experience. A fuzzy model was developed to address this issue by standardising the process, however fuzzy min-max operation was unable to respond to the variances in antecedent and reflect the proportional change in consequents. To improve the sensitivity of the model, a fuzzy evidential reasoning (ER) model has been proposed in this work. There have been multiple inputs for each parent node of the BN model hence effectiveness of the proposed approach has been demonstrated by creating a fuzzy ER model for scavenge air quality node. Operational inputs from engine operational data can be inserted into the fuzzy ER model and then the obtained output coupled with the BN would calculate the overall health of the engine. The advantage of this user-friendly model is that it can run simulations for trending various operational parameters.

Keywords: Evidential Reasoning (ER), Bayesian Network (BN), Two-stroke engine

Introduction:

With the ever-increasing commercial pressures on ship operators and shrinking margins, loss of propulsion due to machinery breakdown is just a tip of the iceberg and exhibits a significant economic loss associated with the subsequent delays and repair bills. In its 2018 annual report, the Swedish Club (2018) reported that the cost of machinery claims for the period 2015-2017 was around USD 384 million with main engine damages remain the most expensive category accounting for 34% of the total machinery claims. Efforts are underway from engine manufacturers and operators to enhance reliability of engine operations through better diagnostic and prognostics.

This paper advances the work presented by Usman et al., (2018) where prior probabilities for Bayesian Network (BN) of two-stroke engine diagnostic model were developed through a fuzzy set theory. However, the main criticism of the proposed method has been the traditional fuzzy 'min-max' approach used to quantitatively determine the consequent part of the fuzzy rule base. There can be several ways to address the issues though Evidential Reasoning (ER) seem to have the superiority as it avoids the loss of useful information during inference process. Moreover, slight changes in the antecedent part of the rule base may sometimes be inadequately reflected in the consequent part with the conventional fuzzy methodology (Yang et al., 2009).

Evidential Reasoning (ER)

The ER approach was initially used to address the quantitative and qualitative issues concerning multi-criteria decision making (MCDM) under uncertainty by utilising the expert judgement in the form of belief functions (Yang & Xu, 2002). Since then there has been number of applications such as Zeng et al., (2006) carried out an information technology project by developing an aggregative risk assessment; Liu et al., (2003) used the fuzzy rule base ER approach to analyse the safety of an engineering system.

ER algorithm

ER algorithm is used to capture the non-linear relationships between the set of rules. This aim is achieved by combining all the outputs from each rule to generate a conclusion. For this study,

following steps have been adopted to improve the fuzzy inference through the use of ER approach.

The first step is the assigning the relative weight (ω) to the antecedents A_k (where K = 1, 2, …, L) and mainly under the condition of $\sum_{KK=1}^{LL} \omega = 1$. Assigning of the weights are performed through expert judgement as it is understood that impact of the various parameters on overall performance or outcome is unequal in real world scenarios hence this needs to be reflected in the model.

The second step is the calculating the degree of belief (β_k) based on knowledge of antecedents (A_k) for consequents (D_k). This is mainly carried out by taking into the relative weights assigned to the antecedents in the step one. For example, IF 'air pressure' is **Low,** 'temperature' is **Low,** 'water mist catcher (WMC)' performance is **Satisfactory,** THEN 'scavenge quality' is 25% **Satisfactory** and 75% **Unsatisfactory.**

Third step is calculating the weight of each rule Θ_k for a particular scenario. This is performed by multiplying the corresponding antecedent mass distribution to generate a crisp number for the rule R_k. The impact of the particular rule in the final outcome is proportional to its weight though following condition applies $\sum_{KK=1}^{NN} \Theta = 1$ (for total rules activated for a particular scenario).

The fourth step comprised of calculating the mass distribution of D_k for each rule. This is the product of weight of each rule and degree of belief as per equation below.

$$\{D_k\} : m_k^1 = \beta_k^1 \times \Theta_k^1 \text{ for } (k = 1, 2, .., L)$$

Final step is aggregating the values consequents to give final outcome for the ER fuzzy inference process. For a consequent D_k^1

$$\{D_k^1\} : \sum_{k=1}^{L} m \ (k = 1, 2, \ldots, L)$$

In certain scenarios there can be incompleteness or unassigned degree of belief in the assessment which if represented as H_U can be calculated through $H_U = \frac{\widetilde{H_{UI}}}{1-\widetilde{H_{UI}}}$.

Likewise the evaluation of several reviewers or the assessment of the condition of subordinate criteria can be combined in chain systems (components or sub-components) (Asuquo et al., 2019).

ER application

As described earlier, this paper intends to provide technical improvements in the work (Usman et al., 2018) performed on demonstrating the fuzzy logic application to determine the scavenge air quality hence taking the same operational example and values used for fuzzy model input in the previous paper;

Table 1 : Input operational variables

	Units	Operational input
Effective Power	BHP	6300
Corresponding Scavenge air pressure as per manual	Bar	1.7
Actual Scavenge air pressure	Bar	1.4
Scavenge air temperature	^oC	40
Condensate water collected (actual)	Tons/24H	16
Condensate water (calculated from operations manual for given conditions)	Tons/24H	18

Placing these operational values into the fuzzy model would result in the following table which shows the fuzzy membership for all three variables.

Table 2: Fuzzy membership for individual fuzzy sets

Air pressure	
Low	0.26
Acceptable	0.74
Temperature	
Low	0.2
Acceptable	0.8
High	0
Water mist Catcher	
Satisfactory	0.6
Unsatisfactory	0.4

This scenario has activated following 8 rules out of total 12 as per the following table;

Table 3: Activated rules

		Air Pressure	Temperature	WMC
Rule A	If --->	Low (-ive)	Low (-ive)	Satisfactory (+ive)
Rule B	If --->	Low (-ive)	Low (-ive)	Unsatisfactory (-ive)
Rule D	If --->	Low (-ive)	Acceptable (+ive)	Satisfactory (+ive)
Rule E	If --->	Low (-ive)	Acceptable (+ive)	Unsatisfactory (-ive)
Rule G	If --->	Low (-ive)	High (-ive)	Satisfactory (+ive)
Rule H	If --->	Low (-ive)	High (-ive)	Unsatisfactory (-ive)
Rule J	If --->	Acceptable (+ive)	Low (-ive)	Satisfactory (+ive)
Rule K	If --->	Acceptable (+ive)	Low (-ive)	Unsatisfactory (-ive)
Rule M	If --->	Acceptable (+ive)	Acceptable (+ive)	Satisfactory (+ive)
Rule N	If --->	Acceptable (+ive)	Acceptable (+ive)	Unsatisfactory (-ive)
Rule P	If --->	Acceptable (+ive)	High (-ive)	Satisfactory (+ive)
Rule Q	If --->	Acceptable (+ive)	High (-ive)	Unsatisfactory (-ive)

As a first ER step, three operational indicators i.e. Scavenge air pressure, temperature and water mist catcher performance has been assigned individual weights based on their importance to impact the outcome i.e. 'scavenge air quality' as per following table through expert judgement;

Table 4: weight of antecedents

Scavenge Air	Pressure	temperature	WMC performance
ω	0.40	0.35	0.25

Second step is determining the degree of belief of each rule as demonstrated below;

Table 5: degree of belief

ω --->	0.4	0.35	0.25	Then (Scavnge Quality)	
	Air Pressure	Temperature	WMC	Satisfactory	Unsatisfactory
If --->	Low (-ive)	Low (-ive)	Satisfactory (+ive)	0.25	0.75
If --->	Low (-ive)	Low (-ive)	Unsatisfactory (-ive)	0	1
If --->	Low (-ive)	Acceptable (+ive)	Satisfactory (+ive)	0.6	0.4
If --->	Low (-ive)	Acceptable (+ive)	Unsatisfactory (-ive)	0.35	0.65
If --->	Low (-ive)	High (-ive)	Satisfactory (+ive)	0.25	0.75
If --->	Low (-ive)	High (-ive)	Unsatisfactory (-ive)	0	1
If --->	Acceptable (+ive)	Low (-ive)	Satisfactory (+ive)	0.65	0.35
If --->	Acceptable (+ive)	Low (-ive)	Unsatisfactory (-ive)	0.4	0.6
If --->	Acceptable (+ive)	Acceptable (+ive)	Satisfactory (+ive)	1	0
If --->	Acceptable (+ive)	Acceptable (+ive)	Unsatisfactory (-ive)	0.75	0.25
If --->	Acceptable (+ive)	High (-ive)	Satisfactory (+ive)	0.65	0.35
If --->	Acceptable (+ive)	High (-ive)	Unsatisfactory (-ive)	0.4	0.6

The next phase is the determining the weight of activated rules. From table 3, it can be observed that there are 8 rules activated for the given scenario. Hence their corresponding weights are calculated as shown in the following table;

Table 6: weights of activated rules

Activated rule tag	Corresponding antecedent values			Θ (weight of each rule
A	0.26	0.20	0.60	0.031
B	0.26	0.20	0.40	0.021
D	0.26	0.80	0.60	0.125
E	0.26	0.80	0.40	0.083
J	0.74	0.20	0.60	0.089
K	0.74	0.20	0.40	0.059
M	0.74	0.80	0.60	0.355
N	0.74	0.80	0.40	0.237

Final couple of steps involves determining the corresponding the consequent mass distribution as shown in following table (yellow marked cells).

Table 7: Determining the consequent part of each rule

ω -->	0.4	0.35	0.25	Then (Scavnge Quality)	
	Air Pressure	Temperature	WMC	Satisfactory	Unsatisfactory
If --->	Low (-ive)	Low (-ive)	Satisfactory (+ive)	0.25	0.75
If --->	Low (-ive)	Low (-ive)	Unsatisfactory (-ive)	0	1
If --->	Low (-ive)	Acceptable (+ive)	Satisfactory (+ive)	0.6	0.4
If --->	Low (-ive)	Acceptable (+ive)	Unsatisfactory (-ive)	0.35	0.65
If --->	Low (-ive)	High (-ive)	Satisfactory (+ive)	0.25	0.75
If --->	Low (-ive)	High (-ive)	Unsatisfactory (-ive)	0	1
If --->	Acceptable (+ive)	Low (-ive)	Satisfactory (+ive)	0.65	0.35
If --->	Acceptable (+ive)	Low (-ive)	Unsatisfactory (-ive)	0.4	0.6
If --->	Acceptable (+ive)	Acceptable (+ive)	Satisfactory (+ive)	1	0
If --->	Acceptable (+ive)	Acceptable (+ive)	Unsatisfactory (-ive)	0.75	0.25
If --->	Acceptable (+ive)	High (-ive)	Satisfactory (+ive)	0.65	0.35
If --->	Acceptable (+ive)	High (-ive)	Unsatisfactory (-ive)	0.4	0.6

Activated rule tag	Corresponding antecedent values			Θ (weight of each rule	Unsatisfactory	Satisfactory
A	0.26	0.20	0.60	0.031	0.023	0.008
B	0.26	0.20	0.40	0.021	0.021	0.000
D	0.26	0.80	0.60	0.125	0.050	0.075
E	0.26	0.80	0.40	0.083	0.054	0.029
J	0.74	0.20	0.60	0.089	0.031	0.058
K	0.74	0.20	0.40	0.059	0.035	0.024
M	0.74	0.80	0.60	0.355	0.000	0.355
N	0.74	0.80	0.40	0.237	0.059	0.177

The last step is aggregating the values from table 7 and getting a final value for the 'scavenge air quality' which is coming out as **Satisfactory** 0.73 and **Unsatisfactory** 0.27.

There is slight difference in the results received from this method compared to fuzzy 'min-max' inference process which were **Satisfactory** 0.70 and **Unsatisfactory** 0.30. Apparently in the given example, there is insignificant difference however ER model has been tested on some of the extreme cases of temperature, pressure and performance and there are indications of striking differences.

Comparative analysis and conclusion

This section will review the level of sensitivity to the changes in the input and how it compares with the conventional 'min-max' approach in terms of real numbers. To perform the analysis, the scenario developed in the above sections are used however only changing the input 'scavenge pressure' in both the models and observing the differences. Following

Pressure (Bars)	1.0	1.1	1.2	1.3	1.4	1.5	1.6	1.7
'Min-Max' inference*	0.60	0.60	0.60	0.62	0.70	0.75	0.75	0.75
ER inference *	0.55	0.59	0.65	0.68	0.73	0.77	0.81	0.88

* Fuzzy output 'Satisfactory Scavenge air quality'

The following graph further demonstrates the difference between the two outputs from different inference processes.

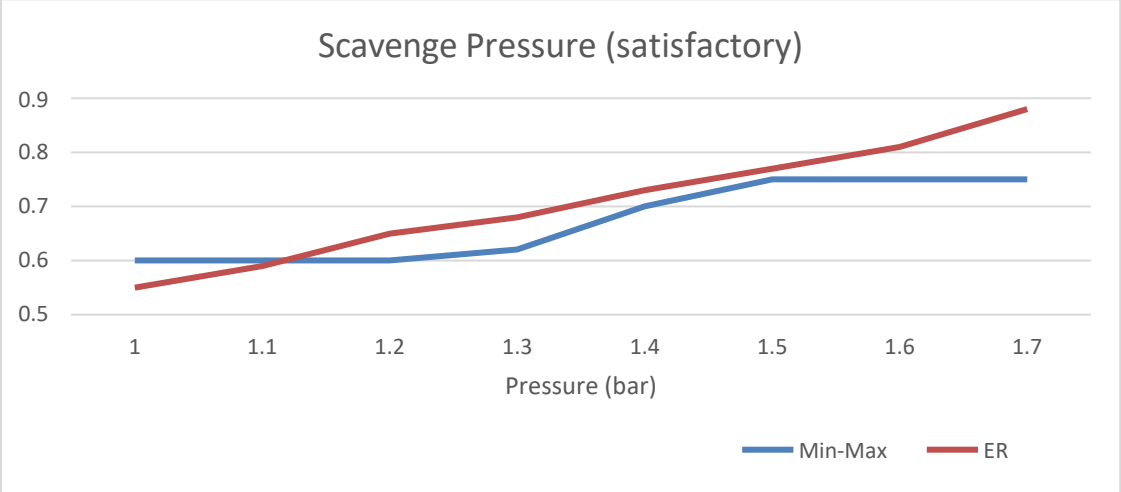

This shows that the ER inference process demonstrated relatively better sensitivity tot the variations in the input whilst 'min-max' curve flattens out at low and high pressures. The model has also been tested by altering other operational inputs and similar results were found.

This paper proposes to integrate ER approach to the fuzzy model used to determine the prior probability for BN model developed for 2-stroke engine health assessment. Further work is needed with the help of IDS software tool and supplementary mapping to cover the remaining 2-stroke engine operational spectrum employed within BN health assessment model.

References

Asuquo, M.P; Wang, J; Phylip-Jones, G; Riahi, R (2019) Condition monitoring of marine and offshore machinery using evidential reasoning techniques. Journal of marine engineering & technology. https://doi.org/10.1080/20464177.2019.1573457

Liu, J; Yang, J.B; Wang, J; Sii, H.S (2003) Review of uncertainty reasoning approaches as guidance for maritime and offshore safety-based assessment.

The Swedish Club (2019) Main Engine Damage [online]. Available at https://www.swedishclub.com/media_upload/files/Loss%20Prevention/Main%20Engine%20Damage%202018/TSC-main-engine-web%202018%20%281%29.pdf. [Accessed: 30th January 2019]

Usman, M; Chang, C,H; Qu, Z; Yang, Z (2018) A fuzzy modelling approach to standardise the prior probabilities for parent nodes of Bayesian Network (BN) model used for two-stroke engine health assessment. Proceedings of the faculty research week, Liverpool John Moores University.

Yang, Z.L; Wang, J; Bonsall, S; Fang, Q.G. (2009) Use of fuzzy evidential reasoning in maritime security assessment. Risk Analysis, Vol. 29 No.1

Zeng, Y; Wang, L; Zheng, J (2006) Aggregative risk assessment model for international technology and project development. Fifth Wuhan international conference on e-business, integration on innovation through measurement and management. 1(3): 1139-1144

Yang, J.B; Xu, DL (2002) On the Evidential Reasoning Algorithm for Multiple Attribute Decision Analysis Under Uncertainty. IEEE TRANSACTIONS ON SYSTEMS, MAN, AND CYBERNETICS—PART A: SYSTEMS AND HUMANS, VOL. 32, NO. 3

ISSN 2398-6611 (Online)

A Virtual Force-based Method for Environment Coverage by Autonomous Mobile Robots

Kang Ji, Qian Zhang, Dingli Yu
Department of Electronics and Electrical, Liverpool John Moores University,
Kji@2017.ljmu.ac.uk, Q.Zhang@ljmu.ac.uk, D.Yu@ljmu.ac.uk

Abstract. In this project, the problem of using a swarm of autonomous mobile robots for environment monitoring is tackled. In the monitoring task, finding robots' final deployment with satisfying coverage performance from the initial distribution is addressed. A new virtual force-based method has been designed for maximizing coverage area. In this method, two kinds of virtual force (the vortex force and the repulsive force) are introduced to be exerted on the agents. Each agent can update its position under the virtual force and final deployment will be achieved after some iteration. In addition, new structure particle swarm optimization is applied for finding the feasible obstacle-free trajectories of each agent when the environment is known. The deployment of agents with desired coverage performance has been demonstrated in the simulation experiments. The main contribution of this paper is introducing the novel vortex force interaction scheme to strengthen the capability of environment exploration and ensure the uniform distribution in the robotics agent deployment for maximizing area coverage.

Keywords. Autonomous system, multi-agent system, virtual force

1. Introduction

There is growing attention in the application and research about the autonomous mobile robot. The multi-robot system is widely applied in environmental monitoring, search and rescue, and battlefield surveillance. Deployment of a swarm of mobile robots with a circular sensing range for coverage the complex environment is addressed in this study. The core objective is to find robots' positions with maximum coverage of the area of interest from their initial positions and a virtual force interaction method (VFIM) is proposed to achieve it. In this method, virtual vortex force and repulsive force are defined for each robot to find the feasible movement and the well-distributed deployment can be achieved after iterations. The novel vortex force can increase the robots' stronger capability of exploring environment compared with other virtual force-based algorithms.

The virtual force algorithm for the deployment of wireless sensor nodes was firstly proposed by Zou et al. [1]. In VFA, the attractive force and repulsive force between nodes are defined for increasing coverage. His method is not suitable for the environment with many obstacles due to only the simple repulsive force from the obstacle is defined and test in the environment with only one obstacles. Research on the improved virtual force-based methods for coverage control contains introducing Delauny triangulation to set the adjacent relationship to increase computation efficiency [2] introducing energy awareness for each agent in the virtual force method to balance their energy consumption [3] and combining the VFA with particle Swarm optimization for global search ability [4]. The above research assumes the obstacle-free environment and the agents were randomly initialized in the environment at the beginning. However, such an assumption may not be available in real-life scenarios.

3. Methodology for the environment coverage problem

3.1. Problem description

In this environment monitoring problem, various size and shapes obstacles are set in the environment and each agent is initialized along with the environment boundary averagely. Each mobile robotic agent is assumed to have homogeneous characteristics including mobility, sensing a circular zone around its location, obtaining its location and exchange the location information in its communication range.

3.2. Virtual force-based method

The process of the proposed virtual force based method contains two core parts in each iteration: calculating virtual force and moving to the new position. For observing the coverage performance change in the whole process, the grid scanning method is utilized [5].

3.2.1. Virtual force definition

For each agent, it is assumed to receive the virtual force from the following source including the nearby agents, obstacles and environment boundary. The virtual force can be identified two types: vortex force for better exploration of the whole environment and repulsive force for local exploitation. The Obstacle and boundary can exert both vortex force and repulsive force upon the nearby agent while the agent can only exert a repulsive force on the nearby agent.

The repulsive force among agents can reduce their coverage overlap when they are close. The repulsive force from agent *i* to agent *j* is inversely proportional to their distance when the distance is less than a distance threshold that is double sensing range. The orientation is the direction of the vector from agent *i* and agent *j*. The repulsive force from the obstacle can decrease the uninterested area coverage when the agent is close to it. The magnitude of the force is propositional to the agent's invisible area caused by the obstacle. The orientation is from the nearest point of observed obstacle boundary to the agent. The repulsive force from the boundary is inversely proportional to the shortest distance between the agent and the environment boundary when the distance is great than a threshold value. The direction of vortex force from the obstacle or the boundary is orthogonal to the direction of the corresponding repulsive force and the magnitude is proportional the magnitude of the corresponding repulsive force with a randomized coefficient in the range of (0.5, 1).

3.2.2. Movement rules

Each agent will update its position consecutively according to the three sources: the combined repulsive force and two kinds of vortex forces. The movement can be calculated as equation (1) and (2).

$$x_{new} = \begin{cases} x_{now}, & if\ \left|\overrightarrow{F_s}\right| = 0 \\ x_{now} + W_s * S_m * sign\left(\overrightarrow{F_{sx}}\right) * \left|\overrightarrow{F_{sx}}/\overrightarrow{F_s}\right| * e^{-\frac{1}{\left|\overrightarrow{F_s}\right|}}, & if\ \left|\overrightarrow{F_s}\right| > 0 \end{cases} \quad (1)$$

$$y_{new} = \begin{cases} y_{now}, & if\ \left|\overrightarrow{F_s}\right| = 0 \\ y_{now} + W_s * S_m * sign\left(\overrightarrow{F_{sy}}\right) * \left|\overrightarrow{F_{sy}}/\overrightarrow{F_s}\right| * e^{-\frac{1}{\left|\overrightarrow{F_s}\right|}}, & if\ \left|\overrightarrow{F_s}\right| > 0 \end{cases} \quad (2)$$

Where (x_{now}, y_{now}) and (x_{new}, y_{new}) is the current position and newly calculated position of the agent; S_m is the maximum of one-step size; W_s is the uniformly distributed random variable in the range of (0.8, 1); $\overrightarrow{F_s}$, $\overrightarrow{F_{sx}}$ and $\overrightarrow{F_{sy}}$ are one type of received virtual force and its component forces along the x-coordinate and y-coordinate respectively.

3.3. Path planning strategy

The proposed VFIS method enables to find the destination with good coverage performance for each agent despite the environment information is known or unknown for agents. If the environment is known, the virtual trajectory of each agent can be generated from VFIS and it can be optimized by a centralized path planning method. In this condition, an improved version of PSO method named nPSO is chosen [6]. When applying nPSO, the prohibited area is set by the inflated obstacle borders. The intermediate points between the start position and destination of each agent are defined as movable millstones whose coordinates are decision variables in nPSO. The fitness function is as equation (14).

$$f = \sum_{i=1}^{N_m+1}(L_i * (1 + 100 * v)) \quad (14)$$

where N_m is the number of moveable milestones; L_i is the length of the line segment between the ith milestone and the $(i+1)$th milestone; v is a discrete variable whose value is 1 or 0, where "1" indicates there are intersections between the line segment and the obstacle's extended borders.

4. Experiments and results

4.1. Expeperiment environment setting

The experiments are conducted through simulation in MATLAB. The environment is expressed a grey square with 100-units side length and the obstacles are expressed by black objects. The sensing range of each agent is set as 10 and the communication range is triple the sensing range. Each agent is set along the environment border averagely at first. Figure 1 presents two environment settings with different numbers of obstacles and two conditions of using a different number of agents.

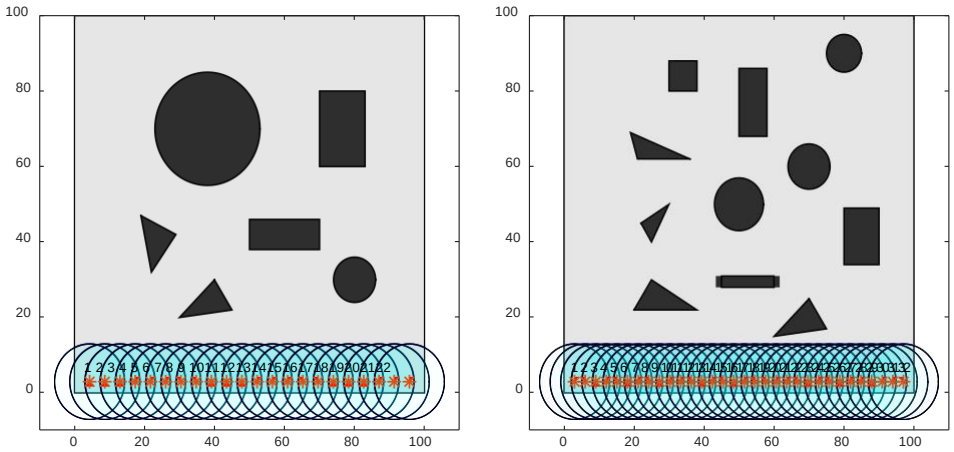

(a) Fewer agents in 6-obstacle environment (b) More agents in the 11-obstacle environment

Figure 1 Settings of environments and agents

4.2. Experimental results

4.2.1. Coverage performance

Considering different conditions of the number of obstacles in the environment and the number of agents, four groups of experiments are designed and conducted. For verifying the reliability of experiment results, each group of experiments is repeated ten times. Coverage rate is defined as the ratio of the covered area to the area of the environment excluding the obstacles.

Figure 2 and table 1 present the appropriated distributions with a high coverage level can be achieved through the proposed method in all 4 situations. In table 1, the average coverage area keeps large and the standard deviation is relatively small in all experiments, which shows the method's effectiveness and reliability. When the number of agents increases in the same environment, there will be better coverage performance. When the number of obstacles increases, the coverage rate remains at a good level but may have a minor decrease.

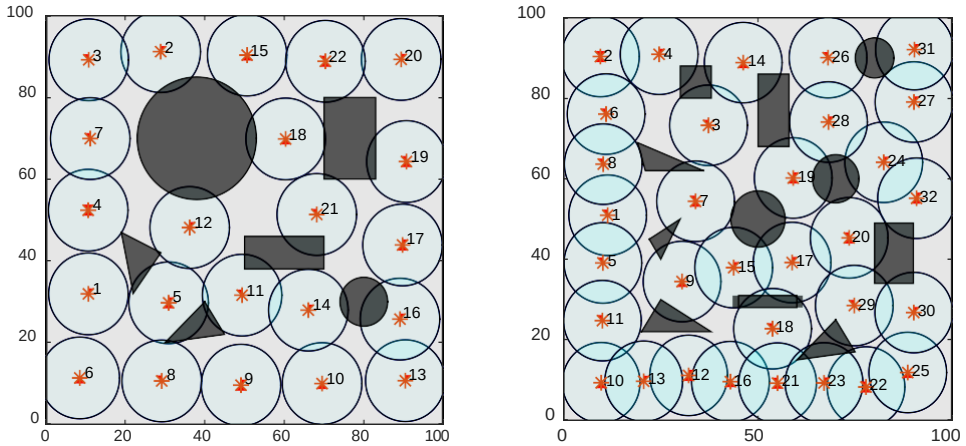

(a) Exp. No.1 (b) Exp. No. 4

Figure 2 Experiments settings

Table 1. Experimental results.

Exp. No.	Number of agents	Number of obstacles	Obstacle area	Average coverage	Standard deviation of Average coverage	Coverage rate (%)
1	22	6	1373	6468	41.4	75.0 ± 0.5
2	32	6	1373	7784	28.1	90.2± 0.3
3	22	11	966	6220	29.4	76.6± 0.3
4	32	11	966	7818	18.0	90.7± 0.2

4.2.2. Results of path planning

Figure 3 presents the raw trajectories and the trajectories after the optimization of the nPSO method. It can found that nPSO method enables to generate the short obstacle-free trajectories.

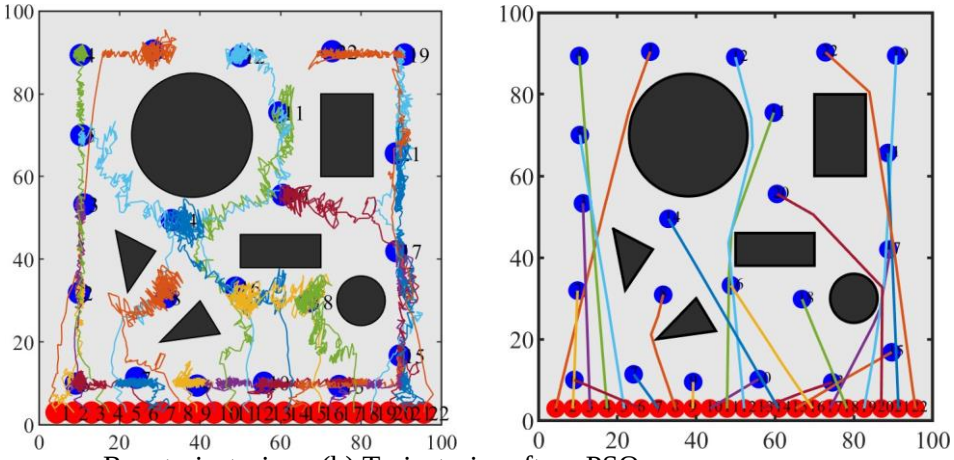

(a) Raw trajectories (b) Trajectories after nPSO

Figure 3 Raw trajectories and path planning result

5. Conclusion

The paper presents the design and implementation of a virtual force-based method for the environment monitoring problem using the multi-robot system. The novel virtual vortex force is designed to cooperate with repulsive forces to achieve a good balance between global exploration and local adaptation and the deployment with good coverage performance and even distribution has been achieved in the simulation experiments.

6. References

[1] Y. Zou and K. Chakrabarty, "Sensor deployment and target localization based on virtual forces," in *INFOCOM 2003. Twenty-Second Annual Joint Conference of the IEEE Computer and Communications. IEEE Societies*, 2003, vol. 2, pp. 1293-1303: IEEE.

[2] X. Yu, W. Huang, J. Lan, and X. Qian, "A novel virtual force approach for node deployment in wireless sensor network," in *Distributed Computing in Sensor Systems (DCOSS), 2012 IEEE 8th International Conference on*, 2012, pp. 359-363: IEEE.

[3] X. Wang, S. Wang, and D. Bi, "Virtual force-directed particle swarm optimization for dynamic deployment in wireless sensor networks," in *International Conference on Intelligent Computing*, 2007, pp. 292-303: Springer.

[4] G. Sallam, U. Baroudi, and M. Al-Shaboti, "Multi-Robot Deployment Using a Virtual Force Approach:Challenges and Guidelines," *Electronics*, vol. 5, no. 3, p. 34, 2016.

[5] X. Shen, J. Chen, and Y. Sun, "Grid scan: A simple and effective approach for coverage issue in wireless sensor networks," in *Communications, 2006. ICC'06. IEEE International Conference on*, 2006, vol. 8, pp. 3480-3484: IEEE.

[6] Q. Zhang and M. Mahfouf, "A new structure for particle swarm optimization (nPSO) applicable to single objective and multiobjective problems," in *Intelligent Systems, 2006 3rd International IEEE Conference on*, 2006, pp. 176-181: IEEE.

ISSN 2398-6611 (Online)

Development of Risk Optimisation Model for Oil and Gas Pipeline Routes

L Kraidi [1, 2], R Shah [1], W Matipa, [1] and F Borthwick [1]
[1]Department of Built Environment, Faculty of Engineering and Technology, Liverpool John Moores University, Byrom Street Campus, Liverpool. L3 3AF
[2]PhD Student, Henry Cotton Building, 15-21 Webster Street, Liverpool, L3 2ET, UK. Email: L.A.Kraidi@2016.ljmu.ac.uk

Abstract. Identifying safe routes for the pipelines that transport Oil and Gas (O&G) products is a challenging topic in the current environment; particularly in the insure countries. Because the relevant data about the probability and severity levels of the Risk Factors (RFs) that affect the safety of these pipelines are rare. Which makes the existing risk assessment tools ineffective to analyse these RFs and identify safe routes for these pipelines. Hence, this paper aims to develop a risk assessment tool that can identify safe routes for the new O&G pipelines in Iraq in a systematic way using the following steps. Firstly, an industry-wide questionnaire survey was conducted to gather the data about the probability and severity levels of the RFs in such projects in Iraq. Secondly, the Fuzzy Inference System (FIS) in MATLAB was used to analyse and rank the RFs. Because the FIS can reduce the uncertainty in risk analysis, which results from the lack of data and the biases of stakeholder's judgments about the RFs. Thirdly, the existing information from the new pipelines projects were analysed to identify the potential RFs in the proposed routes for these projects. As the O&G pipeline network in Iraq is above-the-ground, this paper focused on the RFs that affect this type of pipelines. Fourthly, the safest route for the new pipeline was identified by optimising the risk index value for each route. While the route that has less value of risk index is the safest route. This paper analysed the five routes that were suggested to build a new gas export pipeline in the Waist in Iraq. The pipeline will transport the extracted gas from Badra filed to the shipping points in Iraq. It was found that route number 4 is the safest route for this pipeline.

Keywords. Oil and gas pipelines, risk assessment tool, pipelines' safety, pipelines' routes and computer model.

1. Introduction and research approach

Oil and Gas Pipelines (OGPs) must be planned, designed, installed, operated and maintained regarding the safety requirements to transport the petroleum products safely. However, several Risks Factors (RFs) are threatening the safety of these projects, such as terrorism, sabotage, thefts, corrosion, design and construction defects, natural hazards, operational errors and many more. Meanwhile, the current risk assessment tools are inaccurate to analyse the RFs in OGP projects in the developing countries due to the data scarcity and lack of research about them in these countries. As stated by Kraidi *et al.*, [1], the risk management system in OGP projects in Iraq suffers from the scarcity of data about the probability and severity levels of the RFs in these projects. The alternative way of identifying and analysing the RFs in such a situation is via conducting a literature review about the RFs in OGP projects and collecting the stakeholders' perceptions about them [2]. Nevertheless, analysing the RFs based on the stakeholders'

perceptions results in uncertain results. Because the stakeholders have different perceptions about the probability and severity levels of the RFs [3]. Therefore, the RFs in this paper will be analysed using the Fuzzy Inference System (FIS) in MATLAB. Because the FIS uses linguistics terms (e.g. very low, low, moderate, high and very high) to analyse the RFs, which is useful to calculate the Risk Index (RI) of the factors when there are neither sharp boundaries nor precise values of their probability and severity levels [4].

The purpose of the paper, therefore, is to develop a risk assessment tool that helps in analysing the RFs in the pipelines' projects and choosing safe routes for the new projects in a systematic way. This tool will analyse the OGP projects in two cities south of Iraq, which are Waist (Al Kut) and Basra. Because the current risk management system in these projects is inadequate, which obstructs gas export activities. Figure 1 shows the flowchart of the risk assessment tool.

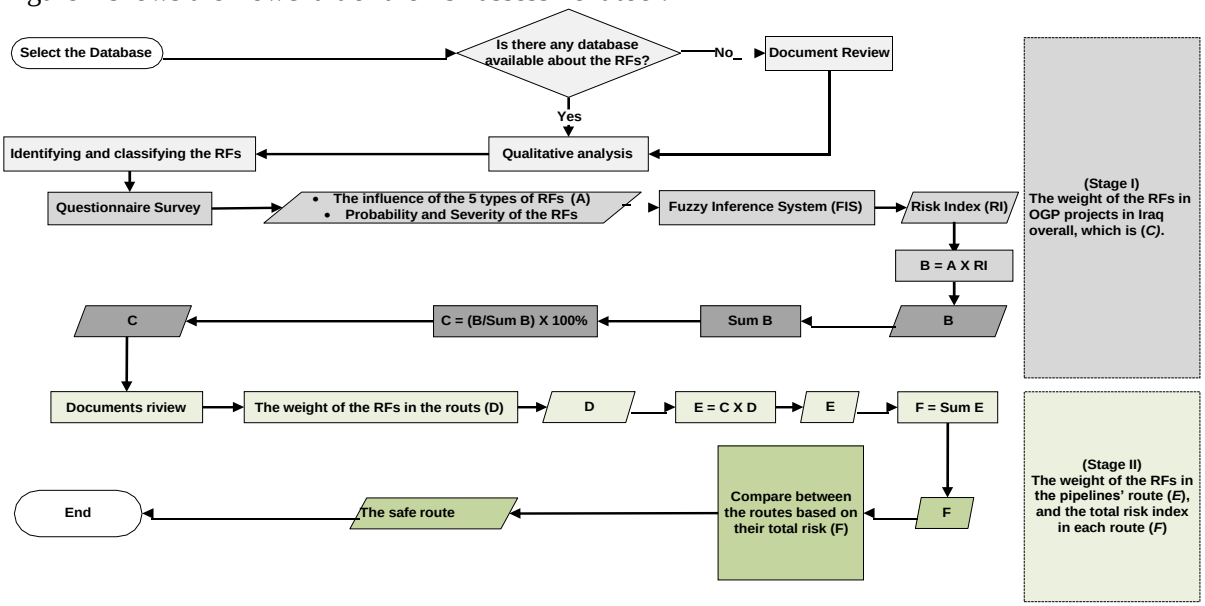

Figure 1: the flowchart of the risk assessment tool.

Following figure 1, the risk assessment tool works in two stages. In stage I, extensive investigations were carried out to identify the RFs in OGP projects in different countries and circumstances to overcome the problem of data scarcity about them in Iraq. The identified RFs were classified into five groups based on their type. Then, the RFs were evaluated via a questionnaire survey that was distributed amongst the stakeholders in OGP projects in Iraq using an online survey tool. The outputs of the survey were the weight of each group of the RFs ($\boldsymbol{A}$). As well as the probability and severity levels of the RFs, which were used as inputs for the FIS in MATLAB to calculate the RI of the RFs, see figure 2. $\boldsymbol{B}$ is the weight of the RF that considers the weight of its groups ($\boldsymbol{A}$) and its value of RI ($\boldsymbol{B = A \times RI}$). $\boldsymbol{C}$ is the weight of the RFs from 100%, where $\boldsymbol{C = (B/Sum\ B) \times 100\%}$.

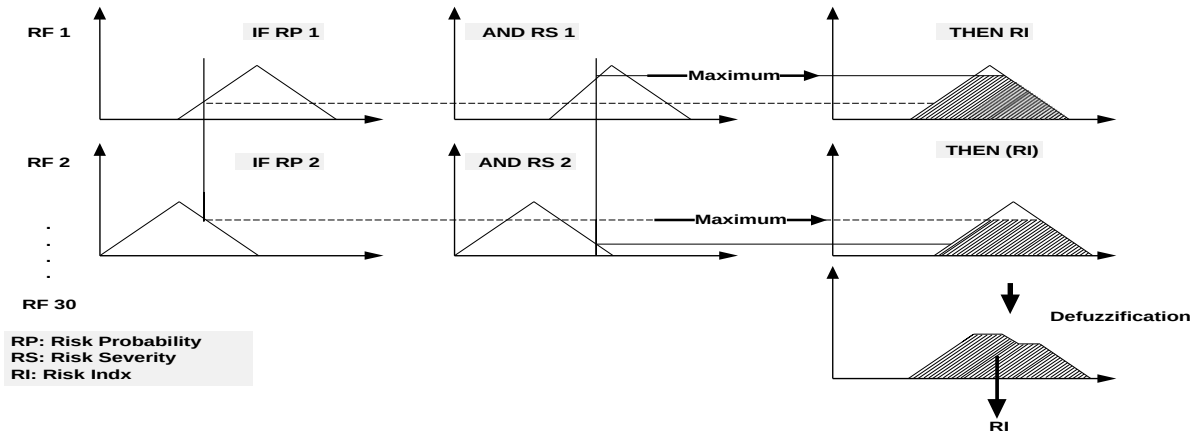

Figure 2: The diagram of the Fuzzy Inference System (FIS)

The results of (Stage I) of risk analysis are shown in table 1.

Table 1: The identified RFs from the literature review and their values of probability, severity and index.

RFs [1-3, 5,6]	Type*	A	Probability	Severity	RI	B	C
Terrorism, sabotage and the security risk	Security and Safety	2.84	3.995	4.490	3.99	11.33	5.43
Stealing the products			3.692	4.081	3.75	10.65	5.10
Public awareness			3.712	4.106	3.80	10.79	5.17
Staff threats			3.323	3.571	3.35	9.51	4.55
Socio-political effects			3.449	3.611	3.49	9.91	4.75
Leakage of sensitive information			2.980	3.399	3.38	9.60	4.60
Corruption	Rules and Regulations	1.45	3.980	4.323	3.87	5.61	2.69
The absence of the law on TPD			3.606	3.682	3.54	5.13	2.46
Lack of risk management practice			3.530	3.652	3.51	5.09	2.44
Lack of proper training			3.646	3.859	3.71	5.38	2.58
Lack of risk registration			3.566	3.662	3.60	5.22	2.50
Little research on this topic			3.621	3.697	3.55	5.15	2.46
The geographical location	Pipeline Location	2.37	3.717	4.192	3.76	8.91	4.27
The pipeline is easy to access			3.631	3.773	3.57	8.46	4.05
Land ownership conflicts			3.495	3.646	3.68	8.72	4.18
Geological risks			2.747	3.182	3.17	7.51	3.60
Vehicles accidents			2.465	2.970	2.80	6.64	3.18
Animals accidents			1.894	2.020	1.95	4.62	2.21
Improper safety regulations	Health, Safety and Environment	1.89	3.687	3.960	3.70	6.99	3.35
Improper inspection and maintenance			3.657	3.899	3.69	6.97	3.34
The risk related to the aboveground pipeline			3.667	3.949	3.70	6.99	3.35
Limited warning signs			3.626	3.732	3.56	6.73	3.22
Inadequate risk management			3.227	3.505	3.48	6.58	3.15
Natural disasters			2.652	3.066	3.10	5.86	2.81
Corrosion	Operations Consent	1.45	3.687	3.990	3.72	5.39	2.58
The weak ability to manage the risk			3.631	3.848	3.67	5.32	2.55
Shortage of modern equipment			3.667	3.924	3.68	5.34	2.55
Design, construction and material defects			3.333	3.611	3.64	5.28	2.53
Operational errors			3.101	3.409	3.30	4.79	2.29
Hacker attacks on the system			3.066	3.066	3.03	4.39	2.10

Stage II of the risk assessment tool is about analysing the RFs in specific routes of OGPs. This paper has analysed the five proposed routes for a new gas pipeline, which will be built from Badra gas field in Waist to Basra in order to export the extracted gas from that field via the sea. The available documents about these five routes were subjectively analysed to identify the RFs that might threaten the pipelines in these routes. $\boldsymbol{D}$ is the weight of the RFs in the route. Based on the document analysis, in the case that the RF is threatening the pipeline, then ($\boldsymbol{D=1}$); otherwise, ($\boldsymbol{D=0}$). Then, ($\boldsymbol{EE = CC \times DD}$), where $\boldsymbol{C}$ is the weight of the RFs in OGP projects in Iraq overall and $\boldsymbol{D}$ is the weight of the RFs within the specific route. Therefore, $\boldsymbol{E}$ is the final weight of the RFs in the route. $\boldsymbol{F}$ is the total risk index in the route, where ($\boldsymbol{FF = SSSSSS\ EE}$). The route that has less value of $\boldsymbol{F}$ is the safest route. Because it has the less total impact of the RFs. The results of analysing the OGPs' routes are shown in table 2.

Table 2: The results of analysing the RFs and testing the pipelines routs.

RFs	C	Route 1		Route 2		Route 3		Route 4		Route 5	
		D1	E1	D2	E2	D3	E3	D4	E4	D5	E5
Terrorism, sabotage and the security risk	5.43	0	0.00	1	5.43	1	5.43	0	0.00	0	0.00
Stealing the products	5.10	1	5.10	1	3.20	1	5.10	0	0.00	0	0.00
Public awareness	5.17	1	5.17	1	3.24	1	5.17	1	5.17	1	5.17
Staff threats	4.55	0	0.00	1	2.86	0	0.00	1	4.55	0	0.00
Socio-political effects	4.75	0	0.00	1	2.98	1	4.75	1	4.75	0	0.00
Leakage of sensitive information	4.60	1	4.60	0	0.00	1	4.60	0	0.00	1	4.60
Corruption	2.69	1	2.69	1	3.30	1	2.69	1	2.69	1	2.69
The absence of the law on TPD	2.46	1	2.46	1	3.02	1	2.46	1	2.46	0	0.00
Lack of risk management practice	2.44	1	2.44	1	2.99	1	2.44	1	2.44	1	2.44
Lack of proper training	2.58	1	2.58	1	3.16	1	2.58	1	2.58	1	2.58
Lack of risk registration	2.50	1	2.50	1	3.07	1	2.50	1	2.50	1	2.50
Little research on this topic	2.46	1	2.46	1	3.03	1	2.46	1	2.46	1	2.46
The geographical location	4.27	0	0.00	1	3.21	1	4.27	0	0.00	0	0.00
The pipeline is easy to access	4.05	1	4.05	1	3.05	1	4.05	0	0.00	1	4.05

Land ownership conflicts	4.18	1	4.18	1	3.14	0	0.00	1	4.18	1	4.18
Geological risks	3.60	0	0.00	1	2.70	1	3.60	0	0.00	1	3.60
Vehicles accidents	3.18	0	0.00	1	2.39	1	3.18	0	0.00	1	3.18
Animals accidents	2.21	0	0.00	0	0.00	0	0.00	0	0.00	0	0.00
Improper safety regulations	3.35	1	3.35	1	3.16	1	3.35	1	3.35	1	3.35
Improper inspection and maintenance	3.34	1	3.34	1	3.15	0	0.00	0	0.00	1	3.34
The risk related to the aboveground pipeline	3.35	1	3.35	1	3.16	0	0.00	1	3.35	1	3.35
Limited warning signs	3.22	0	0.00	1	3.04	1	3.22	0	0.00	1	3.22
Inadequate risk management	3.15	1	3.15	1	2.97	1	3.15	1	3.15	1	3.15
Natural disasters	2.81	1	2.81	0	0.00	1	2.81	0	0.00	1	2.81
Corrosion	2.58	0	0.00	1	3.17	1	2.58	1	2.58	0	0.00
The weak ability to manage the risk	2.55	1	2.55	1	3.13	1	2.55	1	2.55	1	2.55
Shortage of modern equipment	2.55	1	2.55	1	3.14	1	2.55	1	2.55	1	2.55
Design, construction and material defects	2.53	1	2.53	0	0.00	1	2.53	0	0.00	1	2.53
Operational errors	2.29	1	2.29	1	2.81	1	2.29	0	0.00	1	2.29
Hacker attacks on the system	2.10	0	0.00	0	0.00	0	0.00	0	0.00	0	0.00
Sum =	100.00	F1=	64.12	F2=	78.50	**F3=**	**80.27**	F4=	51.29	F4=	66.55

2. Results and Summary

- The developed risk assessment tool in this paper provides a systematic approach of choosing safe routes for OGP projects, specifically for the organisations that just began analysing the RFs in OGPs more effectively, which is the case in OGP projects in Iraq.
- Using the FIS in risk assessment remedies the problems of the traditional approaches to risk analysis and ranking.
- It was found in table 2 that **Route 3** is the riskiest route **(F3 =80)**. Meanwhile, Route 4 is the safest route **(F = 51)**. Therefore, the export gas pipeline should be built on this route**.**
- The future work of this paper is to estimate the consequences of OGPs failures. Moreover, evaluate the cost and time impact of the RFs; as well as, the cost and time impact of the risk mitigation methods that should be applied to mitigate them.

References

1. Kraidi L, Shah R, Matipa W, and Borthwick F. (2019). Analyzing the Critical Risk Factors Associated with Oil and Gas Pipeline Projects in Iraq. International *Journal of Critical Infrastructure Protection*. (**Vol. 24, pp. 17-22**) https://doi.org/10.1016/j.ijcip.2018.10.010
2. Kraidi L, Shah R, Matipa W, and Borthwick F. (2017) Analysing the Critical Risk Factors of Oil and Gas Pipeline Projects in Iraq. In Dubai (Ed.*), The 3rd BUiD Doctoral Research Conference 13th of May 2017. Faculty of Engineering & IT, the British University in Dubai*. (**pp. 133–148**). URL: http://content.buid.ac.ae/bdrc/BDRC2017-Full-Proceedings-Faculty-of-Engineering-and-IT.pdf
3. Lavasani S M, Yang Z, Finlay, J, and Wang, J. (2011). Fuzzy risk assessment of oil and gas offshore wells. *Process Safety and Environmental Protection*. (**Vol. 89(5), pp. 277-294**). https://doi.org/10.1016/j.psep.2011.06.006
4. Biezma, M V, Agudo D, Barron G. (2018). A Fuzzy Logic method: Predicting pipeline external corrosion rate. *International Journal Press of Pressure Vessels and Piping.* (V**ol. 163(June) pp. 55–62**). https://doi.org/10.1016/j.ijpvp.2018.05.001
5. Kraidi L, Shah R, Matipa W, and Borthwick F. (2018). Analyzing the critical risk factors in oil and gas pipelines projects regarding the perceptions of the stakeholders. *In Creative Construction Conference 2018 - Proceedings. Ljubljana, Slovenia, Budapest University of Technology and Economics*. (**pp. 304–311**). https://doi.org/10.3311/CCC2018-041
6. Kraidi L, Shah, R, Matipa, W, & Borthwick F. (2018). An Analysis of the Critical Risk Factors in Oil and Gas Pipeline Projects Using a Comprehensive Risk Management Framework. *This paper was presented as a working paper at the ARCOM 34th Conference, 3-5 September. Belfast, UK, pp 360-368.* URL: http://www.arcom.ac.uk/-docs/archive/2018-Working-Papers.pdf

Acknowledgement The financial support from the Ministry of Higher Education and Scientific Research, Iraq and AL-Muthanna University is highly appreciated.

ISSN 2398-6611 (Online)

Micron diamond processing of advanced ceramics

L Ait Ouarab, X. Chen, T.T. Opoz
General engineering research institute, Liverpool John Moores University,
GERI Building, Byrom Street, Liverpool, L3 3AF
Email: l.aitouarab@2016.ljmu.ac.uk

Abstract: Grinding is one of the most complex manufacturing processes in industry and understanding its physics is difficult due to the stochastic nature of the process. In this work, the influence of the abrasive grit's shape and size on the grinding process is considered. A number of parameters are investigated to set a classification of the abrasives based on particle's shape and size. These parameters are determined according to image analyses of a large number of particles. Based on this method, the shapes of the abrasives grits might be classified into 21 groups. Typical grit shapes will fall into only few categories. Once the abrasives are assessed, a series of multiple grit grinding tests are performed. For this purpose, a scratching tests have been conducted with two different diamond abrasives: MDA M2030 and MDA M3040 with normal size distribution. A sapphire material was used as a workpiece. The machining performances of the abrasive grits are evaluated in consideration of the effect of different grit shapes on grinding process output. The cutting forces and the acoustic emission were used to characterize the grinding mechanism during this experiment. In addition, the scratch marks are characterised by measuring the depth, the width and the length of the marks. This experimental trial provides critical insight of the cutting mechanism and a suitable grit shape is identified for better cutting efficiency**.**

Keywords: Grain shape, size distribution, scratching, diamond abrasives, Acoustic Emission (AE), grinding force

1. Introduction

Abrasive machining process utilises abrasive grits as cutting tool to remove materials from workpiece. Characterisation of the morphology of the grits (shape and size) is of great utility to analyse and improve the grinding performances. In the literature, the main previous researches regarding the grit characterisation consider the shape of the grits to be as a single particular shape: sphere or ellipsoid [1, 2], pyramid with a certain angle or cone shape [3]. Moreover, many abrasive shape models were build based on the aforementioned geometries. While in fact, the grits shapes present a large variety of geometries and are arbitrary distributed over the cutting tool. Hence, a precise shape and size description of the grits at a micron level is required in order to better evaluate its influence on the grinding process. However, publications dealing with abrasive assessment are very few due to the irregularity of the abrasive shapes. This paper aims to develop new test methods for micron diamond processing assessments in considering various application demands and characterising the results on diamond breakdown and performance. In order to find out the influence of the grit size and shape on the grinding process, a particle characterization is carried out by observing the particles under a microscope. In this case, a scanning electron microscope (SEM) is used for the observations.

Two sets of diamond abrasive samples were investigated: (a) MDA M2030 standard size distribution and (b) MDA M3040 normal size distribution. Once these two abrasives are assessed in terms of shape and size, both are used to carry out scratching tests. The grinding efficiency of the cutting process is evaluated in terms of specific energy.

2. Particle characterization and image analysis

2.1. Geometrical grit shape classification:

Based on cutting actions, cutting edges of grits may be classified into 21 groups:
Ball shapes (2): Sphere, Ellipsoid. Cone shape (6): Base sections are round, oval, polygons up to 6 sides. Truncated cone (6): Base sections are round, oval, polygons up to 6 sides. Columns (6): Base sections are round, oval, polygons up to 6 sides. Other shapes are not covered by above types (1).

2.2. Particle's Parameter processing:

The abrasives used in this investigation are bonded on cutting tools and observed under a SEM as it is shown in Figure 1. While there is no limit to the number of particles uploaded, only 100 particle of each abrasive were inspected. Once the images are obtained and based on a subjective visual judgment, each particle is classified into one of the 21 geometrical shapes defined previously. In addition, the particle size (length and width) are measured and then the aspect ratio, defined here as the width divided the length is determined for each particle. A probability density function distribution and shape measurement are conducted. The parameter values for each particle are exported for statistical processing.

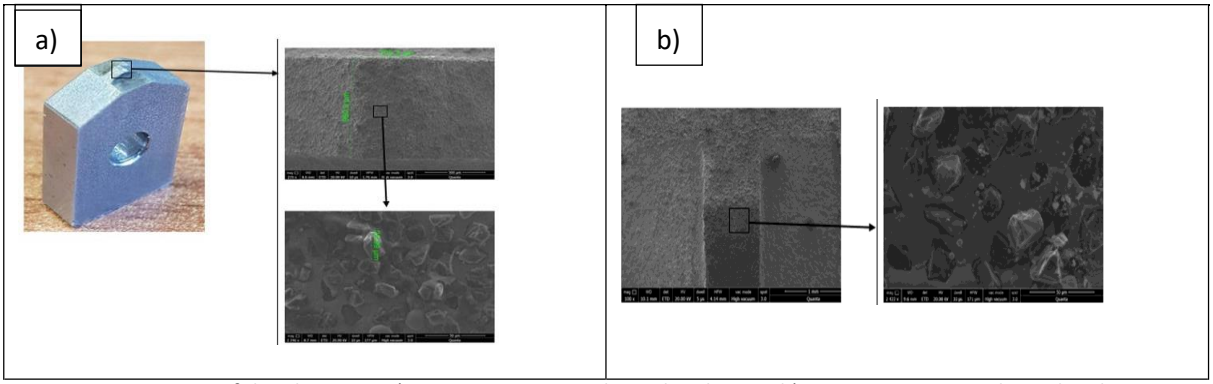

Figure 1: SEM images of the abrasives: a) MDA M2030 normal size distribution, b) MDA M3040 normal size distribution

2.3. Grit shape classification and morphology distribution

Based on the classification methods defined in table previously, the 3D morphological distributions of the two abrasive particles are visually illustrated in Figure 2 with histogram. The geometrical shapes of each sample group are categorised, it can be seen that only a few types of geometrical shapes dominate the population of abrasives grits; ellipsoid, sphere, tetrahedron and quadrilateral shapes are among the most popular one. It appears as well, that the proportion of the ellipsoid shape (34%) is much higher in the case of the MDA M2030 normal size distribution compared to the second abrasive where this proportion is only 20 %.

2.4. Aspect ratio distribution

With a probability density function, the distribution of the AR is presented. On the Figure 3 the distribution of the 2 abrasives samples. As the AR is the ratio of the width over the length, its value is always lower than 1. It is observed that the diamond MDA M2030 normal size distribution present a higher probability density and slightly a higher aspect ratio.

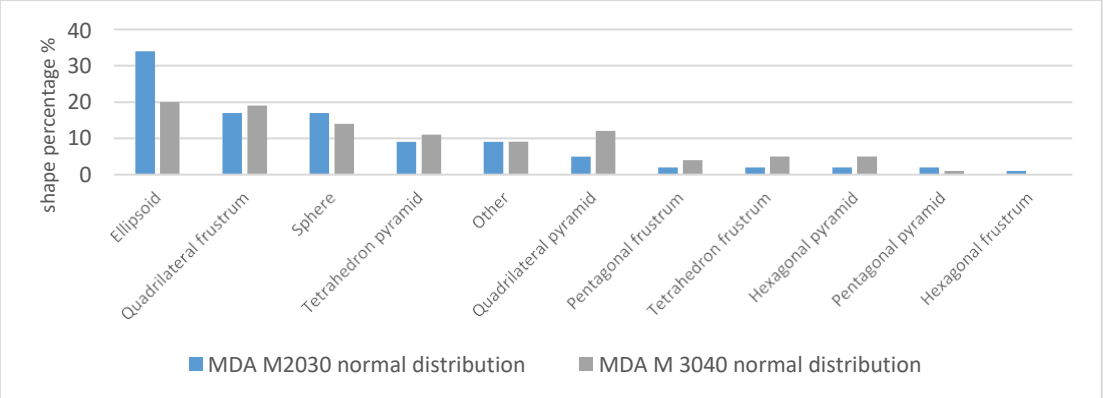

Figure 2: Shape distribution of the two abrasives

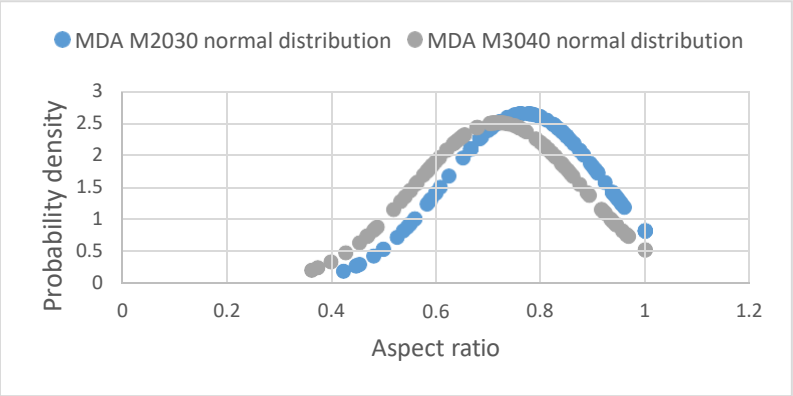

Figure 3: Aspect ratio distribution for the two abrasives

Once the two abrasives were assessed, a scratching tests were carried out in order to find out the cutting performance of each abrasive.

3. Experimental procedure

The set of experimental work was conducted on the XR 610 VMC Hardinge Bridgeport CNC machine in dry condition using a developed rig as shown in figure 4. Table 1 gives the overall parameters for the experiment. The scratching test was performed, where the worktable was moving through the Z-axis towards the steel wheel spindle whilst the steel wheel was rotating. Once the abrasive grits touches the workpiece surface, the AE sensor detects an acoustic emission signal of contact between the abrasives and the workpiece. At this point, the wheel rotation was set to the desired speed before the scratch test commenced. The scratching marks are generated by moving the spindle from the top to the bottom along the X-axis. The process was repeated by shifting the Y-axis position of the worktable to generate new series of scratches. The cutting process was undertaken within two cutting lines where each cutting line is performed with a different type of abrasives. Once the trials were completed, the grinding marks have been inspected and the cutting performance is evaluated in terms of specific energy.

Table 1: Cutting test parameters

Grinding Parameters	**Value**
Wheel diameter	80 mm
Cutting speed V_s	1m/s
Feed rate in Y direction V_w	500mm/m
Cutting depth a_e	1 µm
Spindle speed	238 rpm
Grinding condition	Dry
Workpiece material	Sapphire
Abrasive	• Cutting line 1: MDA M2030 normal size distribution • Cutting line 2: MDA M3040 normal size distribution
Machine tool	XR 610 VMC Hardinge Bridgeport CNC machine

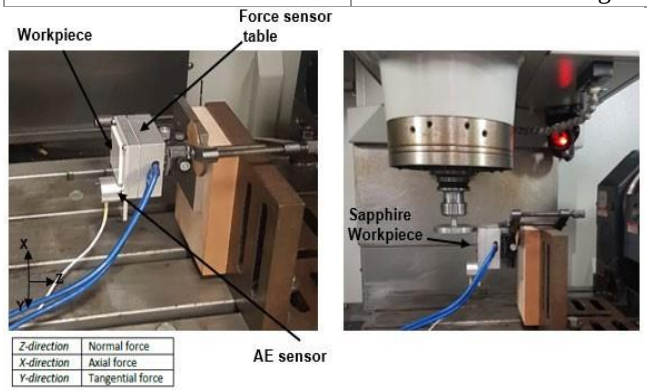

Figure 4: Experimental set up

4. Results and discussion

The cutting performances of the two abrasives (a) MDA M2030 standard size distribution and (b) MDA M3040 normal size distribution is evaluated using the specific energy generated during the cutting process. The specific energy is calculated as the cutting force divided by the cutting area of the scratching marks. The cutting area, the cutting depth and the cutting width are measured using Bruker ContourGT platform (version 64) as it is shown in figure 5.

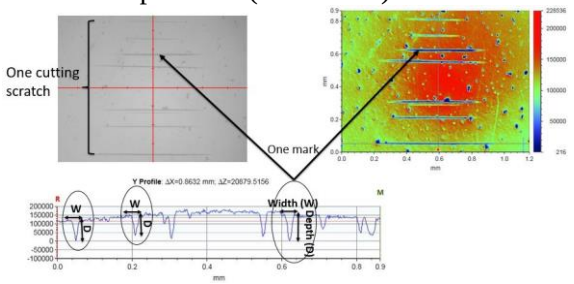

Figure 5: Cutting marks inspection

Figure 6 below, shows that the specific energy decrease when the cutting depth is increasing. This can be explained by the fact that at a high cutting depth, the cutting area is larger and hence imply the diminution of the cutting energy. Furthermore, a higher cutting depth is reached when the abrasive grits involved in the cutting process are more likely to be with sharp shape edges. Moreover, the comparison of the specific energy generated on the two case of cut (cutting with the abrasive (a) and (b) respectively) shows that the specific energy generated while cutting with the abrasive (a) is higher than the specific energy generated while cutting with the abrasive (b). And it was found previously that the abrasive (a) has a higher aspect ratio and present in its shape distribution a higher percentage of ellipsoid shapes. This clearly highlight the influence the abrasive grit shape on the cutting process.

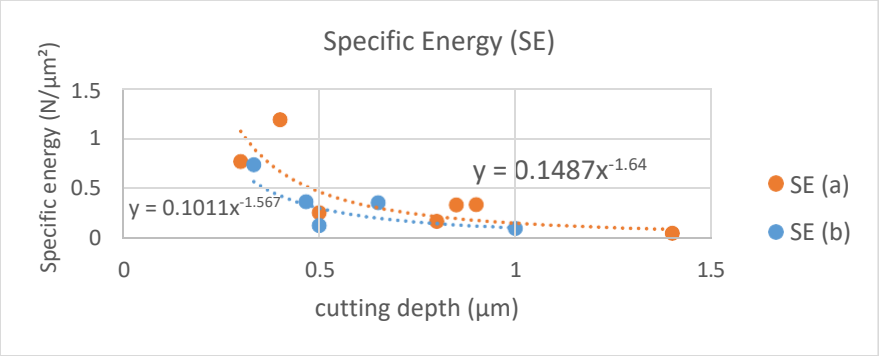

Figure 6: Specific energy generated during the scratching tests

5. Conclusion

A number of parameters have been investigated to measure shape and size of two types of diamond abrasives by means of microscopic measurements and image analysis. The measurements provide details to determine and quantify differences in particle shape and size. The cutting tests curried out emphasis the effect of the grit shape on the cutting process as it was found that the abrasive with lower aspect ratio and with high ellipsoid shape percentage perform a lower specific energy during the cutting process.

References

[1] D. Doman, A. Warkentin and R. Bauer, "A survey of recent grinding wheel topography models," Vols. 343-352, no. 46, 2006.

[2] A. Darafon, A. Warkentin and R. Bauer, "3D metal removal simulation to determine uncut chip thickness, contact length and surface finish in grinding," *Int. J. Adv Manuf Technol,* no. 66, pp. 6-12, 2013.

[3] M. Rasim, P. Mattfeld and F. Klocke, "Analysis of the grain shape influence on the chip formation in grinding," *Journal of Materials Processing Technology,* no. 226, pp. 60-68, 2015.

[4] J. Chen, J. Shen, H. Huang and X. Xu, "Grinding characteristics in high speed grinding of engineering ceramics with brazed diamond wheels," *Journal of Materials Processing Technology,* vol. 210, pp. 899-906, 2010.

ISSN 2398-6611 (Online)

Constraining GRB and SLSN Progenitors using a large, unbiased sample of nearby Core-collapse Supernovae.

Kirsty Taggart
Astrophysics Research
Institute
Liverpool Science Park, IC2
E-mail address: K.L.Taggart@2016.ljmu.ac.uk

In the past 10 years we have come to realise that the range of end-points of massive stars is strikingly diverse. What produces this diversity? It appears that the environment plays a critical role. Both superluminous super- novae (SLSNe) and long duration gamma ray bursts (LGRBs) are found preferentially in faint, low mass galaxies. However we do not know the reason for this. The host galaxy properties of extragalactic transients can be used to study these progenitor populations. However, the high redshift nature of SLSNe and long duration LGRBs makes environmental studies of their galaxies difficult and a comparison sample of core collapse supernova (ccSNe) is lacking. Fortunately, with the advance of wide-field surveys we have increasingly large samples of these transient hosts at low redshift, allowing statistical comparison of the populations.

We have compiled the largest photometric catalogue of nearby SLSN, LGRB and ccSN hosts from a variety of sky surveys. We present this multi-wavelength photometry spanning from UV to near IR in a comprehensive study of the host galaxy populations. We model the observed spectral energy distribution (SED) of these host galaxies with the program Le Phare in order to derive physical properties, such as stellar mass and star formation rate. In this model, we assume the galaxy SED can be approximated by a single-age stellar population. An example of a best-fit SED to one of the CCSNe can be seen in Figure 1 and from this model we derive a stellar mass of 1.3×10^{8} M_0 and a star-formation rate of 0.2 M_0/yr. We compare the stellar mass distributions, luminosity distributions and starburst fractions of transient host populations against each other and to the predicted distribution for the star forming population. This work is a step forward in understanding the progenitor population at low-redshift to aid the characterisation of high-redshift transients and help constrain the connection between ccSNe, SLSNe and LGRBs.

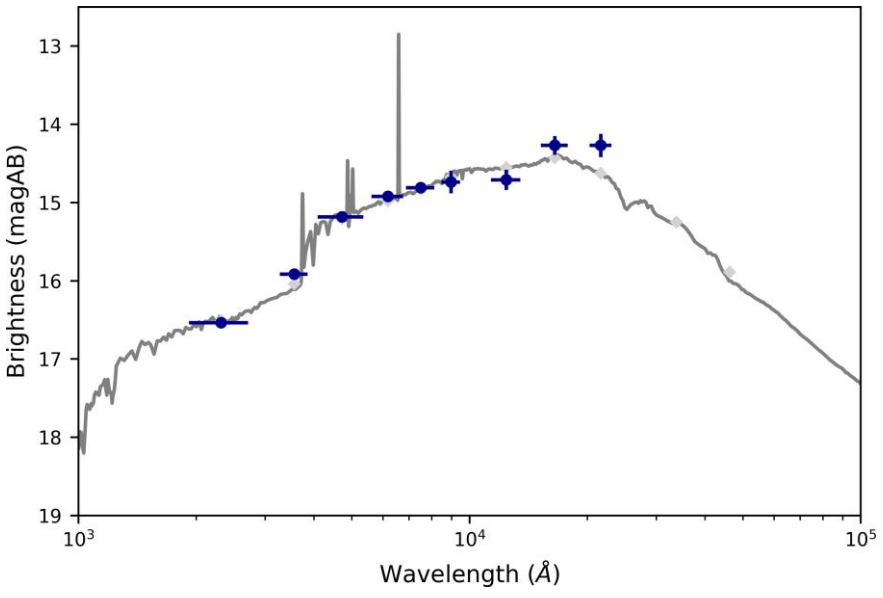

Figure 1. An example of the spectral energy distribution of CGCG012-116, a dwarf galaxy hosting the ccSNe ASASSN-16ab. The black points are the observed magnitudes,The solid grey line displays the best-fit model of the SED. The squares in a lighter shade are the model predicted magnitudes.

ISSN 2398-6611 (Online)

A risk-based approach for implementing functional safety in the UK marine sector

Edward James Shaw
Mechanical and Marine Engineering, Liverpool Offshore and Marine Research Institute, 3 Byrom St, Liverpool L3 3AF.
E-mail address: e.j.shaw@2012.ljmu.ac.uk

Abstract. The UK marine sector has witnessed a rapid increase in sophistication of technology in regards to safety-critical systems whilst neglecting to adopt risk-based legislation regarding the implementation of functional safety. In other engineering sectors that have witnessed similar phenomena, 'good working practice' for the implementation of functional safety comes from using the risk-based approach provided by IEC 61508 Functional Safety of Electrical/Electronic/Programmable Electronic Safety-related Systems (E/E/PE).
This paper introduces IEC 61508, justifies its significance for use in the UK marine sector, and describes a migration strategy proposal for current practice for implementing functional safety in the UK marine sector. IEC 61508 accounts for future development of technology, therefore the migration strategy utilises a balanced scorecard (BSC) for its ability to adapt measures and objectives without straying from its vision. The BSC method balances multiple perspectives to reduce the risk of unsuccessful implementation of its vision.
The objectives of the migration strategy are to use the Delphi method to conduct a questionnaire that gathers a consensus from experts regarding gaps between current practice for implementing functional safety in the UK marine sector, and the guidelines in IEC 61508. Then to rank opinion-based results using the analytical hierarchy process (AHP) to determine the importance or friction currently unimplemented actions for complying with IEC 61508 pose. Then to use the highest ranked methods to produce a BSC that translates opinion-based results into a list of measures and objectives for use in an implementation strategy.

Keywords. IEC 61508, Functional safety, Buncefield, Delphi method, Fuzzy set theory, Analytical hierarchy process, Balanced scorecard.

1. IEC 61508

The 1970s witnessed a culture change towards functional safety of systems that could cause major hazards in the event of a failure. Safety practice used to improve in response to an accident, but the scale of industrial plants began to increase, and use of E/E/PE systems became more common and increasingly complex. As a result, the scale of potential industrial accidents also increased. Engineering sectors realised the importance of identifying potential hazards before they occurred and quantifying the consequences of failure [1]. In 1984, the International Electrotechnical Commission (IEC), commissioned the British Standards Institution (BSI) Technical Committee to assemble a workgroup and produce an international standard for safety-critical software. In 1985, the IEC work group's task expanded to include E/E/PE in the standard, and in 2000, 'IEC 61508 Functional safety of Programmable Electronics Systems' was published [2].

Functional safety engineering involves identifying hazardous failures and then establishing a maximum tolerable frequency target for each mode of failure. Safety-related equipment and safety-critical systems refers to equipment or a system whose failure results in a hazard occurring. A safety function is a function of a piece of equipment that maintains it in a safe state, or brings it to a safe state in the event of a hazard.

The purpose of IEC 61508 is to establish a Safety Integrity target for a safety-critical system, then to provide a strategy for meeting the target by incorporating safety-related equipment into the safety critical systems design [1].

The basic requirements for IEC 61508 are:

- Targeting integrity and assessing random hardware failures: Assessing the rate of random hardware failures, and establishing a Safety Integrity Level (SIL) for mandating the appropriate rigor of life cycle activities.
- ALARP: Establishing whether further safety functions are justified.
- Architecture assessment: An assessment to determine the minimum level of redundancy appropriate for the given fault tolerance.
- Life cycle requirements: Complying with the sub clauses relating to the Overall lifecycle (figure 2).
- Functional Safety Assessment: An assessment to demonstrate compliance with the target SILs.

2. Buncefield

The necessity for implementing IEC 61508 becomes apparent when regarding major accidents that have occurred in recent past. One example is the Buncefield oil depot explosion.

On Sunday 11th December 2005, a fuel tank at the Hertfordshire Oil Storage Terminal overfilled, spilling petrol into the bunding, which resulted in a cloud of petrol vapour engulfing the site [3]. The cloud ignited causing an explosion and fire that spread to 23 other fuel tanks on site and to residential areas within Hemel Hempstead that lasted 5 days.

There were two safety measures to prevent overfilling: a gauge for monitoring the level of the fuel in the tanks and an Independent High Level Switch, neither of which operated correctly the night of the explosion [4]. Staff at Buncefield were aware of the level gauge on tank 912 being unreliable, reporting such the August before. The night of the spill, tank 912 accepted fuel from three pipelines at once, two of which the staff in charge of monitoring the level of the tank could not directly control. The work culture at Buncefield made ‘process operation’ a higher priority than ‘process safety’, this prevented the safety measures getting the attention they required. Many other factors contributed to the overall failure at Buncefield; however, the following conclusions are drawn.

The chances of the accident occurring may have been reduced if the risks were better identified and errors identified in the safety-critical equipment’s operation were dealt with properly. This highlights the importance of sustaining the integrity of safety functions at all stages of a safety-critical systems lifecycle. The Process Oil & Gas, Rail, Defence and Automotive sectors apply IEC 61508, and several other sectors such as the Nuclear and Avionics sectors use the guidelines to supplement their own safety standards to mitigate the chances of major accidents such as the Buncefield explosion from happening again. The UK marine sector is responsible for the operation of many large-scale safety-critical systems and the transportation of large quantities of hazardous material; therefore, it is at risk of a similar major accident until it implements a risk-based approach for implementing functional safety such as IEC 61508.

3. Methodology

Figure 1 is a Project framework model that satisfies the migration strategy objectives and illustrates the three stages of the migration strategy proposal: the process framework, the balanced scorecard framework and the implementation strategy framework. The process framework section includes the initial data gathering methods that are required for producing the BSC. This involves conducting a questionnaire to determine how many methods for complying with IEC 61508 already occur in regards to current functional safety implementation in the UK marine sector, and how much friction complying with others could pose. To validate the results of expert opinion based data, the questionnaire will utilise an iterative Delphi method.

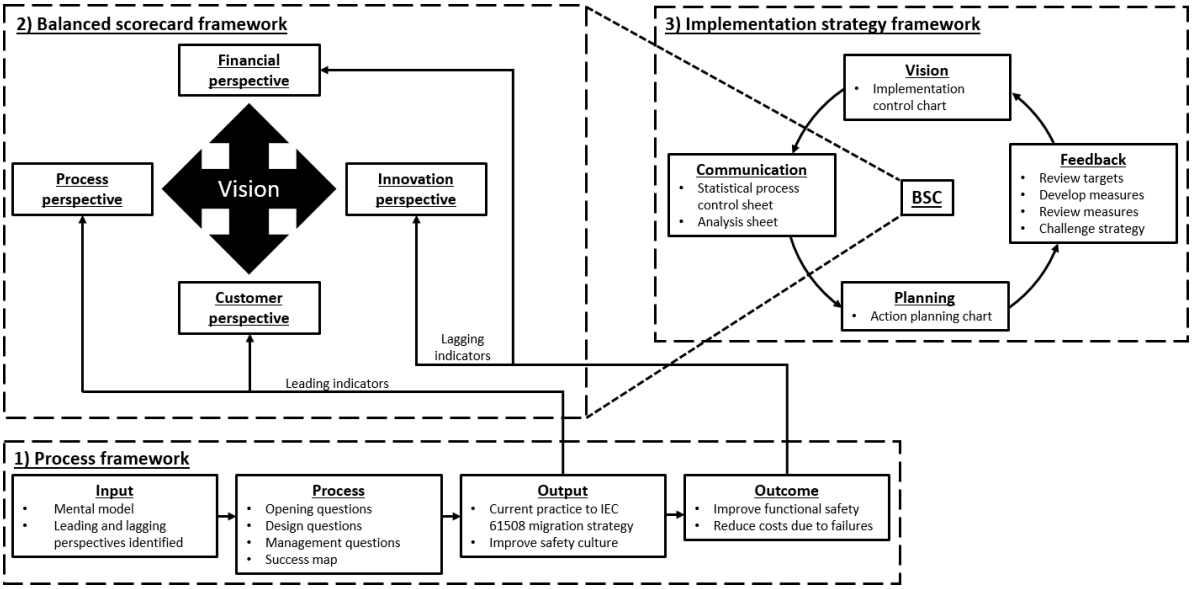

Figure 1 Project Framework.

The purpose of a BSC is to translate a vision an organisation wishes to become a reality into a series of objectives. These objectives must be categorised between different perspectives so that positive changes made to one aspect of the organisation does not inadvertently cause negative changes to another [5]. Typically, the objectives fall into to four perspectives: innovation, process, customer, and financial. The number of objectives used to implement the vision should not exceed 25; however, the number of perspectives, and which aspects of the organisation they represent can vary. Each objective has a system for measuring the success of its implementation, referred to as a measure. Measures are methods for producing quantitative data that represents the progress of its respective objective.

The Balanced scorecard framework processes the gathered data from the questionnaire into objectives and measures for implementing IEC 61508. This involves translating fuzzy qualitative opinion based data from the questionnaire into crisp quantitative data using the triangular defuzzication process. Crisp values that determine the importance of methods required for implementing IEC 61508 will then feature in an AHP to rank them in order. The highest-ranking methods will be categorised between the four perspectives of the BSC and have measures determined.

The Implementation strategy framework involves producing performance measure control sheets (PMCS). The purpose of the PMCS are to ensure the organisation understands the BSC vision, analyse the cause of any change in performance of the organisation, plan the activities required to complete the BSC objectives, ensure these activities are undertaken, and analyse the impact of the activities. The performance-measure control sheets consist of:

- Statistical-process control chart (SPCC)
- Analysis sheet
- Action planning chart (APC)
- Implementation control chart (ICC)

The SPCC provides a mathematical model for each measure. Each model uses a method for tabulating data collected pertaining to its measure, and transferring the data into a graph that illustrates the success of the measures objective over time. The analysis sheet records events that effect the performance of a measure. If an objective relates to improving safety by reducing the risk of a specific system failing, the causes for that system failing are presented in the analysis sheet. Keeping an analysis sheet provides valuable failure data for future use by an organisation in the UK marine sector. An APC provides planning for time and resources for an objective. The dates on the APC should correlate with variance on the SPCC. An ICC displays the steps needed to complete the objective addressed in the previous PMCS's in the form of a Gantt chart. Each BSC objective will require a tailored measure model that will feature in each objectives SPCC.

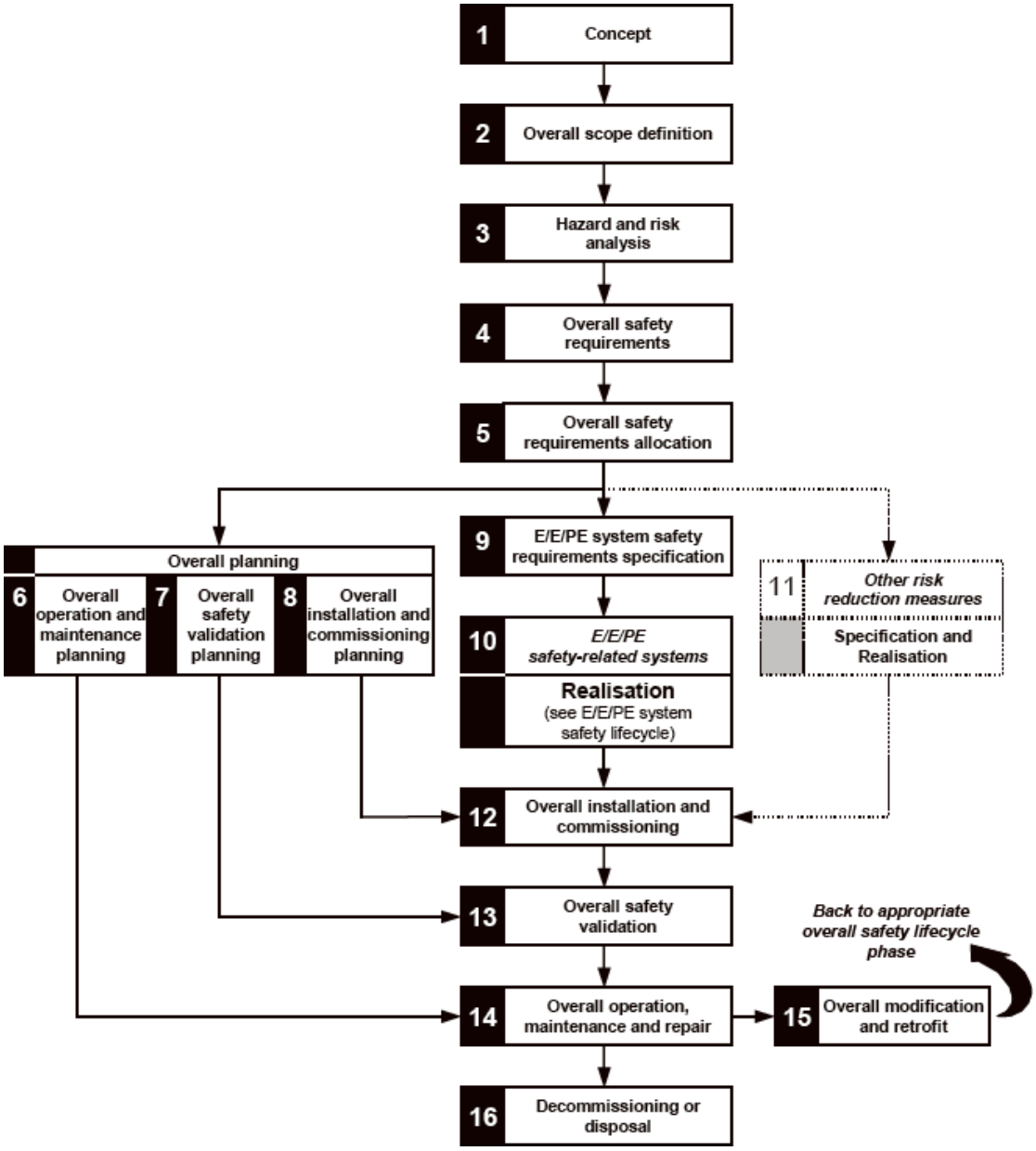

Figure 2 Overall Safety Lifecycle.

The basic requirement of IEC 61508 that requires meeting the life cycle requirements refers to complying with the sub clauses that relate to each key stage of the Overall Safety Lifecycle figure 2. These sub clauses explicitly satisfy the other basic requirements; therefore, the questionnaire translates the sub clauses into objectives for use in a BSC.

4. References

[1] Smith D.J. and Simpson K.G.L. 2016 The Safety Critical Systems Handbook 4th Edition A Straightforward Guide to Functional Safety: IEC 61508 (2010 Edition), IEC 61511 (2015 Edition) and Related Guidance (Elsevier Butterworth-Heinemann)

[2] Bell R 2017 Safety critical systems - A brief history of the development of guidelines and standards (Engineering Safety Consultants (ESC) Ltd)

[3] MIIB 2008 The Buncefield Incident 11 December 2005: The final report of the Major Incident Investigation Board (Volume 1 HSE Books 2008)

[4] HSE 2011 Buncefield: Why did it happen? The underlying causes of the explosion and fire at the Buncefield oil storage depot, Hemel Hempstead, Hertfordshire on 11 December 2005 (Competent Authority for the Control of Major Accident Hazards)

[5] Bourne M and Bourne P 2012 Balanced Scorecard (Chartered management institute, Hodder education)

ISSN 2398-6611 (Online)

Fault detection for wind turbine systems using a neural network estimator.

K Madubuike*, C Mayhew*, Qian Zhang*, B Gomm* and Ding-Li Yu*.
* Control System Research Group, Liverpool John Moores University, Liverpool, UK.

Abstract:
Wind turbine systems have attracted more attention from energy suppliers around the world; this is due to increased government investments and promotion to go green. The importance of power generation from the wind turbine cannot be over emphasized in the electric power industries. However, the failure rate in the wind turbine is increasing because of the remote environment where it is installed. A system failure could be prevented and performance of the system in faulty conditions can be increased by early fault detection and controller reconfiguration. The need for fault detection scheme became very vital for the wind energy industry. This work proposes the use of a neural network (NN) estimator to detect sensor faults in a wind turbine system. The type of NN used is the Radial basis function (RBF) because of its ability to approximate a nonlinear input into a linear output. A benchmark model consisting of a pitch system, a drive train, generator and converter and the state space model is proposed. The benchmark model is characterized by a three-bladed pitch-controlled variable-speed wind turbine with a nominal power of 4.8 MW. The RBF is trained using sample data during a fault free operating condition. The developed method is applied to the benchmark model of the wind turbine system with sensor faults simulated. Simulation results demonstrate that the proposed method is effective with residual signal sensitive to the faults.

Fault Detection, Neural Network and Radial basis function.

I. Introduction

Recently, wind energy has attracted more attention from energy suppliers around the world; this is due to increased government investments and promotion to go green. These have led to the demand for wind energy because it is renewable and eco-friendly [1, 2]. Megawatt-sized wind turbines are expensive; therefore, it is anticipated that their energy production within the short downtimes will be worth the investment [3]. This is hard to achieve without the introduction of fault detection, isolation and accommodation systems into the turbines [3]. Fault detection provides the ability of a system to detect a fault early without human intervention. The effect of fault in a system ranges from total shut down of the system to delay in production until the fault is resolved [3]. Modelling has become the basic tool for analysing dynamic systems including wind turbines. Researchers face challenges related to the availability of data due to competition between wind turbine producers. These challenges led researchers to develop modelling techniques for the wind turbine systems.

From the industrial point of view, different faults can occur in a wind turbine system. Pitch systems could have actuator faults. This actuator fault in the pitch may be caused by air content in the oil or hydraulic pressure drop. This will lead to slow pitch action which makes it impossible for the pitch control to maintain the rated speed in the rotor. The sensor fault can occur by damage of the sensor by maintenance men. This will lead to false measurement of the pitch angle, rotor speed and generator speed. This paper focuses on detecting sensor faults in the pitch angle, rotor speed and generator speed.

In the wind turbine system proposed in this paper, a benchmark model of the wind turbine with physical parameters as used in [3] will be used. A Mat lab and Simulink model will be developed using the benchmark model. Three sensor faults on the pitch angle, rotor speed and generator speed will be simulated on the benchmark model. RBF Neural network will be trained and then later used for fault detection. The rest of the paper is organized as follows: Section II describes the wind turbine benchmark model dynamics. Section III presents the design of the RBF Neural network. Section IV presents the design of RBF Neural network of a wind turbine. Finally, section V presents the conclusion.

II. Wind Turbine Benchmark Model

The wind turbine is designed in a way to conveniently allow electrical energy to be generated from the wind's kinetic energy. The turbine is a variable speed and pitch controlled three-blade horizontal-axis turbine. The following sub-systems make up the wind turbine system; Aerodynamics, Pitch Actuator, Drive-train System, and generator and converters.

A. Aerodynamic model

The drive train is used to transfer aerodynamic torque from the rotor to the generator [3]. The aerodynamic torque is given by (1).

$$\tau_r(t) = \frac{\rho \pi R^3 C_q(\lambda(t),\beta(t)) v_w^2(t)}{2} \quad (1)$$

where $C_q = \frac{C_p}{\lambda}$, ρ is the air density, r is the radius of the blade, C_q is the torque coefficient, β is the pitch angle

and λ is the speed ratio. Power in the wind is given by the rate of change in energy.

$$R_w = \frac{dE}{dt} = \frac{1}{2}\rho A v_w^3 \quad (2)$$

Where $A = \pi R^2$, R is the radius of the blade

According to Betz limit, a wind turbine can extract no more than 59.3% of the energy carried by the wind. The C_p value is unique to each turbine type as no wind turbine can operate at the C_{pmax} value. C_p is dependent on the tip-speed ratio λ and blade pitch angle β. This is expressed in (3). Due to factors like gear box, bearings and generator, only 10-30% of the power of the wind is eventually converted into useable electricity. Hence the available power from the wind is given by (4).

$$\begin{cases} C_p(\lambda,\beta) = 0.22\left(\frac{116}{\lambda_i} - 0.4\beta - 5\right)e^{-12.5/\lambda_i} \\ \frac{1}{\lambda_i} = \frac{1}{\lambda + 0.08\beta} - \frac{0.035}{\beta^3+1} \end{cases} \quad (3)$$

$$\lambda = \frac{w_r R}{v_w}$$

w_r =Mechanical angular velocity in rad/sec. v_w =Wind speed in m/s

$$P_{avail} = \frac{1}{2}\rho A v_w^3 C_p \quad (4)$$

B. Pitch system

The pitch system is a hydraulic system which is modelled as a second order system between the measured pitch angle β and the reference signalβr.

$$\ddot{\beta}(t) = -2\dot{\beta}(t)\zeta\omega_n - \beta(t){\omega_n}^2 + \beta_r(t){\omega_n}^2 \quad (5)$$

Where β_r is the desired pitch angle and β is the actual pitch angle ω_n and ζ are the natural frequency and damping ratio of the pitch actuator respectively.

C. Drive Train

The drive train model is modelled as a rotational 2-mass, 1-spring.1-damper system. The drive train of a wind turbine system consists of a main gear box, low speed shaft (turbine) and a high-speed shaft (generator) whose inertias are denoted as Jr and J_g respectively. Its aim is to transfer torque from the low speed shaft (turbine) to the generator using a gearbox. The drive train model is presented in Figure 1

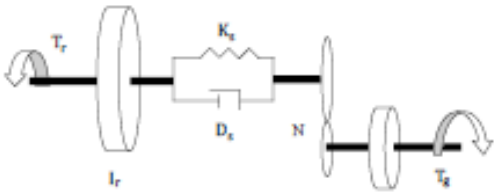

Figure 1: Drive train dynamics [1]

In Figure 1, the shaft on the rotor side is assumed to be flexible and the shaft on the generator side is rigid. The gear unit is assumed to be loss-free. N is the gear ratio between the rotor and the generator. The drive train systems differential equations take the form of (6a) to (6c)

$$\dot{\omega}_r = -\frac{B_{dt}}{j_r}\omega_r + \frac{B_{dt}}{j_r N}\omega_g + \frac{\tau_s}{j_r} + \frac{\tau_r}{j_r} \quad (6a)$$

$$\dot{\omega}_g = -\frac{B_{dt}}{j_g N}\omega_r - \frac{B_{dt}}{j_g N^2}\omega_g - \frac{\tau_s}{j_g N} - \frac{\tau_g}{j_g} \quad (6b)$$

$$\dot{\theta} = \omega_r - \frac{\omega_g}{N} \quad (6c)$$

The system inputs are the rotor torque, pitch angle reference and the generator torque. The outputs of the system are the rotor speed, generator speed and the pitch angle.

III. Radial Basis Function Neural Networks

Rbf network structure

The RBF network is made up of three layers: input layer, hidden layers and output layer where $x = [x_1, x_2, x_3 \ldots . x_m]^T \in R^m$ is the input vector, $h = [h_1, h_2, h_3, \ldots h_q]^T \in R^q$ is the output vector of the hidden layer. $w(k) \epsilon R^{p \times q}$ is the weight of the matrix with entry w_{xy}, which is simply the weight linking the yth node in the hidden layer to the xth node in the output layer and the output vector of the RBF network is represented as $\hat{y} = [\hat{y}_1, \hat{y}_2, \hat{y}_3, \ldots, \hat{y}_q]^T$,

The Rbf is represented in mathematical terms as

$$\hat{y}(k) = w/h(k) \quad (7)$$

$$h(k) = f[z(k)] \quad (8)$$

$$z_i(k) = \sqrt{[x(k) - C_i]^T [x(k) - C_i]} = \|x(k) - C_i\| \quad (9)$$

where $i = 1,2,\cdots q$. $f[\cdot]$ is the nonlinear activation function in the hidden layer. $[\cdot]$ represent the equation for finding the Gaussian basis function.

$$f[z(k), \sigma] = e^{-\left(\frac{z^2(k)}{\sigma^2}\right)} \quad (10)$$

where σ is a positive scalar known as width, which is defined as a distance scaling parameter to determine the distance in the input space over which the unit will have a significant output.

In this paper the Rbf network will be used to predict some unmeasurable variables. The steps is to determine network input according to the dynamics of the system, data collection and scaling, network training and validation. In the training of the network the number q of centers is determined, the appropriate centres C_i and widths $\sigma_i, i = 1,2,3,\dots q$ is found from the training data sets and the weight w is obtained by training data and validating the network in a healthy operating conditions. The training algorithms are explained briefly.

a) K-means algorithm

In this paper the centres of the Rbf network are chosen using the algorithm from a set of training data. The steps are listed below;

- Choose q initial cluster centres $c_1(1), c_2(1), \dots c_q(1)$.
- Distribute the sample {x} into $S_j(t)$ among the q clusters domain at the i^{th} iteration step. The set of samples whose cluster is $C_j(t)$ are denoted as $S_j(t)$.

$$x \epsilon S_j(i) \; if \; \|x(k) - C_i\| < \; \|x(k) - C_i\|$$

Where $j = 1,2,3,\dots q, i = 1,2,3,\dots q$.

- Update the cluster centres

$$c_j(i+1) = \frac{1}{N_j} \sum_j^{N_j} S_j(t)$$

Where N_j is the number of elements in $S_j(t)$

- Repeat step 2 and step 3 until

$$C_j(i+1) = c_j(t)$$

b) p-nearest neigbours method

The Rbf network width σ of each unit is amputed by the p nearest neigbours method. The width is selected so that σ is greater than the distance to the nearest unit centre. This can be calculated using (11).

$$\sigma_i = \left(\frac{1}{p} \sum_{j=1}^{p} \|C_i - C_j\|^2\right)^{\frac{1}{2}} \quad (11)$$

Where $i = 1,2,3, \dots q$ and C_j is the p-nearest neighbour of C_i. For the non linear approximation,p depends on the problem and requires experiments to be made to find it.

c) Recursive least square algorithm

This is a recursive form of the least squares algorithm.it is used here to determine the Rbf network weights W which is summarized in (12)-(15).

$$Y_p(t) = Y_c(t) - W(t-1)h(t) \quad (12)$$

$$g_z(t) = \frac{P_{z(t-1)h(t)}}{\mu + h^T(t) P_z(t-1) h(t)} \quad (13)$$

$$P_z(t) = \mu^{-1}[P_z(t-1) - g_z(t) h^T(t) P_z(t-1)] \quad (14)$$

$$W(t) = W(t-1) + g_z(t) Y_p(t) \quad (15)$$

Where $W(t)$ and h(k) represents the Rbf network weights and activation function outputs respectively at iteration k, $y_c(k)$ is the process output vector, and P_z and g_z are middle terms. μ here is called the forgetting factor ranging from 0 to 1 and is chosen to be 1 for offline training. The parameters $g_z, W \; and \; P_z$ are updated orderly for each sample with change in the activation function output h(k).

d) Design Calculations

The wind turbine parameters used in [1] are stated below. The parameters are substituted into system equations (1, 5, 6a, 6b, 6c). $N = 97, J_r = 5.9154 \times 10^7, J_g = 500, D_g = 6.215 \times 10^6, K_s = 8.6763 \times 10^8, \zeta = 0.9$,$R = 63, \rho = 1.225, \tau = 0.1$ and $\omega_n = 0.88$. The network weights are trained using the RLS algorithm with the following parameters set; μ=0.999 , $w(0) = 1.0 \times 10^{-6} \times U_{n_h \times 3}$, $P(0) = 1.0 \times 10^8 \times I_{n_h}$

IV. RBF MODEL OF A WIND TURBINE SYSTEM

A. Data collection

Here a set of random amplitude signals (RAS) are generated and used as wind turbine system input signals. The ranges of these signals are represented in table 1.This is generated randomly to cover the whole range of frequencies and entire operation space of amplitude in the wind turbine.

Table 1: Wind turbine input signals

RAS	Minimum	Maximum
B_{ref}	10	35
T_{gr}	4068	40680
vw	5	20

The inputs are wind speed, reference blade pitch angle and reference generator torque. All the raw data samples are scaled into the range [0, 1] in order to increase the accuracy of the Rbf and decrease the error.

B. Modelling structure

The input of the RBF model will now be determined. The selection is based on modelling trials where the model structure generates the smallest modelling errors. The selected structure is made up of 18 inputs and 3 outputs. The hidden layer was chosen to be 8. This is chosen buy experiment. The center is calculated using k-means clustering algorithm and the width σ was chosen using the p-nearest neighbors. The simulation was ran for 1000secs with 1000 data samples collected. These data samples were used to train the Rbf NN.

C. Fault detection using Rbf NN

a) No fault condition

An independent NN model is trained with data collected from the wind turbine at healthy conditions. The modelling error between the wind turbine output and the model prediction will be used as the residual signal. Here the residual is just modelling error caused by noise and model-plant mismatch. This is shown in figure 2.

a) At faulty condition

A total of 5000 data sets were used in testing. Three sensor faults are considered here. They are 20 to 50 percent changes on the output of the wind turbine blade angle, rotor speed and generator speed sensors. The faults occurred as can be presented in table 2. The faulty data for the sensors are generated using multiplying factors of 0.5, 1.5,1 respectively. These faults are simulated with the wind turbine model. Fig 3 shows the residual signal of the wind turbine. It can be seen clearly that the three sensor faults could be detected by the designed Rbf Neural network.

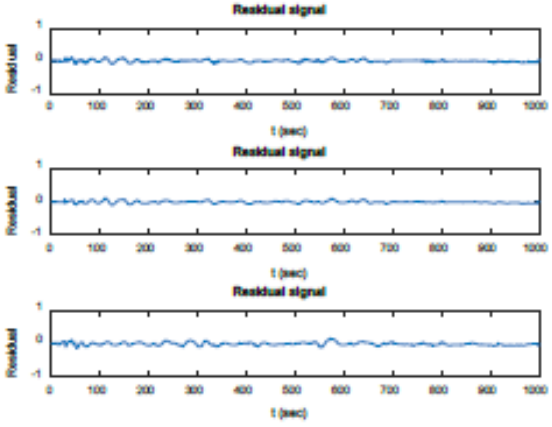

Figure 2: Residual signals of the wind turbine

Table 2: Sensor Output faults time

Outputs	Time of fault
Pitch angle	1000-1500
Rotor speed	4000-4500
Generator speed	2500-3000

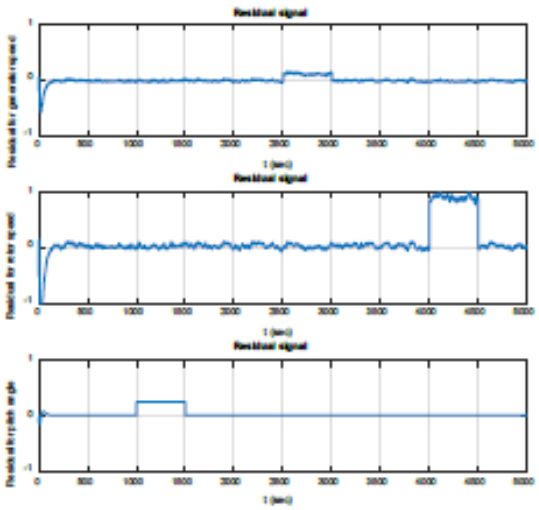

Figure 3: Residual signals of a faulty wind turbine

V. CONCLUSION

In this paper, a robust fault detection approach using radial basis function neural network is proposed. The mathematical model of the wind turbine system is studied. The choice of the Rbf is because of its ability to approximate a nonlinear input into a linear output. The training process is also faster and better. The RBF is trained using sample data during a fault free operating condition. The developed method is applied to the benchmark model of the wind turbine system with sensor faults simulated. Simulation results demonstrate that the proposed method is effective with residual signal sensitive to the sensor faults. Further works will be carried out on how to isolate and tolerate actuator and sensor faults in a wind turbine.

REFERENCES

[1] Liu Yusheng, Yu Ding-Li (2014), "Robust fault detection for wind turbine systems" proceedings of the 20th international conference on Automation and computing, Cranfield university, Bedfordshire, UK. 12-13 September, 2014.

References

[1] Martinez J (2007), “Modelling and control of wind turbines” Department of chemical engineering and chemical technology Imperial college London.

[2] P. Odgaard, J. Stoustrup, M. Kinnaert (2013), “Fault- tolerant control of wind turbines: A benchmark model”, IEEE Transactions on Control Systems Technology Vol 21 (4), 4 July 2013, 1168–1182.

[3] Polycarpou M (2000), “Fault Accommodation of a Class of Multivariable Nonlinear Dynamical Systems Using a Learning Approach” IEEE transactions on automatic control, vol. 46, no. 5, may 2001.R. Nicole, “Title of paper with only first word capitalized,” J. Name Stand. Abbrev., in press.

[4] Van, M., Shuzhi, S., and Hongliang, R. (2017), Robust Fault-Tolerant Control for a Class of Second-Order Nonlinear Systems Using an Adaptive Third-Order Sliding Mode Control, *IEEE trans. on systems, man and cybernetics: systems*, vol. 47, no. 2, February 2017.

[5] Wang, S.H., Davison, E.J. and Dorato, P. (1975), “A parameter insensitive technique for aircraft sensor fault analysis.” journal. of Guidance, Control and Dynamics, Vol.10, pp. 359-367.

[6] ZHAI, Y. & YU, D. (2008) “Radial-basis-function-based feedforward—feedback control for air—fuel ratio of spark ignition engines” Proceedings of the Institution of Mechanical Engineers, Part D: Journal of Automobile Engineering, 222, 415-428

ISSN 2398-6611 (Online)

The rate of reaction for diamine oxidase against two actively metabolised polyamines

M Amin[1], K A. Whitehead[3], L Shalamanova[3], R L. Taylor[3], S Wylie[2] and *B M. Abdullah[1]
[1]Liverpool John Moores University, Department of Engineering and Technology, Built Environment, UK.
[2]Liverpool John Moores University, Department of Engineering and Technology, Civil Engineering, UK.
[3]Manchester Metropolitan University, Microbiology at Interfaces Group, UK.
Email Address: M.Amin@2018.LJMU.ac.uk and *B.M.Abdullah@ljmu.ac.uk

Abstract
Diamine oxidase and its substrates can be measured using a reaction, coupling peroxidase and o-dianisidine dihydrochloride with two biogenic polyamines, cadaverine and putrescine. This method provides a rapid, reliable test for determining the enzymatic activity of diamine oxidase against its respective substrates. Using this method, it was reported that diamine oxidase (0.1 U) and cadaverine (40 μg/mL) required a total time of 150 s for complete uptake of the substrate. Similarly, putrescine (40 μg/mL) demonstrated total catalysis by the 120 s point, thus indicating that, initially enzyme catalysis between diamine oxidase and the polyamines, cadaverine and putrescine occurs and a timescale for complete catalysis was achieved. This work would allow for the detection of polyamines using a diamine oxidase based enzymatic assay within the healthcare and food industries.

Keywords. Diamine Oxidase, Cadaverine, Putrescine, Enzymatic Assay

Introduction
Naturally occurring polyamines putrescine, spermine and spermidine, which are derived from ornithine decarboxylation exist as ubiquitous organic cationic compounds that retain tightly regulated functions through key enzymes during biosynthesis (Moinard et al., 2005). These amines are reported to be essential components for all living cells, due to their requirements in cell growth, proliferation and normal function (Kozová et al., 2009). They aid in the regulatory functions of DNA, RNA and protein synthesis, which coincides with regular eukaryotic cell growth (Venza et al., 2001). Due to their involvement in cell growth, it isn't unconceivable that their involvement in many proliferative physiological processes may be closely related to the concentration and efficacy of polyamines (Handa et al., 2018). Trace levels of polyamines from dietary sources such as agmatine, which is synthesised by plants and many microorganisms, of which include the intestinal micro flora, have been found in human tissue (Handa et al., 2018). The polyamines, cadaverine and putrescine are present in variable amounts of foods (Barrdocz et al., 1993), and through decarboxylation *via* putrefactive bacteria, which explains why higher concentrations of polyamines would be present in fermented foods (Kalač et al., 2002).

Since its discovery, diamine oxidase has been recognised to catalyse the breakdown and consequential oxidation of polyamines into their respective aldehydes (Stoner, 1985). The rate at which this catalysis occurs is measured through a method known as an enzymatic assay. The main factors when considering an enzymatic assay are temperature, pH, ionic strength and concentrations for both enzyme and substrate (Bisswanger, 2014). Due to the complex diversity of enzymes, standardisation of such a procedure is difficult, thus each enzymatic assay is uniquely respective to the target enzyme and/or substrate (Dong et al., 2015). For detailed measurements in to the exact rate of the enzymatic reaction, spectrophotometry is an appropriate method. Spectrophotometry allows for measurements of absorption, thus extending the observation range exponentially (Bisswanger, 2014). Furthermore, due to ease of use, and low susceptibility towards interferences, spectrophotometric assays are ideal in

enzymatic assay measurements. Thus, this work aims to determine the enzymatic activity of diamine oxidase against cadaverine and putrescine using a spectrophotometric, microtiter plate-based method.

Materials and Methods

Solutions of diamine oxidase (Sigma, UK), peroxidase from horseradish (HRP) (Sigma, UK) and o-dianisidine dihdrochloride (Sigma, UK) were prepared in phosphate buffered saline (pH 7.2) (Oxoid, UK). Cadaverine (Sigma, UK) and putrescine (Sigma, UK) solutions were prepared by adding 40 μg/ mL of stock cadaverine/putrescine to 1 mL of sterile distilled water (pH 7.0) and then vortexed for 2 s for even distribution.

To a 96 well plate (Thermo Scientific, UK), 160 μL of phosphate buffered saline (PBS) was added to each well. Ten microliters of diamine oxidase (0.01U) was added to each well following a 1 hr incubation at 37˚C in 5% CO_2. Following the addition of diamine oxidase enzyme, 10 μL of peroxidase from horseradish and o-dianisidine dihydrochloride (Sigma, UK), were added to each well, ensuring this was done in a dark environment as to not degrade the dye. Before addition of polyamine substrate, the plate reader (Thermo Scientific, UK) was calibrated to the following parameters: Incubation temperature set to constant 37°C, Kinetic loop at 10 s intervals, allowing for 480 s of enzyme substrate activity, Photometric, single wavelength set to accurate at 405 nm. The polyamines, cadaverine and putrescine (10 μL) are added to each respective well and gently mixed to disperse evenly in each well. Care was taken not to introduce bubbles as this may interfere with absorbance readings. The plate was then placed in the plate reader for measurements to be taken and recorded.

Results and Discussion

Enzymatic assays involve the rate of a chemical reaction, including all potential factors such as temperature, concentration and pH, which may influence an enzymes rate at which a substrate is catalysed (Robinson, 2015). The results of this study demonstrated that binding between cadaverine (40 μg/ mL) and diamine oxidase (DAO) (0.05 U) was proficient (figure 1), resulting in a substrate-enzyme complex and subsequent release of H_2O_2. A sharp increase in absorbance shortly after a substrate is inoculated with its respective enzyme, followed by a plateau (as demonstrated in figure 1) is indicative of a standard rate of reaction curve (Ishikawa et al., 1993). The increase in absorbance depicts the uptake of substrate *via* the enzyme active site, thus producing H_2O_2 (Pan et al., 2010). The plateau demonstrates the end of the reaction, where all substrate has been catalysed into their respective breakdown products, or there is no longer any active enzyme present for uptake of substrate. In this work, the reaction taking place was evident of enzyme substrate formation, since the reaction would demonstrate no absorbance change without the production of H_2O_2, as the colorimetric dye (o-dianisidine dihydrochloride) would not be oxidised by HRP in the absence of H_2O_2 (Claiborne and Fridovich, 1979). The reaction occurred in accordance to the following equation (1):

(1) Cadaverine + H_2O + O_2 $\xrightarrow{\text{Diamine Oxidase}}$ 5 - Aminobutanaldehyde + NH_3 + H_2O_2

The reaction used HPR with o-dianisidine dihydrochloride in the presence of H_2O_2 (2) (the substrate in this reaction was introduced at the last step, to maximise the orange oxidised end-product formation). This was measured spectrophotometrically at 405 nm.

(2) H_2O_2 + o-dianisidine dihydrochloride(reduced) $\xrightarrow{\text{Peroxidase}}$ $2H_2O$ + o-dianisidine dihydrochloride(oxidized)

The rate of reaction was determined to evaluate the time required for all the substrate (cadaverine) to be catalysed by the diamine oxidase enzyme and converted to its appropriate by-products. The time required, using the 2.5 U peroxidase was 120 s. This time was similar to that of the 25 U HRP however; the reaction was initiated at a much greater absorbance of 0.8162 nm, whilst showing a smaller absorbance increase over the course of the reaction. This suggested that increasing the concentrations of HRP in the reaction did not affect the rate at which the reaction occurred however, the absorbance intensity increased. The enzymatic assay allowed for determination of the timeframe

needed for diamine oxidase to completely catalyse the conversion of cadaverine into 5-aminobutanaldehyde, NH_3 and H_2O_2.

The enzymatic reaction was then carried out against putrescine, using the same method to determine the efficacy of putrescine towards diamine oxidase and determine its rate of catalysis (figure 2). Similarly to cadaverine, putrescine showed in increase in absorbance over a timeframe of 150 s however, the absorbance readings were at a much lower maximum reading (0.44 1nm at 2.5 U HRP and 0.738 nm at 25 U HRP). This was potentially due to the fact that diamine oxidase, whilst being a diamine molecule catalyst, demonstrates a much stronger binding affinity towards cadaverine (almost 1.5x higher affinity), whilst demonstrating a less specific response, albeit still selective, towards putrescine (Elmore et al., 2002).

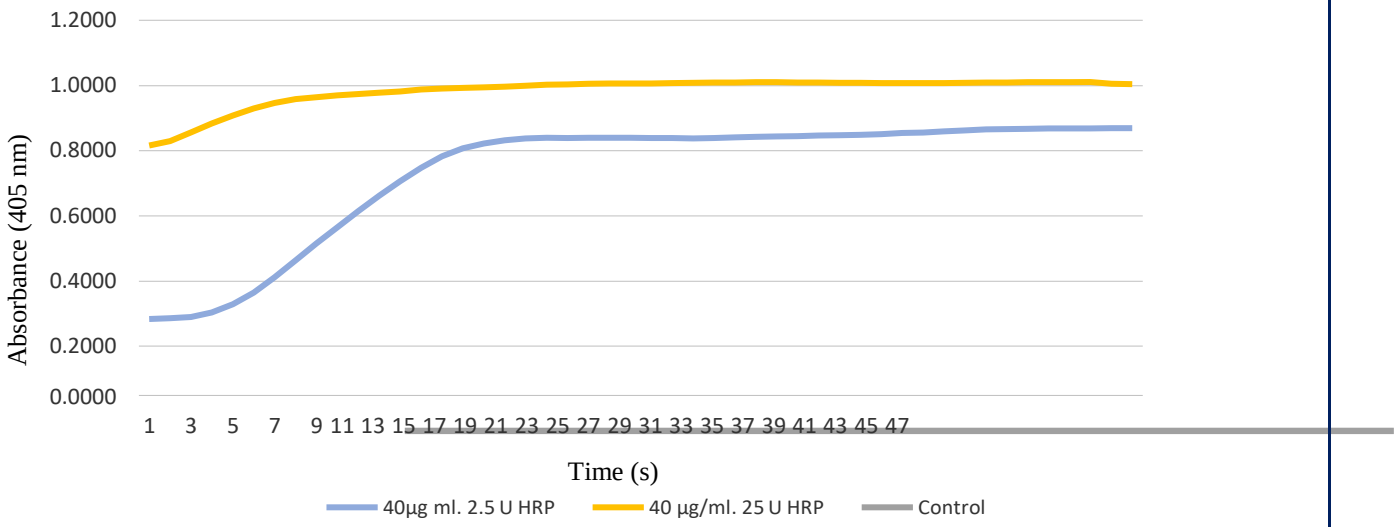

Figure 1. Diamine oxidase activity was measured as a function of time. Absorbance of physiological concentrations of cadaverine measured using a rate of reaction assay. Diamine oxidase with peroxidase (two concentrations of 2.5 and 25 units (U) respectively) and o-dianisidine dihydrochloride were used for determination of cadaverine substrate binding at an absorbance of 405 nm (n=2).

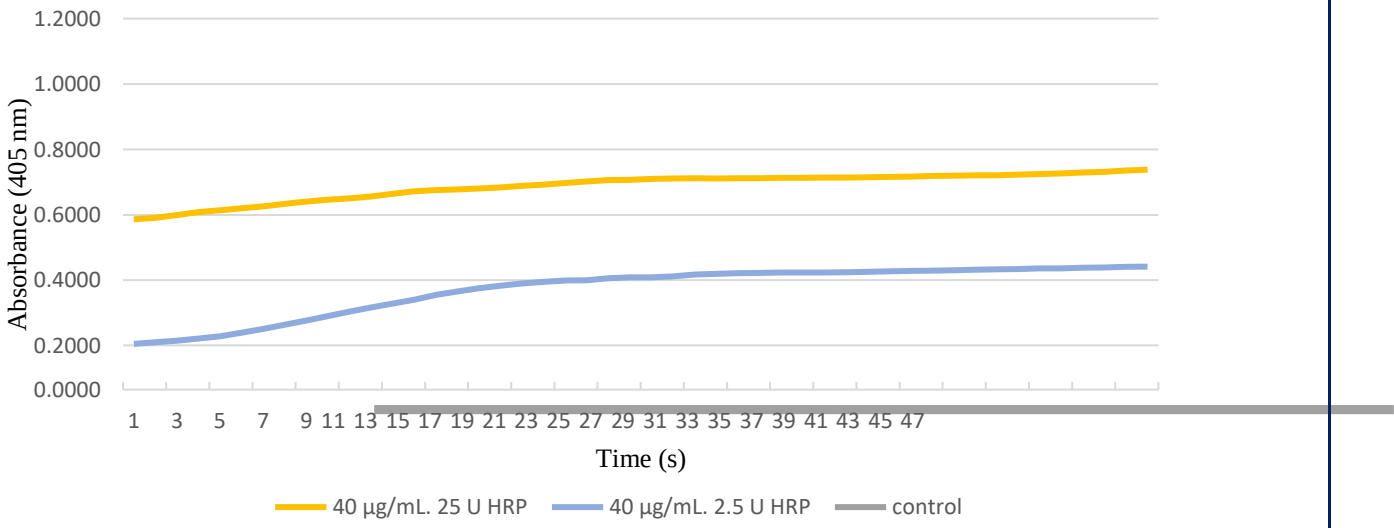

Figure 2. Diamine oxidase activity was measured as a function of time**.** Absorbance of physiological concentrations of putrescine measured using a rate of reaction assay. Diamine oxidase with peroxidase (two concentrations of 2.5 and 25 units (U) respectively) and o-dianisidine dihydrochloride were used for determination of putrescine substrate binding at an absorbance of 405 nm (n=2)

Conclusion

A rapid and simple test for determining the enzymatic catalysis rate of two polyamines, cadaverine and putrescine, using diamine oxidase was done. This method employed the used of hydrogen peroxide production coupled with o-dianisidine dihydrochloride to produce a colorimetric reaction, measured at 405 nm using a spectrophotometric plater reader. It was determined that cadaverine and putrescine require 120 s and 150 s, respectively from their initial introduction into the enzyme mixture to achieve complete catalysis and stop further H_2O_2 production. This work can be used in several healthcare or food industrial applications for detection the presence of polyamines in biological samples as indicators of disease, or for determining food freshness such as fish and meat *via* presence and concentrations of polyamines.

References

Bardocz,S., Grant, G., Brown, D., Ralph, A. and Puszati, A. (1993) Polyamines in food—implications for growth and health☆. *The Journal of Nutritional Biochemistry*, 4 (2), pp.66-71.

Bisswanger, H. (2014) Enzyme assays. *Perspectives in Science*, 1 (1-6), pp.41-55.

Claiborne, A. and Fridovich, I. (1979) Chemical and enzymic intermediates in the peroxidation of o-dianisidine by horseradish peroxidase. 1. Spectral properties of the products of dianisidine oxidation. *Biochemistry*, 18 (11), pp.2324-2329.

Dong, H., Liu, Y., Zu, X., Li, N., Li, F. and Zhang, D. (2015). An Enzymatic Assay for High-Throughput Screening of Cytidine-Producing Microbial Strains. *PLOS ONE*, 10(3), pp.121.

Elmore, B., Bollinger, J. and Dooley, D. (2002). Human kidney diamine oxidase: heterologous expression, purification, and characterization. *JBIC Journal of Biological Inorganic Chemistry*, 7(6), pp.565-579.

Handa, A., Fatima, T. and Mattoo, A. (2018) Polyamines: Bio-Molecules with Diverse Functions in Plant and Human Health and Disease. *Frontiers in Chemistry*, 6. pp.1-12.

Ishikawa, H., Ogino, H. and Oshida, H. (1991). Rates of reactions catalysed by a dimeric enzyme. Effects of the reaction scheme and the kinetic parameters on co-operativity. *Biochemical Journal*, 280(1), pp.131-137.

Kalač, P., Švecová, S. and Pelikánová, T. (2002) Levels of biogenic amines in typical vegetable products. *Food Chemistry*, 77 (3), pp.349-351.

Kozová, M., Kalač, P. and Pelikánová, T. (2009) Contents of biologically active polyamines in chicken meat, liver, heart and skin after slaughter and their changes during meat storage and cooking. *Food Chemistry*, 116 (2), pp.419-425.

Moinard, C., Cynober, L. and Debandtm J. (2005) Polyamines: metabolism and implications in human diseases. *Clinical Nutrition*, 24 (2), pp.184-197.

Pan, R., Zhang, X., Zhang, Z., Zhou, Y., Tian, W. and He, R. (2010). Substrate-induced Changes in Protease Active Site Conformation Impact on Subsequent Reactions with Substrates. *Journal of Biological Chemistry*, 285(30), pp.22950-22956.

Robinson, P. (2015) Enzymes: principles and biotechnological applications. *Essays In Biochemistry*, 59 (0), pp.1-41.

Stoner, P. (1985) An improved spectrophotometric assay for histamine and diamine oxidase (DAO) activity. *Agents and Actions*, 17 (1), pp.5-9.

Venza, M., Visalli, M., Cicciu', D. and Teti, D. (2001) Determination of polyamines in human saliva by high-performance liquid chromatography with fluorescence detection. *Journal of Chromatography B: Biomedical Sciences and Applications*, 757 (1), pp.111-117.

ISSN 2398-6611 (Online)

Analysis of maritime accidents using Bayesian Networks

Shiqi Fan
Liverpool Logistic Offshore & Marine Research Institute, Liverpool John Moores University, Liverpool L3 3AF, UK
E-mail address: s.fan@2017.ljmu.ac.uk

Abstract. In the past decades, safety assessment in maritime transportation has raised industry and public's concerns, given complex risks existing in maritime accidents. In the meantime, various causal factors analyses have been developed to identify the inherent relations to maritime accidents. A risk analysis approach is proposed in this article based on Bayesian Networks (BN), to enable analysis of risk factors influencing different types of accident in waterborne transportation, and further to predict the probability of accidents. First, the data is derived from the maritime accident reports from 2012 to 2017 in MAIB and TSB databases to extract the relevant risk factors. New primary data is analysed directly from maritime accident records. Then, the network structure is constructed via the NBN (Naïve Bayesian Network) and validated by sensitivity analysis subsequently. The results reveal that the key risk factors influencing maritime accident types include Ship operation, Voyage segment, Ship type, Gross tonnage, Hull type, and Information. The findings provide transport authorities with useful insights for maritime accident prevention.

Keywords. Maritime transport, Risk analysis, Maritime safety, Bayesian networks

1. Introduction

Waterborne transportation accounts for approximately 90% of the world trades, representing one of the essential concerns among the society. From the 'Safety and Shipping' Annual Report of 2017 [1], published by Allianz Global Corporate & Specialty, there is more than a quarter of ship losses occurred in the South China, Indochina, Indonesia and Philippines regions. Although the number of maritime casualties has declined over the years, there is increasing complexity of maritime risk existing in the shipping industry. Analysis of maritime accident reports is one of the most effective ways to investigate the causal chains and the correlations among causation factors in risk assessment. Studies rely on the discretional context and experts' comments to extract the causal relations among the process of accidents, as well as data-driven methodologies. Specifically, casual relations are connected to one type of accidents through accident analysis method [2-4]. However, in face with several casual factors affecting maritime accidents, few studies explore the relationship between risk factors and the accident types considering human errors. That is to say, the key factors contributing to collision accidents are probably different from those resulting in grounding accidents.

This study aims at analysing risk attributes in waterborne transportation based on Bayesian network (BN) modelling, and identifying the contributing factors that have impact on different types of maritime accidents. The historical data sources from the maritime accidents occurred in the last 6 years from 2012 to 2017 is utilised to identify the risk. Then, a data-driven BN-based approach is proposed to analyse the accident type in maritime transportation. The results would enhance the understanding of the relationship between risk attributes and the accident type.

2. Methodology

2.1. Model

BN model is a probabilistic directed acyclic graphical (DAG) model introduced by Pearl [5]. It is composed of nodes with the links between them, representing variables and influences of one node on the other(s), respectively. This study developed the NBN(naive Bayesian Network) modelling to decrease the complexity level of the structure. It has an independent node as the target node directly connected to all the other nodes, and no other links between child nodes are allowed in the structure. The NBN is a very commonly used model aiming at classification [6].

Let 'accident type' be the target node, also the class variable (S) with 9 states, $RR =$ $\{RR_{SSSS}, RR_{HHSS}, RR_{SSSS}, RR_{LL}, RR_{GGSS}, RR_{SSSS}, RR_{VVSS}, RR_{WWWW}, RR_{SSW}, RR_{SSTT}, RR_{FFSS}, RR_{SSSS}, RR_{WW}, RR_{EE}, RR_{EETT}, RR_{II}\}$ is the set of risk variables (RR_{kk}) (e.g., ship type, hull type, ship age, length, gross tonnage, ship operation, voyage segment, weather condition, sea condition, time of day, fairway traffic, ship speed, vessel condition, equipment, ergonomic design, information), where each variable represents a category that is obtained and selected from the reports. To obtain the structure of the relationship between S and RR_{kk}, the NBN assumes the pairwise independence of the variables.

2.2. Sensitivity analysis

In the probability theory, the mutual information is a measure of the mutual dependence between two variables. Since the objective of this study is to identify the relationship between RIFs and 'accident type', 'accident type' is determined as the fixed variable in mutual information. The larger the value of mutual information is, the stronger relationship between the factor and 'accident type'. In this way, calculating the mutual information is able to filter out the attributes that are relatively less relevant in the model. Then the remaining attributes are selected as significant variables.

To determine the effects of different variables, a method proposed by Alyami, Yang [7] is applied. This method increases the probability of the state within the highest influencing on the collision to 100% to obtain the High Risk Inference (HRI) of collision. Then it increases the probability of the state generating the lowest influence on the collision to 100% to obtain the Low Risk Inference (LRI) [8] of collision. In this way, calculating the average value of HRI and LRI concludes the True Risk Influence (TRI) of each variable in the case of collision accident type. To obtain the variable influence on 'accident type', the same analysis procedure is applied to other accident types, 'grounding', 'flooding', etc. Therefore, the sensitivity analysis results illustrate the ranking of variables' influences on accident types. In addition, the average TRI value ranks the variables' effects on the 'accident type'.

3. Results and discussion

3.1. Data and variables

In online searching and selecting accident reports database, the MAIB and TSB with a time span of search from Jan. 2012 to Dec. 2017 were reviewed for the maritime accident reports. The search was conducted in Jan. 2018 and the general statistics are presented.

A maritime accident can be classified according to the original accident reports written by MAIB and TSB organisations, i.e. collision, grounding, flooding fire/explosion, capsize, contact/crush, sinking, overboard, and others. Further, the accident-related categories or attributes are retrieved in table 1.

Table 1. The accident-related categories.

Notation	Descriptions	Values
R_{ST}	Passenger vessel, tug, barge, fishing vessel, container ship, bulk carrier, RORO, tanker or chemical ship, cargo ship, others.	1, 2, 3, 4, 5, 6, 7, 8, 9, 10
R_{HT}	Steel, wood, aluminium, others	1, 2, 4, 5
R_{SA}	(0 5], [6 10], [11 15], [16 20], >20, NA	1, 2, 3, 4, 5, 6
R_{L}	≤100, >100, NA	1, 2, 3
R_{GT}	≤300, 300 to 10000, >10000, NA	1, 2, 3, 4
R_{SO}	Towing, Loading/unloading, Pilotage, Manoeuvring, Fishing, At anchor, On passage, others	1, 2, 3, 4, 5, 6, 7, 8
R_{VS}	In port, Departure, Arrival, Mid-water, Transit, others	1, 2, 3, 4, 5, 6
R_{WC}	Good or poor considering rain, wind, fog, visibility	1, 2
R_{SC}	Good or poor considering falling/rising tide, current, waves	1, 2

R_{TD}	07:00 to 19:00, other	1, 2
R_{FT}	Good or poor considering complex geographic environment, dense traffic, or receptive nature of the route contributing to ignorance)	1, 2
R_{SS}	Normal, fast	1, 2
R_{vc}	Good condition of vessels; Poor condition of vessels, increasing complexity, modification made to vessels and size contributes to the accidents	1, 2
R_E	Devices and equipment on board operate correctly; Devices and equipment not fully utilised or operated correctly (e.g., BNWAS switched off, alarm system not noticed)	1, 2
R_{ED}	Ergonomic friendly; ergonomic impact of design (e.g., visual blind sector ahead, motion illusion)	1, 2
R_I	effective and updated information provided; insufficient or lack of information (e.g., poor quality of data, relies on a single piece of navigational equipment, without indicators for observing)	1, 2

3.2. NBN modelling

Assuming that all the variables, i.e. the child nodes, are independent with each other, the NBN is constructed. Based on the NBN model, the posterior probabilities of each variable are calculated. The statistical analysis of the probability of variables reveals some initial findings.

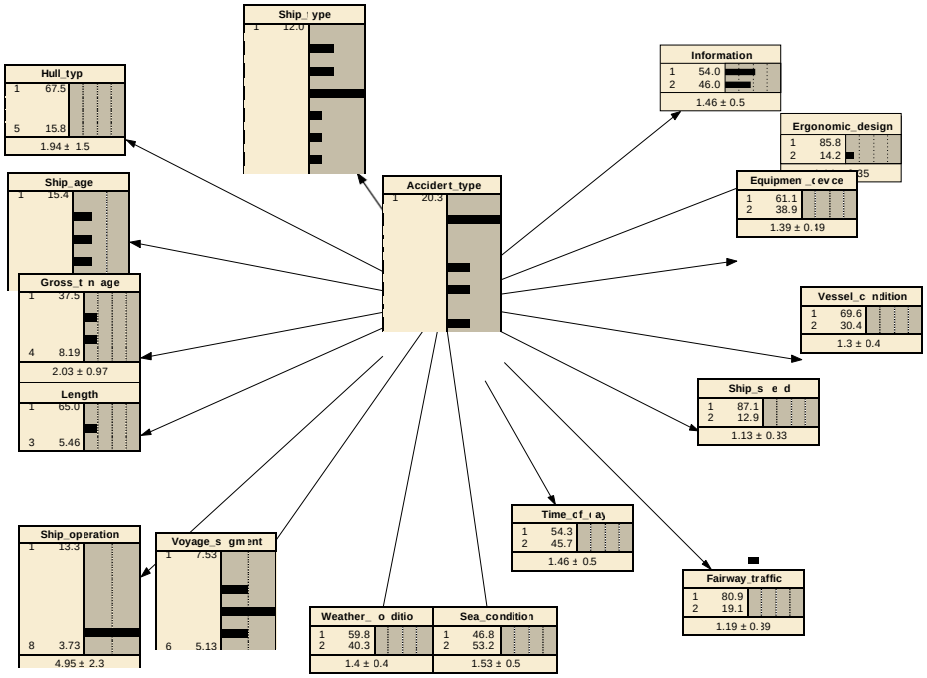

Figure 1. Naïve Bayes network

Figure. 1 presents the initial posterior probability distributions of the factors involved. In the shipping accidents recorded in the maritime accident reports, grounding and collision were two types of accident with the highest probability: 20.3% and 21.2% respectively. 40% of vessels involved in the accidents are in passage rather than other ship operation, and 41.3% of vessels in the accidents are involved in the mid-water of the voyage segment, followed by the arrival segment. 46% of the vessels conveyed insufficient information, 14.2% of the vessels had ergonomic design problems in the face of accidents, 38.9% of them had invalid equipment or devices onboard, and the modification and increasing size of the vessels contributing to human errors is 30.4%.

3.3. Sensitivity analysis

Given that "accident type" is the target node, the "ship operation" has the strongest effect on the accident type: the corresponding amount of mutual information is 0.28294. Based on the mutual information value, we set the threshold to select important variables for further analysis. The variables yield values more than 0.09 and had essential impacts on "accident type", i.e. "ship operation", "voyage segment", "ship type", "gross tonnage", "hull type", and "information". Table 2 shows the TRI values of nodes under different scenarios.

Table 2. TRI of risk variables for all accident type

Node	**TRI**									
	S1	**S2**	**S3**	**S4**	**S5**	**S6**	**S7**	**S8**	**S9**	**Average**
Ship_operation	36.81	40.66	4.74	8.41	20.14	12.48	7.11	25.88	38.72	21.66
Voyage_segment	32.87	29.88	3.91	4.12	18.14	26.75	4.05	18.12	29.63	18.61
Ship_type	23.4	23.64	6.17	6.7	17.43	19.25	8.87	17.22	16.45	15.46
Gross_tonnage	10.7	23.8	3.39	2.38	15.18	12.02	7.15	7.78	8.2	10.07
Hull_type	14	14.6	7.82	16.46	9.34	6.93	8.04	18.81	17.01	12.56
Information	8.5	18.8	3.06	3.4	6.21	12.39	1.01	6.48	8.5	7.59

Specifically, the first row of each variable denotes the base-case scenario, and the following rows respectively represent the different scenarios with each state of the variable reaches 100% occurrence probability. Also, the comparison and ranking between TRI of different variables represent the result of the sensitivity analysis, i.e. the impact level of different variables under the circumstance.

Generally, the most important variables lists for 'accident type' are as follows:

Ship operation > Voyage segment > Ship type > Hull type > Gross tonnage > Information

4. Conclusions

Previous studies mostly focused on the causal factors related to the severity and probability of maritime accidents. In this study, the NBN approach is applied to analyse the RIFs and accident types. To identify significant RIFs, maritime accident reports from MAIB and TSB within 5 years are extracted and reviewed given human errors. The risk-based NBN model is constructed to analyse the causal factors in waterborne accidents. And sensitivity analysis is implemented to validate the model.

Based on the mutual information calculation, the risk variables are ranked and extracted according to the degree of sharing information with the node of accident type. The results reveal that the order of the critical attributes for the maritime accident type is: Ship operation, Voyage segment, Ship type, Gross tonnage, Hull type, Information.

In general, the results from the NBN present the influence of RIFs in the objective description on the accident type. More subjective data for human factors in view of communication, situation awareness, fatigue, etc., is being processed to conduct further research to illustrate the influence of human error attribute on maritime accidents.

References

[1] Specialty A G C, 2018, *Safety and Shipping Review 2017.*

[2] Hanninen M and Kujala P, 2012, *Influences of variables on ship collision probability in a Bayesian belief network model.* Reliability Engineering & System Safety. **102**. 27-40.

[3] Macrae C, 2009, *Human factors at sea: common patterns of error in groundings and collisions.* Maritime Policy & Management. **36**(1). 21-38.

[4] Uğurlu Ö, Köse E, Yıldırım U, and Yüksekyıldız E, 2015, *Marine accident analysis for collision and grounding in oil tanker using FTA method.* Maritime Policy & Management. **42**(2). 163-85.

[5] Pearl J, 1988, *Probabilistic Reasoning in Intelligent Systems. 1988.* San Mateo, CA: Kaufmann. **23**. 33-34.

[6] Friedman N, Geiger D, and Goldszmidt M, 1997, *Bayesian network classifiers.* Machine learning. **29**(2-3). 131-63.

[7] Alyami H, Yang Z, Riahi R, Bonsall S, and Wang J, 2019, *Advanced uncertainty modelling for container port risk analysis.* Accident Analysis & Prevention. **123**. 411-21.

[8] Yang Z, Yang Z, Yin J, and Qu Z, 2018, *A risk-based game model for rational inspections in port state control.* Transportation Research Part E: Logistics and Transportation Review. **118**. 477-95.